Winter 3-2021

# Halloysite Modified 3D Printer Filament for Medical and Industrial Uses

Antwine William McFarland Jr.

# HALLOYSITE MODIFIED 3D PRINTER FILAMENT FOR MEDICAL AND INDUSTRIAL USES

by

Antwine William McFarland Jr., M.S., B.S., B.S.

A Dissertation Presented in Partial Fulfillment

of the Requirements of the Degree

Doctor of Philosophy

COLLEGE OF ENGINEERING AND SCIENCE
LOUISIANA TECH UNIVERSITY

February 2021

LOUISIANA TECH UNIVERSITY

**GRADUATE SCHOOL**

**December 18, 2020**
Date of dissertation defense

We hereby recommend that the dissertation prepared by

**Antwine William McFarland Jr., M.S., B.S., B.S.**

entitled **Halloysite Modified 3D Printer Filament for Medical and Industrial Uses**

be accepted in partial fulfillment of the requirements for the degree of

**Doctor of Philosophy in Molecular Sciences and Nanotechnology**

David K Mills

David K. Mills
Supervisor of Dissertation Research

GNest

Gergana G. Nestorova
Head of Molecular Sciences and Nanotechnology

**Doctoral Committee Members:**
David Mills
Sven Eklund
Teresa Murray
Phillip McMullan
Rebecca Giorno

**Approved:**

Hisham Hegab
Dean of Engineering & Science

**Approved:**

Ramu Ramachandran
Dean of the Graduate School

GS Form 13a
(01/20)

# ABSTRACT

Thermoplastics can be used as a replacement or alternative for a variety of medical and commercial products. The addition of halloysite nanotubes further enhance the strength and functionality of the composite. The aim of this project was to evaluate the capability polylactic acid (PLA) to be enhance with halloysite nanotubes and other additives. We created a nanocomposite that offered similar stabilization to titanium surgical plates but with the added benefit of bone generation through recruitment and differentiation of mesenchymal stem cells. Varying amounts of PLA and polycaprolactone were combined with growth factor doped halloysite nanotubes or silicon nitrate then extruded into 3D printer filament. Once 3D printed from the custom filament, the nanocomposite was subjected to mechanical and cell culture testing. Human mesenchymal stem cells were exposed to the 3D printed nanocomposites and monitored for osteogenic differentiation.

Additionally, metalized halloysite nanotubes (mHNTs) were added to PLA to make an antibacterial 3D printer filament. Testing of both gentamicin loaded and unloaded mHNTs embedded PLA nanocomposites was conducted on *E. coli* and *S. aureus*. The PLA-mHNT filament was used to make a 3D printed antibacterial mask. Blow-spun fibers made of PLA and mHNTs were used as the filter component, which was added to the antibacterial mask to make an antibacterial respirator.

## APPROVAL FOR SCHOLARLY DISSEMINATION

The author grants to the Prescott Memorial Library of Louisiana Tech University the right to reproduce, by appropriate methods, upon request, any or all portions of this Dissertation. It is understood that "proper request" consists of the agreement, on the part of the requesting party, that said reproduction is for his personal use and that subsequent reproduction will not occur without written approval of the author of this Dissertation. Further, any portions of the Dissertation used in books, papers, and other works must be appropriately referenced to this Dissertation.

Finally, the author of this Dissertation reserves the right to publish freely, in the literature, at any time, any or all portions of this Dissertation.

Author _____

Date _____

# DEDICATION

This dissertation is dedicated to my family and friends. You all motivated me to strive to be the best. Thank you for all the support over the years.

# TABLE OF CONTENTS

# LIST OF FIGURES

# LIST OF TABLES

# ACKNOWLEDGMENTS

These projects were possible because of the mentorship, dedication and encouragement of my advisor and mentor Dr. David K. Mills. I further acknowledge the work put forth by my lab mates to help me succeed in graduate school. I hope I have helped you, as you have me.

# CHAPTER 1

# INTRODUCTION AND BACKGROUND

## 1.1 Industry Standard

With the gaining popularity of using biologically safe polymers in the medical industry, we aim to develop an alternative option to titanium to fixate and stabilize fractured bone. A polymer blend with an enhanced capability to aid in bone regeneration could be the alternative that patients choose over titanium. Surgical implants to preserve fractures have come a long way in a relatively short period. Alloys of vitallium and stainless steel were used for several years but had drawbacks. Stainless steel was the leading manufacturing material. However, testing showed that in many cases, it was inferior to titanium [1]. Stainless steel screws tended to loosen or even breaking before the fracture had been stabilized completely [2]. It was believed that infection played a role in the failure of the stainless-steel implants, but these complications could occur even without disease affecting the screws or surrounding bone [2]. Regardless of that fact, the infection was not typically observed when titanium was used instead of stainless steel.

Additionally, titanium is about 40 percent lighter than stainless steel, making it less taxing on the implant recipient [2]. The utilization of titanium made stainless steel obsolete. The industry standard for reattaching tendons and ligaments has been relatively the same for the past five decades. Titanium is a robust metal that is the leading implant material when a high strength to weight ratio is needed to stabilize or fixate tissues or

other objects in the body. Titanium surgical screws have been used to attach tissues to the bone to closely mimic previous attachment's structure, strength, and functionality of the. These suture anchors are used to attach ligaments or tendons to the bone by drilling holes directly into the existing bone. While titanium has been at the forefront of medical device manufacturing, improvements can be made in designing medical devices.

### 1.2 Drawbacks to Titanium

Complications of titanium, when used *in vivo*, can range from but are not limited to, chondrolysis, synovitis, osteolysis, or even device failure [3]. Chondrolysis and osteolysis typically did not occur due to nanoparticles leaching over time or general wear and tear of the titanium device. Instead, micro-shavings from the insertion of the titanium screws enter adjacent cells and cause lysis. Once the structural integrity is restored following the titanium implant fixation, implant removal becomes an option [4]. Ten percent of titanium implant recipients have concerns about infection and thermal sensitivity in European countries, while United States patients are wary about eventual pain, soreness, tenderness, and disease [4]. In both cases, the 10 percent elect to have their titanium implants removed [4]. Unfortunately, the removal of titanium implants is not a simple task. Osseointegration, a condition in which bone grows over or onto the implant, may occur, leading to the need to remove healthy bone to remove screws or plates [4].

An additional complication could arise if implant breakage happens [5]. Frisken et al. had data to support that implant failure may result in considerably more titanium migrating to proximal lymph nodes. In the study, a 17 percent failure rate was observed and attributed to increased torque and lack of screw taps or antibiotics [5]. Special care

needs to be taken when using titanium braces in elderly patients due to an increased possibility of the patient having higher levels of demineralized bone matrix [6]. Biofilms can form on the titanium implants surface if their surface is not pristine and exhibits any surface roughness [7]. Infections can arise from surface biofilms or compromised immune capabilities due to a surface protein layer that is formed, which makes for a suitable adhesion point for bacterial growth. Biofilms can be formed as soon as 30 minutes after implantation and an increase in thickness and colonies over time [8]. Growth of the bacterial biofilm can not only lead to infection but device weakening and device failure as well.

### 1.3 Current Alternatives to Metal Implants

Advancements in medical technology have made the use of new materials for the manufacturing of structural screws, stabilization plates, and wound sutures. Polymers provide an alternative to the traditional metal in which these products were developed. Careful considerations were taken into the selection process that determines which polymers are used for *in vivo* applications. Special care and testing, in conjunction with the Food and Drug Administration (FDA), ensure that the polymeric compounds that comprise future implants are non-cytotoxic and biocompatible.

The ability to have a 3D printable substance that acts as a scaffold and is later absorbed is the main focus of bioresorbable materials. The scaffold should have specific properties such as controllable porosity, resorbability, and non-toxicity in an *in vivo* environment.[9] Recently, research has been done on many different uses for bioresorbable materials with the properties listed above. One area is in the world of arterial disease repair. Cardiac stents are 3D printed out of bioresorbable materials to

outperform the current metallic stents that are currently being utilized [10]. The new technology is essential because, with the current stents, there are some adverse biological side effects an device reliability issues that include but are not limited to in-stent restenosis and late stent thrombosis [11].

Continuing with research to replace metallic structures with ones made of polymers, Gaball et al. found a bioabsorbable bone plate that exhibited the same strength yet more flexibility of similar bone plates made of titanium [12]. The research showed that the polymers poly(L-lactide-co-D) and poly(L-lactide), when combined at a specific ratio, could be used as a viable replacement option for stabilization of non-weight bearing bones and joints such as the mandibular joint [12]. A study found that these polymers were slightly osteogenic and were completely resorbed once replaced by newly grown bone [13].

Other lines of research that bioresorbable materials are being utilized are in the field of bone and tissue repair or replacement instead of solely fixating. Bioresorbable polymeric scaffolds have an excellent potential for revolutionizing the way bones, cartilage, and musculoskeletal tissues can be printed and replaced in the human body [14]. The scaffolds would be used to promote cell growth of the host's own newly made cells as a replacement for defective or absent tissues. These scaffolds are different from the stabilization plates and screws because the original tissue is wholly or partially removed and replaced with the 3D printed construct. The human body has a remarkable ability to repair itself after it has sustained damage. Tissues tend to be more comfortable and more quickly improved when compared to bone.

### 1.4 Multifunctional Bioresorbable Implants

An implant can be deemed multifunctional if it performs more than a singular primary purpose, for example, structure and active regeneration. To facilitate a bifunctionality such as this, the bone plate would have to contain a substance that promoted cell proliferation and differentiation. Various components that facilitate new bone growth, which acts as a repair mechanism for the damaged bone. Some of these components include growth factors or morphogenetic protein, and when coupled with an adequate blood circulation near the site, new bone can be formed [15]. The particular growth factors and morphogenetic protein typically being utilized for osteogenic and chondrogenic development were TGF-β1, TGF-β2, TGF-β3, and BMP, respectively [15].

Several release mechanisms are available for releasing drugs, proteins, or growth factors encapsulated in implants. Uhrich et al. (1999) researched different mechanisms to release beneficial drugs encapsulated in polymers [16]. Diffusion controlled release involves an insoluble polymer with a complex pore structure in which the encapsulated drug must navigate to reach the surface to become active [16]. Flow regulated release is mainly controlled by osmotic pressure in the host's body using a semipermeable polymer [16]. External pressure is exerted onto the polymer, causing the polymer to release some of the internal drugs, which it was embedded to equalize the pressure [16]. Typically, controlled release involves a release of drugs at a constant rate. The polymer encapsulated drug is controllably released through a system of premade channels in a dissolvable polymer [16].

Studies have shown that the concept of bioresorbable polymers embedded with growth factors such as TGF-β promotes bone growth and repair [17]. Bioresorbable

materials can be made to release these growth factors with a precise dosage over some time [15]. Furthermore, it was concluded that the soft tissue's success rate to bone repair could be improved by further exploring suturing implants composed of tri-calcium phosphate and poly-etheretherketones.

The surface erosion mechanism closely resembles the mechanism that we are aiming to achieve. Hydrolysis occurs for the outside moving inward, releasing the encapsulated substance in specific dosages over some time [16]. The release of the growth factors from halloysite over time due to the polymer's biodegradation and the subsequent resorption of the polymers' monomers is the main focus of my research.

## 1.5 Halloysite Nanotubes

### 1.5.1 Properties

Halloysite is a natural occurring aluminosilicate that is mined in several locations around the world. It self-assembles into a hollow tube shape when exposed to water known as a halloysite nanotubes (HNTs). HNTs have an inner lumen diameter of 15-20 nm, an outer diameter of 30-70 nm, and a length of 100-2000 nm [18]. The alumina layer of the outer surface of the HNT is negatively charged and the surface of the inner lumen has a silica layer that is positively charged. The charged surface of HNTs allow for surface modification by attaching ions, ligands surfactants, or polyelectrolytes. Substances with an overall positive or neutral charge such as antibiotics, proteins, and hormones can be loaded inside the lumen. HNTs can hold approximately 10% by volume most substances that are able to fit into their lumen via vacuum loading.

### 1.5.2 Biocompatibility

Based on a numerous amount of research HNTs have been shown to be biocompatible and non-cytotoxic [18]. Extensive research was conducted to explore the use of HNTs as delivery systems for antimicrobial and chemotherapeutic agents due to their sustained release over time. Cell cultures using fibroblast, pro-osteoblast, and mesenchymal stem cells done by our research team have shown no cytotoxic effects due to HNTs.

## 1.6 Growth Factors

### 1.6.1 TGF β1

Transforming growth factor-beta 1 (TGF β1) is one of many growth factors released during bone resorption mediated by osteoclast. Growth factors are released during this process of bone degradation to facilitate the formation of newer, more healthy bone tissue [19]. Tienlinen et al. (1999) demonstrated that when TGF β1 was delivered directly to an affected area by a degradable lactide pin, aided in bone formation [17]. TGF β1 is an abundant growth factor in the bone matrix that is released to stimulate the migration of bone marrow-derived mesenchymal stem cells to the site of bone resorption by the osteoclasts [19].

The effects of having an abundance of TGF β1 due to its release and activation by osteoclasts have an impact on deterring activity of more osteoclast as a way of balancing the degradation of bone. Metered distribution of TGF β1 is needed because overexposure to TGF β1 over an extended time can lead to excessive bone thickening because of the inhibition of osteoclast precursors, thus disrupting a healthy bone regeneration cycle [19]. Mutations in TGF β1 or the genes that encode for it are major factors in developing

several diseases that can lead to deafness, blindness, or induced myopathy due to overly dense bones [17], [19].

### 1.6.2 TGF β2

Using TGF β2 specific gene-probes, Millan et al. (1991) showed that the expression of TGF β2 is present mainly in the chondroblast zones of long bones and not in mature cartilage or areas of endochondral or intramembranous ossification [20]. Growth in these zones is characteristic of average pre-adulthood growth plate growth. Similarly, Schmid et al. (1991) used a TGF β2 riboprobe to explore the expression of TGF β2 and found that it was mainly present in growth zones of limbs in a study done on mice during embryogenesis [21]. These studies suggest that TGF β2 is an initiator of chondrogenesis and ossification in some bone regions. Additionally, cell proliferation was elevated in coronal sutures and calvarial bones when exposed to TGF β2 [22].

### 1.6.3 TGF β3

The primary mesenchymal stem cell (MSC) response to TGF β3 is an increase in cell proliferation. More specifically, James et al. (2009) showed that TGF β3 could affect chondrogenesis by enhancing the chondroprogenitor cell expression [23]. Matsike et al. (2015) developed a method using TGF β3 to differentiate MSCs into chondrocytes [24]. In both cases, TGF β3 was isolated and introduced to stem cells and successfully showed cell proliferation and differentiation in the pathway that resulted in chondrogenic formation. Kim et al. (2012) showed that a slow, sustained release of TGF β3 over nine weeks had comparable results as the growth of cells exposed to a high concentration immediately [25].

### 1.6.4 BMP2

Bone morphogenetic proteins are widely used as a stem cell differentiator for chondrogenesis and osteogenesis. Bone morphogenetic protein 2 (BMP2) is one of many cytokines that can cause MSC to differentiate into osteoblasts when used in *in vitro* experiments and induce *in vivo* bone growth [26]. BMP2 activates skeletal-related genes for the formation of cartilage and bone in more than just mesenchymal cells [27]. BMP2 exposed stem cells showed early stages of commitment and differentiation to the osteoblast phenotype [27]. Katagili et al. (1994) showed that BMP2 could differentiate myoblasts into osteoblast when implanted into muscular tissue [28].

### 1.6.5 Silicon Nitride

Silicon nitride is being explored for its ability to differentiate cells into bone. It is currently being used clinically due to its characteristic non-cytotoxicity and robustness [29]–[32]. A study conducted by Guedes e Silva et al. (2007) showed osteogenic growth due to silicon nitride through the presence of newly formed bone bridges that grew towards and on the surface of the implant [29]. Pezzotti et al. (2017) confirmed through histomorphometric analyses that the growth of new bone was due to silicon nitride degradation and subsequent ion release as demonstrated by Fourier-transform-infrared (FTIR), Raman, and X-ray photoelectron spectroscopy.

Silicon nitride particles have shown that they dissolve in polar liquids such as phosphate-buffered saline or blood. Adsorption of the silicon nitride components into blood plasma indicated an excellent acceptance of into the body with a relatively low immune response [30]. The subsequent release of silicic acid and nitrogen compounds from the breakdown of silicon nitride enhanced in vitro cellular activity [33]. Cappi et al.

(2009) demonstrated the cytocompatibility of silicon nitride with live/dead staining of human mesenchymal stem cells and mouse fibroblast cells in a cell culture study [34]. Not only is silicon nitride non-toxic, but it encourages cell adhesion, differentiation, and normal proliferation [35]. The results of a survey conducted by Pezzotti et al. (2017) connected osseointegration behavior with Si and N elements, which stimulated progenitor cell differentiation and osteoblastic activity, ultimately resulting in accelerated bone ingrowth [33]. Guedes e Silva et al. (2007) conducted a study using rabbits that revealed that silicon nitride would induce differentiation of cells into bone tissue containing osteocytes and osteons. In the 8-week study, the osteogenic process intensified at the 4-week mark [29].

Additionally, silicon nitride has shown an ability to deter bacterial growth *in vivo* while inducing the growth of healthy new bone tissue in rat studies [36]. During the investigation, Webster et al. compared the potential to grow new bone around silicon nitride, poly (ether ether) ketone (PEEK), and titanium both with and without inducing a bacterial infection with *Staphylococcus epidermidis* [36]. While the study showed a decrease in bone formation in the infected rats, there were no live bacteria adjacent to the silicon nitride, unlike in the PEEK and titanium [36].

### 1.7 Design Elements

A combination of bioresorbable polymers, halloysite nanotubes and growth factors comprised the device that aimed to replace the structural function of titanium. Careful consideration was taken to include components that would add to the effectiveness, either structurally or osteogenically. The research that was conducted aimed to solve some of the problems associated with many of the current bioresorbable

implants exhibits. Some of these challenges include a reduced ability to withstand shear forces, raw material costs, and limitations with machining the implantable material. The overall design elements were carefully chosen to develop a nanocomposite with adequate strength and flexibility to fixate bone while being able to eventually dissolve as it promotes osteogenesis or chondrogenesis, leading to full osteointegration, eventually replacing the nanocomposite with newly grown bone.

Firstly, the ratio of which polymers to blend was investigated. This was important because the nanocomposite, at the very least, must be able to stabilize the fractured bone. Secondly, we decided which morphogens to use that would drive mesenchymal stem cells to differentiate into the pathway that would eventually grow into bone or cartilage. Individual proteins from the transforming growth factor superfamily were investigated for possible inclusion in the nanocomposite design. The compound silicon nitride was also used in this study to evaluate its effectiveness in differentiating stem cells into a lineage that would result in the formation of osteocytes. The growth factors were to be contained within the halloysite nanotubes, which acted as a biocompatible nanocontainer and aided structurally within the nanocomposite.

The shape selection of the nanocomposite is of high importance to the implant's success once it is *in vivo*. Special consideration was taken to mimic the preexisting shape of titanium bone fixation plates. To facilitate the stabilization of bone post-fracture, several shapes of titanium are currently being used. Each has its inherent benefits. Selecting the appropriate size, shape, and thickness of the titanium plate is crucial. Accounting for loads on the device such as *in vivo* forces, interfacial tissue response, applied exterior load, and load transmission to the interface was of grave concern [37].

The use of screws instead of pins can be more beneficial to the implant recipient. A 10-year study conducted by Karoussis et al. (2004) showed that having a lumen within a screw-like shape was better than a hollow cylinder in terms of the overall success of the implant [38]. They remarked that their patient sample showed a significantly higher survival rate for the implant, lower instances of biological complications such as mucositis and peri-implantitis.

One of the first factors that must be determined is whether the bone and, therefore, the titanium implant, is weight-bearing. If a weight-bearing bone is fractured, the implant must be more robust to withstand the weight of the individual once they are healed. Non-weight bearing bone fractures can use thinner titanium plates, as their strength typically does not need to be as high. The infill ratio and pattern of infill as crucial as the shape of the nanocomposite. These two factors are what give the nanocomposite its strength and ability to support cell growth. A proper balance of power and the porosity, along with wall layers, had to be taken into consideration when designing the nanocomposite. For this study, we only considered non-weight bearing bone fractures. In each case, implant shape and the characteristics can have an impact on the effectiveness of an implant over time. Extensive research has been done on the shape, size, and composition of bone fixating surgical implants, as it will directly relate to the success of the nanocomposite.

# CHAPTER 2

# 3D PRINTING OVERVIEW

## 2.1 Types of 3D Printing

3D printing and additive manufacturing are terms that encompass several different techniques to take a material and form it into a construct. These constructs are typically designed using a rendering software that plans the printer's every movement and produces a printing code. Some of the techniques include powder bed inkjet printing, stereolithography (SLA), selective laser sintering (SLS), electron beam melting (EBM), and fused deposition modeling (FDM). Each printing technique has benefits, drawbacks and limitations.

### 2.1.1 Powder Bed Inkjet Printing

In powder bed inkjet printing, the print head deposits a binding liquid, layer by layer, in a predetermined pattern onto a bed of powder according to the computer-aided design (CAD) instructions. The binding liquid is then covered in a thin layer of powder to complete the section. The process is repeated until the model is complete, with each successive layer bound to the previous layer. The next step is to de-powder the model, which involves spraying, blowing, or washing the newly made model with a solvent or air to remove the unbound powder. The main drawbacks for powder bed inkjet printed objects are that they are highly porous, ununiform ,can be brittle, or may require additional steps for curing [39][40]. Powder bed inkjet printing is not suitable for this

application without further research done on the interaction of biodegradable binding liquid and a powdered blend of polymer, growth factor and growth factor container.

### 2.1.2 Stereolithography

Stereolithography (SLA) is a 3D printing technique that uses a photochemical process to bind oligomers and monomers to produce longer polymers. The light-sensitive monomers and oligomers in liquid form are exposed to light, which crosslinks them, forming a solid polymer. After a layer is photo-polymerized, the build platform is moved back to the resin pool. A new layer of oligomer and monomer mixture is coated onto the surface to begin the next layer. Hydrogels are being used to replicate soft tissues using a similar process [41]. The main drawbacks of SLA are that the polymer that is produced may not be uniformed, the final model may need additional curing, the resins are typically not biodegradable, and hydrogel prints are typically not rigid [42], [43]. These attributes rule stereolithography out as a means of manufacturing the desired nanocomposite. Stress fractures or failure of the implanted device could occur due to inconsistent polymer chains. Additional curing could damage growth factors embedded within the nanocomposite.

### 2.1.3 Selective Laser Sintering

Selective laser sintering (SLS) is a technique that uses thermal energy supplied by a focused laser beam as its primary mechanism to facilitate the sintering of substrates such as nylon or polyamides. The powdered substrate is bound together at a single point in space predetermined by 3D modeling software to construct a solid model using a beam deflection system such as Galvano mirrors. This process should not be confused with the similar technique of selective laser melting (SLM), which uses fully melted materials

instead of powders. SLS has identical drawbacks as SLA, but models made using SLS are typically less brittle than those made with the SLA printing method [44]. Selective laser sintering was ruled out due to the thermal energy needed for the process. A nanocomposite using silicon nitride could be made using this process.

### 2.1.4 Electron Beam Melting

Electron beam melting (EBM) is a high energy 3D printing technique in which raw materials such as wire or metal powder are placed under a vacuum and fused. The fusion is done by completely melting the substrate unlike in SLS. The process is typically done at a higher temperature than the other 3D printing techniques which aids in reducing porosity and increases mechanical properties. The main drawbacks are that EBM is generally only used for the manufacturing of metal parts, like titanium braces, due to its high-temperature demand [45], [46].

### 2.1.5 Fused Deposition Modeling

Fused deposition modeling (FDM) is the 3D printing technique that uses a continuous spool of thermoplastic filament to manufacture models. The process entails momentarily melting the thermoplastic polymer and directly extruding it onto the build plate or the previously made layer. Precise heating and cooling of the thermoplastic are vital in preventing warping, adding sufficient detail, and producing the desired porosity. There are several different designs of FDM printers, but two design parameters offer distinction between machines. The most important difference in design is the driving mechanism to feed filament to the hot end of the extruder head. Direct drive is typically less accurate than Bowden driven printers due to the added weight of the driving motor attached to the printer head. In Bowden driven printers, a Bowden tube is connected

between the feeding gear and the printer head. Direct drive printers typically have less stringing when compared to Bowden driven printers. Stringing is misprinted, extra material between two spans of a 3D print. Stringing can be minimized with fine-tuning of temperature and filament retraction distance during printing. **Figure 2-1** illustrates the difference between the two printer head styles.

The second significant distinction between 3D printers is the number of printer head freedoms. This term refers to the number of axes the print head is responsible for covering, between 1 and 3. 2 degrees of freedom is typically more accurate than 1 or 3 if one of the freedoms is in the z axis. The main drawback for FDM is that misprints are common, prints are time-consuming, and there may be a need of printing supports. The main advantages of FDM are that there is a broader range of materials that can be used with this printing method, the printers are typically less expensive, and the printing materials are less costly and readily available.

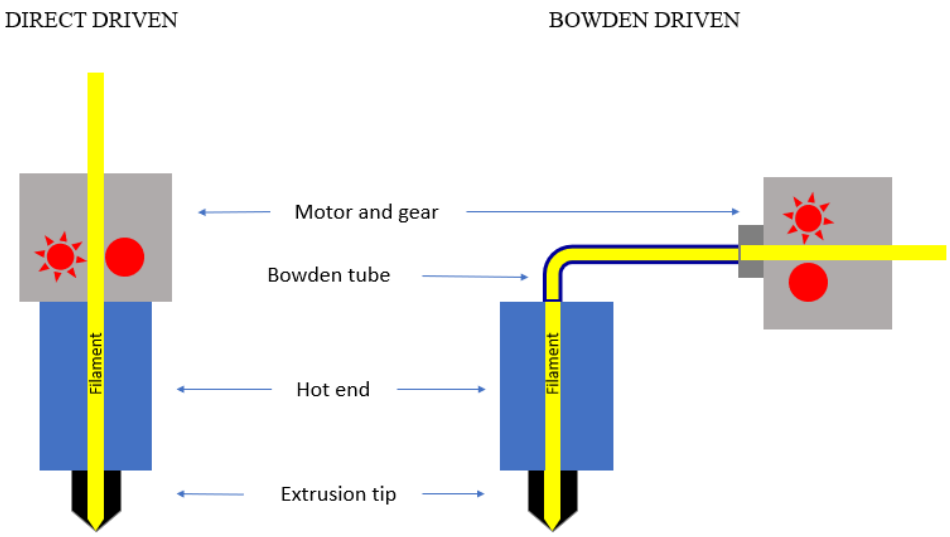


**Figure 2-1:** Illustration of the difference between direct and Bowden driven 3D printer head extruders.

## 2.2 Polymers

Polymers can be divided into two categories, biodegradable and non-biodegradable. Non-biodegradable polymers withstand breakdown under normal biological conditions. Biodegradable polymers are polymers that, when exposed to biological conditions, begin to deteriorate through a process called hydrolysis. A hydroxyl and carboxylic acid group is formed due to the hydrolysis of the ester bond of the polyester backbone [47]. There is a cascade effect in which the breaking of one monomer chain causes the breakdown of another. This is known as autocatalytic hydrolysis in which the primary reaction for the breakdown of the polymer is facilitated by the carboxylic end of the polymer at the ester bond [47]. Antheunis et al. (2010) explained that the ester bonds of both the inner and outer chains are broken in bulk hydrolysis [47]. Polymer hydrolysis can be categorized in two ways, bulk or surface. Surface hydrolysis dissolves from the surface and moves inward, while in bulk

hydrolysis, water penetrates through the surface of the polymer and dissolves the polymer at an accelerated rate in comparison [16]. A diagram illustrating the difference between the two types of erosions can be seen in **Figure 2-2.** In each case, it is the ester bond that is cleaved that facilitates polymer degradation. However, the breaking of the ester bonds is innately unpredictable yet somewhat proximal.

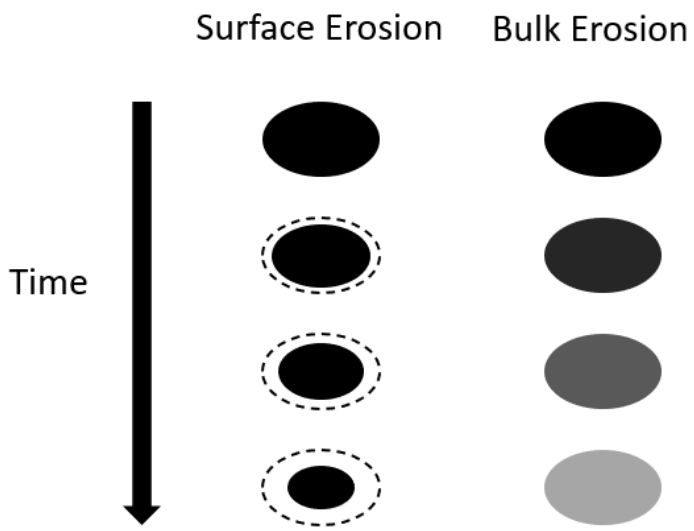


**Figure 2-2:** Illustration of the difference between bulk and surface erosion due to polymer hydrolysis.

Biodegradable polymers can further be divided into the two sub-categories of bioresorbable and non-bioresorbable. The distinction between the two is such that bioresorbable materials are classified as having the potential to partially or entirely be absorbed by cells and be utilized [48]. Several different analysis tests can determine the hydrolysis of the bioresorbable polymer. Some of these tests include lactic acid release testing, thermal property analysis and monitoring the decrease in molecular weight, all of which would be done with an *in vitro* analysis before the implant was approved for *in vivo* usage [49]. Studies have shown that the rate of hydrolysis highly depends on the

starting molecular weight [49]. Higher molecular weight polymers tend to withstand degradation longer than lower molecular weight polymers of the same material.

Due to the high molecular weight and machinability of poly-glycolic acid (PGA), it is the ideal polymer to use to manufacture bioresorbable implants such as sutures. Sutures made of PGA lose most of their mechanical properties, such as strength, in as few as 2-4 weeks post-implantation [50]. However, when PGA is not combined with other polymers, it tends to have a rapid degradation. Polylactic acid (PLA) is weaker in comparison but has a slower rate of resorption than other readily used polymers such as PGA [51]. PLA may be a better polymer than PGA as a stand-alone polymer when considering bioresorbable thermoplastics for bone mending due to its slower degradation rate. Its ability to maintain the original strength of the bone fixation device for a long time is the leading rationale behind this conclusion. While PLA undergoes bulk hydrolysis, it does so at a slower rate than PGA [16].

A combination of PGA and PLA would produce a polymer composite to make an implant that has the strengths of both polymers. Even this polymer composite is not perfect for all implant applications such as sutures, screws, scaffolds and stabilization plates. The addition of polycaprolactone (PCL) further increases the strength and function of the implant. PCL is a relatively inexpensive biodegradable polymer that has a low melting point. PCL is the least rigid of the polymers mentioned above but holds its mass *in vivo* for up to twice as long as the other two polymers [52]. Its ability to resist degradation is ushering research in its ability to become a longer-term scaffold that can release drugs, vaccines or steroids [53].

The desired characteristics of multiple polymers can be combined to make a thermoplastic superior to their constituents [54]. A nanocomposite can be constructed using a blend of various polymers in various ratios to make a polymer blend or copolymer. Polymer blends are created of two or more polymers that have been simply blended into a filament or solvent cast. A copolymer is similar, but with the addition of a polymerizing step that would combine two or more polymers into a new type of polymer.

Post hydrolysis, the polymer is broken down as if it were any other naturally occurring substance. PGA hydrolyses into glycine, while PLA hydrolyses into lactic acid [55]. The excess glycine is either excreted or converted into glucose to be used later. The excretion process for glycine is facilitated through urination. The other pathway to eliminate the excess glycine is to convert it into water and carbon dioxide by the citric acid cycle [55]. Once PLA is broken down into lactic acid, it is filtered out of the blood by the liver or kidneys and expelled in urine. Lactic acid can also be filtered out of the blood system by the liver and kidneys, where it follows a pathway to be metabolized by the Cori Cycle, which produces glucose. PCL is converted into ϵ-hydroxy caproic acid, filtered out of blood and expelled in urine. PGA will not be used in this study due to the inability to secure a supply of unprocessed polymer beads but will be included in future experiments.

## 2.3 Infill

The wall thickness, infill pattern and infill density are more important than the printing method of a 3D printed model. It is these three principles that will give the model its density, rigidity, and overall robustness. The infill pattern and density are

typically changed to adjust the print time, material consumption, density, and rigidity [56]. The three most common infill patterns are the rectangular, concentric and honeycomb patterns. Comparison and reliability test printing must be done to determine the most favorable infill density and pattern for a given model on a 3D printing machine.

The CAD file that determines the overall shape of the model while the rendering software is responsible for the infill pattern. The default settings of a printer are typically predetermined by the printer unless otherwise changed [57]. The combination of the CAD file and infill information is generally contained in the g-code file, which communicates the internal and external patterns and build plate temperature, printer head speed, filament retraction and cooling fan settings. Wall thickness is simply the number of solid layers along the parameter of the printed model. The top and bottom layers of a model are programmed differently from the wall thickness and can be as few as zero to leave the model open at the bottom or top.

# CHAPTER 3

# POLYMER MIXTURE TESTING

## 3.1 Introduction

The blending of biodegradable polymers can enhance their ability to perform mechanically [58]. The result of blending polymers can positively affect limitations which include brittleness, stiffness, toughness, and rigidity. The strengthened restrictions remain even while being enacted upon by outside stimuli such as temperature and moisture variations. Mixing PLA and PCL has the effect of harnessing the strengths of both individual polymers. The power of PLA and the flexibility of PCL combine to make a polymer blend that is rigid enough to resist bending but flexible enough to bend without breaking. The amount of flexibility in the polymer blend is directly correlated with the amount of PCL within the composite. PCL acts as a plasticizing agent that can increase the ability of a nanocomposite to withstand failure through enhanced ductility and flexibility when under strain [58].

Additionally, composites made with both PLA and PCL have displayed a property not seen in PLA or PCL in their unblended composites. Navarro et al. explained that the shape memory effect is a behavior which involves of the ability to maintain or regain the original shapes when acted upon by an outside force or condition [59]. Moreover, the shape memory is facilitated by the manufacturing a nanocomposite that has 2 or more

phases which have the responsibility to reobtain the original shape or the ability to conform to a new form [59]. The process in which the polymers bend and reform is known as programming and recovery. The programming and recovery process is characterized by the temporary deformation from the original shape and then a reformation step back towards the original shape [59]. It is thought that the multiphase design is due to the differences in the glass transition of the two polymers.

Polymer mixing of different percentages have been tested in the past. Typically, the blending process is done by mixing the polymers in heated mixer and pressed into a mold to cool [60]. The extrusion method is also used, but it is done less often due to the special equipment needed and difficulty to produce a uniformed product. Additional additives can be added to the polymer mixture to give the finished polymer blend added properties. Halloysite are one such material that has been shown to increase a variety of physical properties [61][62]. While the position and orientation of the embedded HNTs are somewhat unpredictable, their presence show several benefits such as increased strength, thermal regulation, flame retardance, and a nanocontainer/carrier.

Halloysite nanotubes are naturally occurring, one dimensional nanomaterials that resembles a hollow tube. The shape HNTs give them a high aspect ratio. Because of the nature of its high aspect ratio, HNTs make great structural reinforcers for polymers. A noticeable addition of strength has been documented by the addition of as low as 5% of total weight composite material [62]. Polymers can see an increase in stiffness, strength, and impact resistance simultaneously with the addition of HNTs [62]. The added properties of halloysite make it an important additive in the manufacturing of bone

implants, bone grafts, and bone cements [62]. In conjunction with the benefits listed above, halloysite increase the composite's ability to adhere to bone in *in vivo* studies [62].

The desired concentration of doped HNTs for this experiment was 5% and 10%. A single coating using the method below was sufficient to achieve this percentage. A double coating method was used to manufacture a polymer blend filament with 10% doped HNTs. The methods differ because the outside surface of the polymers became saturated with HNTs when coating with 5%, thus any additional HNTs would not coat the polymer beads and simply agglomerated onto the mixing container. A higher percentage of doped HNTs offer a higher ability to release dopant and possible structural strength increase.

The experiments in this chapter were performed to design parameters to manufacture an HNT embedded PLA/PCL blended polymer. The parameters include HNT percentage, extrusion of filament temperatures, and polymer combinations. The polymer preconditioning was kept constant, but the polymer composition was modified. Different ratios of the polymer were tested to determine which would give the best physical attributes to the final nanocomposite. The ratios of PLA to PCL were 80:20, 70:30, 60:40, and 100:0. The 100:0 polymer filament served as a reference to gauge the difference in physical strength due to the addition of PCL. In each case, HNTs or silicon nitride were embedded into each filament during the extrusion process. After making the filament, each iteration of the filament was printed into a testing strip using the same coding to ensure consistency. We hypothesize that a polymer blend of 80:20 PLA/PCL will exhibit similar strength but increased flexibility when compared to the PLA filament.

## 3.2 Methods and Materials

### 3.2.1 Growth Factor Hydration

Recombinant Human TGF β1, Recombinant Human TGF β3, and Recombinant Human BMP2 were purchased from ProSpec (Rehovot, Israel). Recombinant Human TGF β2 was purchased from TonBo Bioscience (San Diego, US). Each growth factor protein was hydrated according to the manufacturer's specifications. Once hydrated, each respective growth factor was diluted to make a 1 µg/ 10 ml solution in phosphate-buffered saline (PBS).

### 3.2.2 Halloysite Loading

25 mL of PBS was placed in an autoclaved 100 mL beaker with a stir bar. 25 mL of the hydrated growth factor and PBS solution was added to the PBS and stirred for 60 seconds. 5 g of halloysite nanotubes were slowly added to the beaker containing the PBS/GF solution. The solution was stirred for 5 minutes to combine. The beaker was then placed into the glass vacuum chamber and a 75 cm Hg vacuum was pulled for 5 minutes and released. The vacuum and release were done five times, shaking every minute to release trapped air bubbles. A final vacuuming step was taken for an additional 24 hours. After the final vacuuming step, any remaining liquid was aliquoted and the doped halloysite was dried in an incubator at 30°C for 24 hours. **Figure 3-1** shows a visual representation of the loading process.

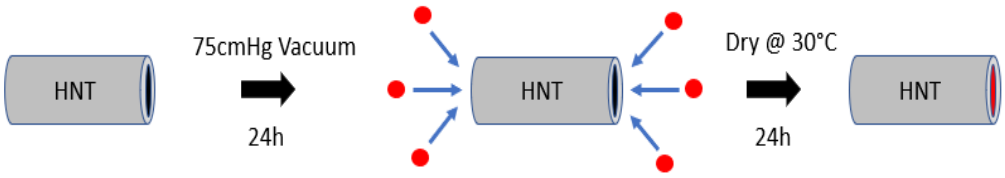


**Figure 3-1** Diagram of the loading of halloysite nanotubes process. Red dots = growth factors.

### 3.2.3 Polymer Preparation

The PLA used as a source in all blends was purchased from Sigma Aldrich and had a molecular weight of 60,000. The PCL for each combination was purchased from Aldrich Chemistry and had a molecular weight of 80,000. Each polymer was kept in a tightly sealed contain to prevent uptake of water due to humidity.

#### 3.2.3.1 *PLA : Loaded HNTs Coating*

PLA (50g) was added to a 1000 mL beaker and placed into an incubator at 45°C for 24 hours. 200 µl of silicone pump oil (SPI Supplies) was pipetted onto the warm polymer beads with a P200 micropipette. Parafilm was placed over the beaker's opening and the contents were vortexed then shaken in 60 seconds intervals respectively for a total of 6 minutes to thoroughly coat the polymer beads. The coated beads were then transferred into a clean 250 mL beaker to prevent access oil from coating the sides of the beaker, thus taking away from the coating in the next step. 2.5 g of preloaded halloysite nanotubes were added to the oiled polymer beads. Parafilm was place over the beaker. The contents were vortexed and then shaken in 60 seconds intervals, respectively, for 6 minutes to thoroughly coat the polymer beads with the loaded HNTs. The HNT coated polymer beads were placed in a 37°C incubator for 24 hours.

#### 3.2.3.2 *PLA : Silicon Nitride Coating*

PLA (50g) was added to a 1000 mL beaker and placed into an incubator at 45°C for 24 hours. 200 µl of silicone pump oil was pipetted onto the warm polymer beads with a P200 micropipette. Parafilm was placed over the beaker's opening and the contents were vortexed then shaken in 60 seconds intervals respectively for a total of 6 minutes to thoroughly coat the polymer beads. The coated beads were then transferred into a clean 250 mL beaker. 5 g of silicon nitride was pulverized using a mortar and pestle. 2.5 g of the pulverized silicon nitride was added to the oiled polymer beads. Parafilm was place over the beaker. The contents were vortexed and then shaken in 60 seconds intervals respectively for 6 minutes to thoroughly coat the polymer beads with the silicon nitride. The silicon nitride coated polymer beads were placed in a 37°C incubator for 24 hours.

#### 3.2.3.3 *PLA:PCL with Loaded HNTs Coating*

In separate containers, 40 g of PLA and 10 g of PCL, 35 g of PLA and 15 g of PCL, and 30 g of PLA and 20 g of PCL was added to a 1000 mL beaker, shaken to combine, then placed into an incubator at 40°C for 24 hours. 200 µl of silicone pump oil was pipetted onto the warm polymer bead mixture with a P200 micropipette. Parafilm was placed over the beaker's opening and the contents were vortexed then shaken in 60 seconds intervals respectively for a total of 6 minutes to thoroughly coat the polymer beads. The coated beads were then transferred into a clean 250 mL beaker. 2.5 g of preloaded halloysite nanotubes were added to the oiled polymer beads. Parafilm was place over the beaker. The contents were vortexed then shaken in 60 seconds intervals respectively for 6 minutes to thoroughly coat the polymer beads with the loaded HNTs. The HNT coated polymer beads were placed in a 37°C incubator for 24 hours.

#### 3.2.3.4 *PLA:PCL with Silicon Nitride Coating*

In separate containers, 40 g of PLA and 10 g of PCL, 35 g of PLA and 15 g of PCL, and 30 g of PLA and 20 g of PCL was added to a 1000 mL beaker, shaken to combine, then placed into an incubator at 40°C for 24 hours. 200 µl of silicone pump oil was pipetted onto the warm polymer bead mixture with a P200 micropipette. Parafilm was placed over the beaker's opening and the contents were vortexed then shaken in 60 seconds intervals respectively for a total of 6 minutes to thoroughly coat the polymer beads. The coated beads were then transferred into a clean 250 mL beaker. 5 g of silicon nitride was pulverized using a mortar and pestle. 2.5 g of the pulverized silicon nitride was added to the oiled polymer beads. Parafilm was place over the beaker. The contents were vortexed then shaken in 60 seconds intervals, respectively, for 6 minutes to thoroughly coat the polymer beads with the silicon nitride. The silicon nitride coated polymer beads were placed in a 37°C incubator for 24 hours.

#### 3.2.3.5 *PLA Double Coating*

50 g of PLA was added to a 1000 mL beaker and placed into an incubator at 45°C for 24 hours. 200 µl of silicone pump oil was pipetted onto the warm polymer beads with a P200 micropipette. Parafilm was placed over the beaker's opening and the contents were vortexed then shaken in 60 seconds intervals respectively for a total of 6 minutes to thoroughly coat the polymer beads. The coated beads were then transferred into a clean 250 mL beaker. 2.5 g of preloaded halloysite nanotubes were added to the oiled polymer beads. Parafilm was place over the beaker. The contents were vortexed then shaken in 60 seconds intervals, respectively, for 6 minutes to thoroughly coat the polymer beads with the loaded HNTs. The HNT coated polymer beads were placed in a 37°C incubator for 4

hours. The loaded HNT coated polymer beads were removed from the beaker and placed into a clean 250 mL beaker, leaving any access HNTs in the former beaker. 300 µl of silicone pump oil was pipetted onto the coated polymer beads with a P1000 micropipette. Parafilm was placed over the opening of the beaker. The contents were vortexed then shaken in 60 seconds intervals, respectively, for a total of 6 minutes to thoroughly coat the precoated polymer beads. The coated beads were then transferred into a clean 250 mL beaker. 2.5 g of preloaded halloysite nanotubes were added to the oiled precoated polymer beads. Parafilm was place over the beaker and the contents were vortexed then shaken in 60 seconds intervals, respectively, for 6 minutes to thoroughly coat the polymer beads with the loaded HNTs. The HNT coated polymer beads were placed in a 37°C incubator for 24 hours.

3.2.3.6 *80:20 PLA:PCL Double Coating*

40 g of PLA and 10 g of PCL was added to a 1000 mL beaker, shaken to combine, then placed into an incubator at 40°C for 24 hours. 200 µl of silicone pump oil was pipetted onto the warm polymer bead mixture with a P200 micropipette. Parafilm was placed over the opening of the beaker and the contents were vortexed then shaken in 60 seconds intervals respectively for 6 minutes to thoroughly coat the polymer beads. The coated beads were then transferred into a clean 250 mL beaker. 2.5 g of preloaded halloysite nanotubes were added to the oiled polymer beads. Parafilm was place over the beaker. The contents were vortexed then shaken in 60 seconds intervals, respectively, for a total of 6 minutes to thoroughly coat the polymer beads with the loaded HNTs. The HNT coated polymer beads were placed in a 37°C incubator for 4 hours. The loaded HNT coated polymer beads were removed from the beaker and placed into a clean 250

mL beaker, leaving any access HNTs in the former beaker. 300 µl of silicone pump oil was pipetted onto the coated polymer beads with a P1000 micropipette. Parafilm was placed over the opening of the beaker. The contents were vortexed then shaken in 60 seconds intervals, respectively, for 6 minutes to thoroughly coat the precoated polymer beads. The coated beads were then transferred into a clean 250 mL beaker. 2.5 g of preloaded halloysite nanotubes were added to the oiled precoated polymer beads. Parafilm was place over the beaker and the contents were vortexed then shaken in 60 seconds intervals, respectively, for 6 minutes to thoroughly coat the polymer beads with the loaded HNTs. The HNT coated polymer beads were placed in a 37°C incubator for 24 hours.

### 3.2.4 Filament Extrusion

Once the desired polymer blend was coated and heated for 24 hours, it was ready to extrude. The drying step must not be skipped to ensure the proper extrusion of the polymer beads into a filament with minimal air bubbles and entrapped water. A "Noztek Pro Filament Extruder" was used to extrude a 1.75 mm filament with a desired standard de of no more than 0.05 mm. There was no feed rate adjuster, so the temperature to achieve the specific desired filament thickness differed for every blend and additive. The extrusion temperatures are displayed in **Table 3-1**. To prevent contamination, of air bubbles or cleaning solvent from being embedded within the newly made filament, the first 5 meters were discarded as per the manufacturer's instructions. The filament was then wound into a spool and placed into a Zip Loc plastic freezing bag and placed into the freezer at -20°C until it was used for printing.

### 3.2.5 Three-Point Bend Tests

#### 3.2.5.1 *Bend Tests*

Each respective iteration of filament was 3D printed into the shape depicted in **Figure 3-2**. The wall thickness on the print was 3 layers while the top and bottom surfaces were 2 layers thick. The shape was created using TinkerCad and the G-code was written using Ultimaker Cura 3.5 software. Elasticity test were preformed using a CellScale UniVert modulator (Ontario, Canada). Each sample was placed onto the Univert testing platform and the middle point was lowered until the load was 0.02 N of force. In this test, the middle arm was moved down to 3cm at a speed of 1cm/s and retracted at 1 cm/s for a series of 5 bends for each sample. Tests were also done to a depth of 5 cm at a speed of 1 mm/s and retracted at 1 cm/s.

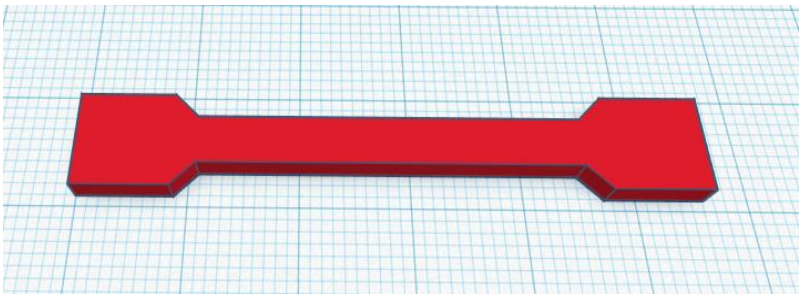

**Figure 3-2:** Rendering of the shape to make the 3D print for the 3-point bend tests. Each square represents 1 $mm^2$. The dimensions are 56 mm x 8 mm x 2.5 mm.

#### 3.2.5.2 *Failure Tests*

Each sample was printed in the same shape as the bend tests. With a similar setup as the 3-point bend test, the failure test was performed on the CellScale Univert modulator. As before, the sample was placed on the bottom 2 points and the middle threshold was lowered to a load of 0.02 N of force.

The break test was performed by moving the middle arm down at a rate of 1cm per second until the sample failed. For the safety of the machine, a maximum distance of 10cm was the programmed stopping point if a failure did not occur. Testing was done on non-degraded and degraded samples. The non-degraded samples were subjected to testing 1 day after printing. The degraded samples were exposed to PBS for 6 or 12 weeks at 37°C. During the degradation period, the nanocomposites were vortexed for 10 seconds every 48 hours. Non-degraded and degraded samples were compared to chart the loss of strength due to degradation.

### 3.2.6 Nanocomposite Degradation for Bend and Failure Tests

The nanocomposite was printed using the "Creality Ender 3 Pro" 3D printer into the bowtie shape of the bend and failure tests. Once the nanocomposite was printed, it was stored in the freezer at -20°C until all nanocomposites were ready to undergo degradation. The nanocomposites were then washed with deionized water and placed into falcon tubes with 15 mL of PBS and placed into an incubator at 37°C. The samples were vortexed every 2 days for a degradation time of 20 weeks.

### 3.2.7 Degradation Testing

The degradation profiles of each blend of the nanocomposite were also investigated. The tests were performed by placing each 3D printed nanocomposite composition into separate sample tubes containing 15 mL of PBS at 37°C. Each sample was vortexed every 48 h to ensure even degradation. The design was made to more closely mimic the outer surface that the nanocomposite would have *in vivo* once the nanocomposite was implanted and held in place as a brace and screw combination. Printing the nanocomposite with the screw holes would have given water an ability to

hydrolyze the nanocomposite from surfaces that would have been plugged. **Figure 3-3** show the shape of the 3D printed nanocomposite that was degraded for this study. Cells prefer a textured surface to attach rather than smooth surface. A textured surface was created to aid in cell adhesion. The nanocomposite was dipped in 5M sodium hydroxide for 1 minute. Readings of 6 different samples were taken every 4 weeks for a total of 20 weeks. The NanoDrop 2000c spectrophotometer was used to read the absorbances of the released monomer in a quartz cuvette. To monitor the hydrolysis of each polymer over the 20 weeks, PLA and PCL were analyzed at 230nm for PLA and 270nm for PCL. PBS was used in place of commonly used simulated body fluid (SBF) because of the long period of time used to degrade the nanocomposite. SBF needs to be changed periodically due to rising pH levels unlike PBS.

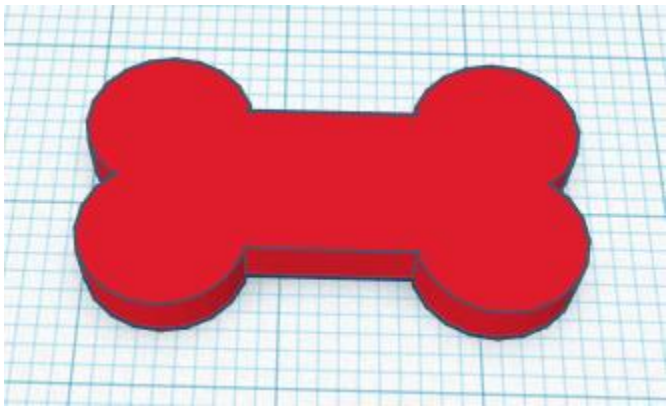

**Figure 3-3** Rendering of the shape to make the 3D print for the degradation and elution tests. Each square represents 1 $mm^2$. The maximum dimensions are 25 mm x 14 mm x 3 mm.

### 3.2.8 Statistical Analysis

Statistical analysis was performed using Microsoft Excel Analysis ToolPak plugin and Origin 9.6. All experiments were done in triplicate and with one-way analysis of variance (ANOVA) with $p < 0.05$ as the significance level was utilized for statistical analysis.

Statistically significant data was reported ($p < 0.05$), and all the results were reported as mean ± standard deviation ($p < 0.05$, n=3) unless otherwise specified.

## 3.3 Results and Discussion

### 3.3.1 Extrusion Temperature

The objective of the first experiment was to determine the optimum temperature for extrusion of filaments with 5 or 10% additive addition. Using single and double coating methods that distributes additive onto polymer beads, a filament was made using the same extruder but at different extrusion temperatures. **Table 3-1** shows each extrusion temperature and the diameter of each filament.

**Table 3-1** The extrusion temperature and diameter of each filament composition. Filament measurements were taken every meter. 30 measurements were taken to determine deviation.

| PLA:PCL | Additive | Temperature | Diameter | Tolerance |
|---|---|---|---|---|
| 100:0 | HNT | 180°C | 1.75mm | 0.03 |
| 100:0 | SiN | 170°C | 1.75mm | 0.02 |
| 100:0 | Double HNT | 184°C | 1.75mm | 0.02 |
| 100:0 | Double SiN | 170°C | 1.75mm | 0.01 |
| 80:20 | HNT | 175°C | 1.75mm | 0.01 |
| 80:20 | SiN | 172°C | 1.75mm | 0.02 |
| 70:30 | HNT | 175°C | 1.75mm | 0.03 |
| 70:30 | SiN | 172°C | 1.75mm | 0.01 |
| 60:40 | HNT | 174°C | 1.75mm | 0.02 |
| 60:40 | SiN | 171°C | 1.75mm | 0.01 |

Although the 1.75 mm filaments were made, the double-coated filament containing 10% additive was brittle and noticeable rough once extruded. However, the single-coated 5% additive filaments were flexible, and the surface was smooth. For 3D printing, the double coated 10% HNT or silicon nitride were not included in future

experiments due to the filament's abrasiveness and brittleness. The ability to make 3D prints was compromised due to the physical conditions of the manufactured filament. Only the filaments with 5% HNT or 5% silicon nitride were used for the duration of the later experiments.

### 3.3.2 Strength Testing

#### 3.3.2.1 *3-cm Bend*

Bones are designed to distribute applied mechanical loads; therefore, a brace should withstand applied stresses and strain. The 3cm bend test was more of an extreme bend than bones typically receive. Each individual blend showed a decrease in strength over time with repeated bends. **Figure 3-4** show the average of 3 different nanocomposites of each polymer blend. The error bars represent the standard deviation of each maximum force at 3cm of bend. The slopes of the peaks represent the average loss in the amount of force needed to reach a 3cm bend. A more negative slope of the trendline represents a higher degree of loss strength. The slope of the 80:20 blend was closer to zero, meaning that it showed the least amount of strength lost sue to repeated bending. The over lay of the graphs in **Figure 3-5** shows that the 80:20 needed similar force to bend the nanocomposite.

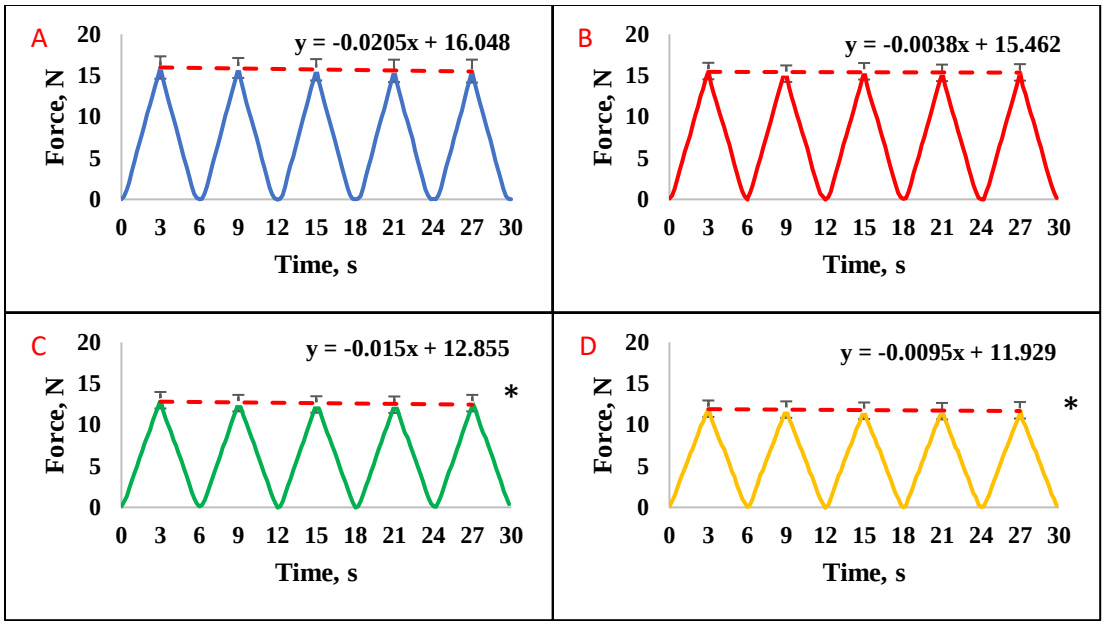


**Figure 3-4:** The graphs of the force exerted upon the nanocomposites during the 3 cm 3-point bend test for (**A**) PLA, (**B**) 80:20, (**C**) 70:30, and (**D**) 60:40 polymer blends. Error bars represent the standard deviation of the peaks. (n=3)

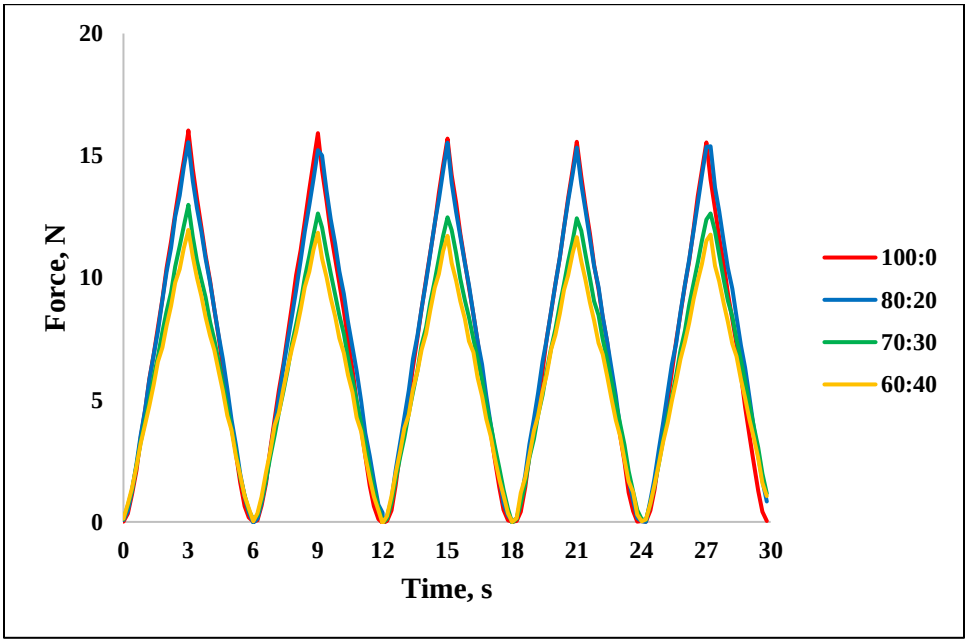


**Figure 3-5:** A composite of the forces exerted onto the nanocomposites during the 3-point bending test. Each line represents the average of 3 tests.

A composite of the force graphs for the 3cm 3-point bend test of the nanocomposite is shown in **Figure 3-5** demonstrates that with the addition of more PCL, less force is needed to reach the maximum bend length of 3cm. The graph represents an average of the forces acted upon of 3 samples per polymer blend. The outcome was predicted due to the plasticizing nature of PCL. Remarkably, the 80:20 combination showed similar strength to the PLA nanocomposite but had less loss of power after bending. The elastic effect was seen in all PCL containing nanocomposites. While the addition of PCL past 20% showed a decrease in force needed to bend, the nanocomposite's recovery and ability to sustain supplemental stress was heightened. The 80:20 blend offered the best combination of strength and flexibility with regard to the 3-point bend test.

3.3.2.2 *5-cm Bend*

A lack in reflex was observed in each iteration of the nanocomposite following the maximum bend distance. The non-linear line of the down slope of the force graph in **Figure 3-6** illustrates this fact. If an even rebound was observed, there would be less of an immediate drop in force. A 3 cm bend is an extreme deformation for a bone, much less a fixation plate, but a 5 cm bend was tested to see if the effects of the lag in reformation would remain constant or be exacerbated. The results of the 5cm bend test can be seen in **Figure 3-6**.

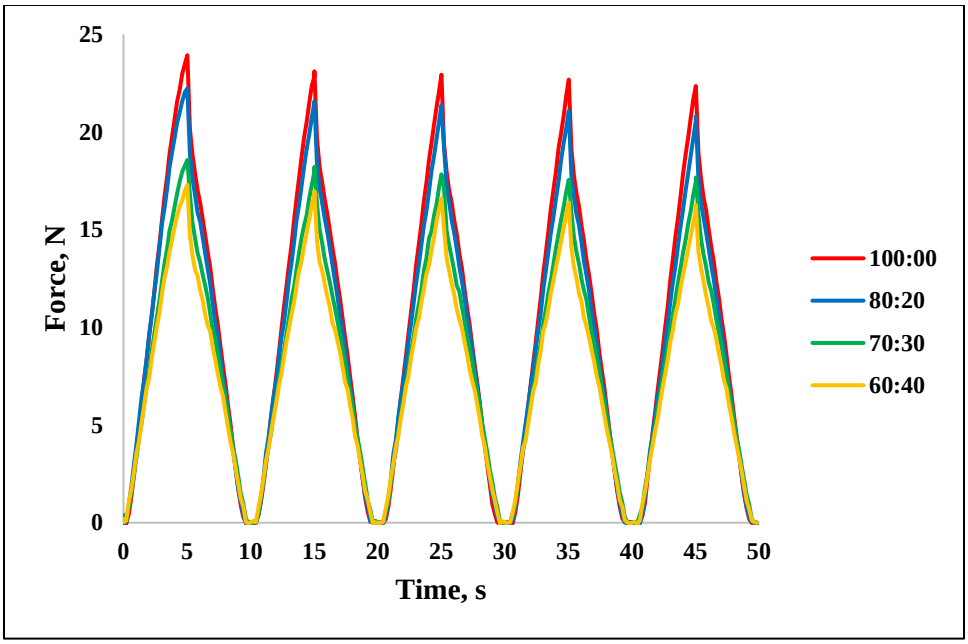


**Figure 3-6:** A composite of the forces exerted onto the nanocomposites during the 5cm 3-point bending test. Each line represents the average of 3 tests.

The 5cm bend test showed a lower ability to reform after an extreme bend, regardless of the amount of PCL present in the blend. Similar to the 3 cm bend test, the 80:20 blend showed identical properties as the PLA nanocomposite. Remarkably, a massive overall loss in strength was not observed. The evidence of this is in the force peaks. While there is a decrease such as seen in the 3cm bend, it was not as drastic.

3.3.2.3 *Break Tests*

Complete nanocomposite failure was tested on newly printed nanocomposites and nanocomposites degraded for 6 or 12 weeks. The comparison of each respective blend concerning degradation is displayed in **Figure**s **3-7**, **3-8**, and **3-9**. In these Figures, each dot represents an actual failure, and the lines represent the average forces and distances for the three test that lead to the three failures.

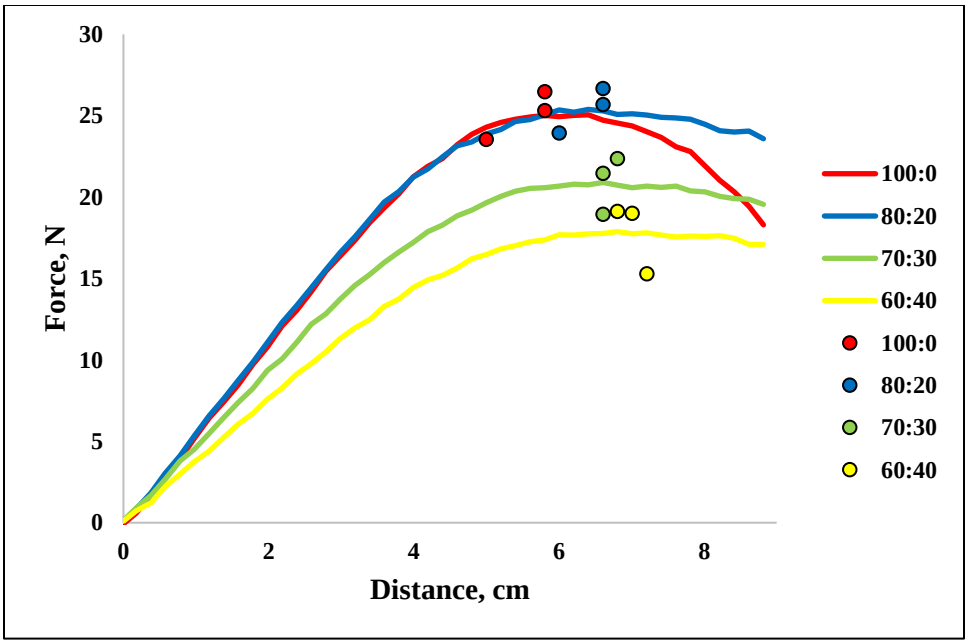


**Figure 3-7:** Force (N) to break the nanocomposite after a degradation period of 0 weeks. Each line is the average of exerted force. Each dot is the maximum force applied with respect to distance before failure.

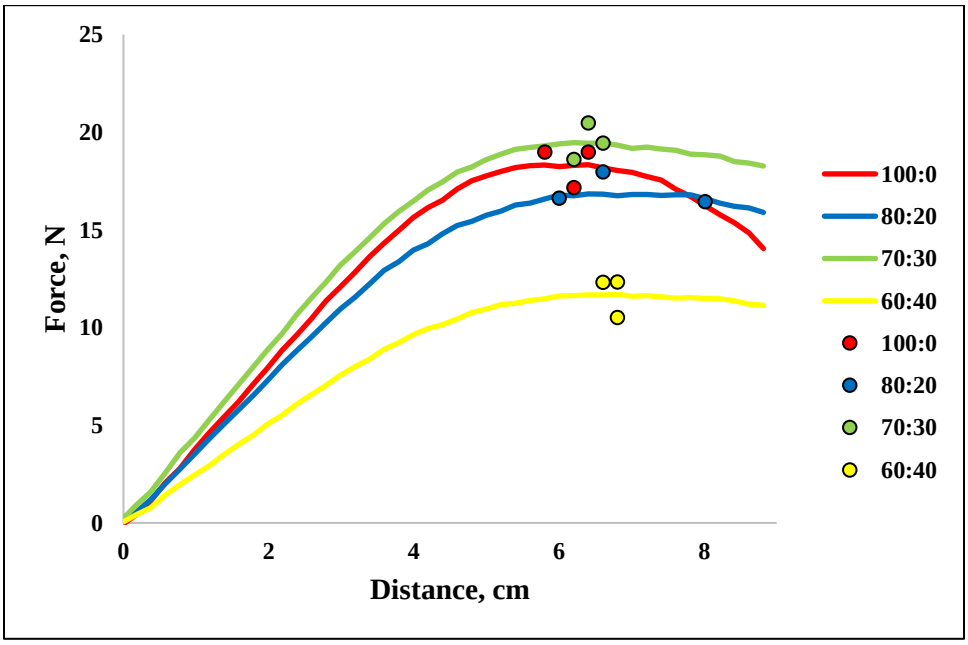


**Figure 3-8:** Force (N) to break the nanocomposite after a degradation period of 6 weeks. Each line is the average of exerted force. Each dot is the maximum force applied with respect to distance before failure.

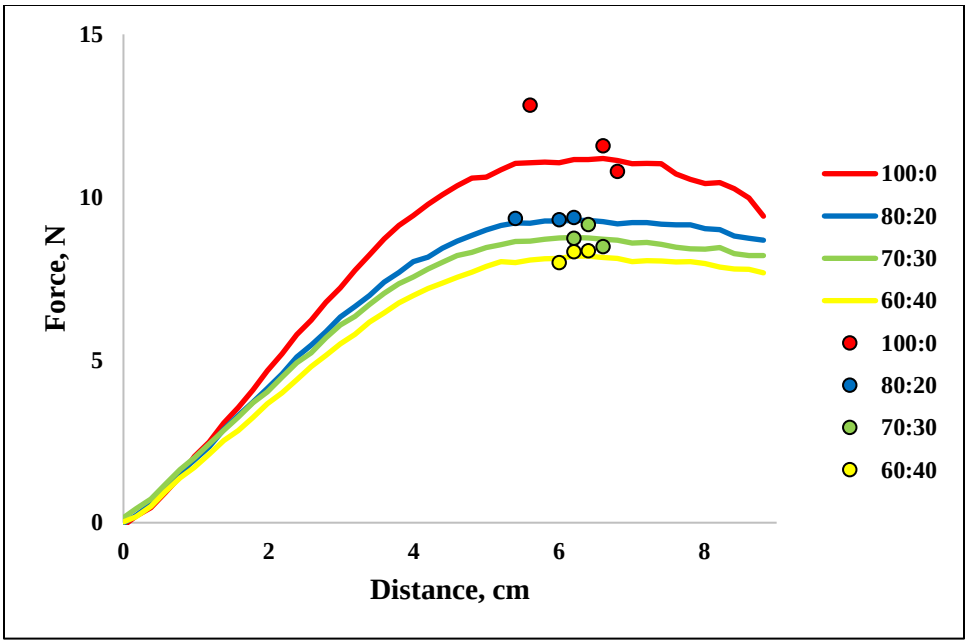


**Figure 3-9:** Force (N) to break the nanocomposite after a degradation period of 12 weeks. Each line is the average of exerted force. Each dot is the maximum force applied with respect to distance before failure.

The newly printed PLA and 80:20 blend had comparable strength, while the other combinations showed that the increase in PCL percentage made the nanocomposite weaker. The nanocomposites that were degraded for 6 weeks all showed a large decrease in strength except for the 70:30 blend. Due to the unpredictable nature of constructing the filament, a small section may have been composed of more PLA than desired. A PCL rich surface would have a slower degradation than one that had PLA more towards the surface. PLA rich filament sections could allow the nanocomposite to behave more like PLA. The nanocomposites that were exposed to PBS for 12 weeks show a much lower ability to resist force. It is speculated that the PCL in the blends is becoming either stiff or brittle due to the exposure to PBS thus losing their elastic properties. PLA experienced less loss of strength compared to the PCL containing nanocomposites. However, it should

be noted that every PLA nanocomposite had a catastrophic failure in which it was completely broken in half. PCL containing nanocomposites remained in a single piece.

The trend of having a general weakening effect as the percentage of PCL increased was once again observed. For a comparison of work needed to cause failure, and the standard deviation of each blend, see **Figure**s **3-10**, **3-11**, and **3-12**.

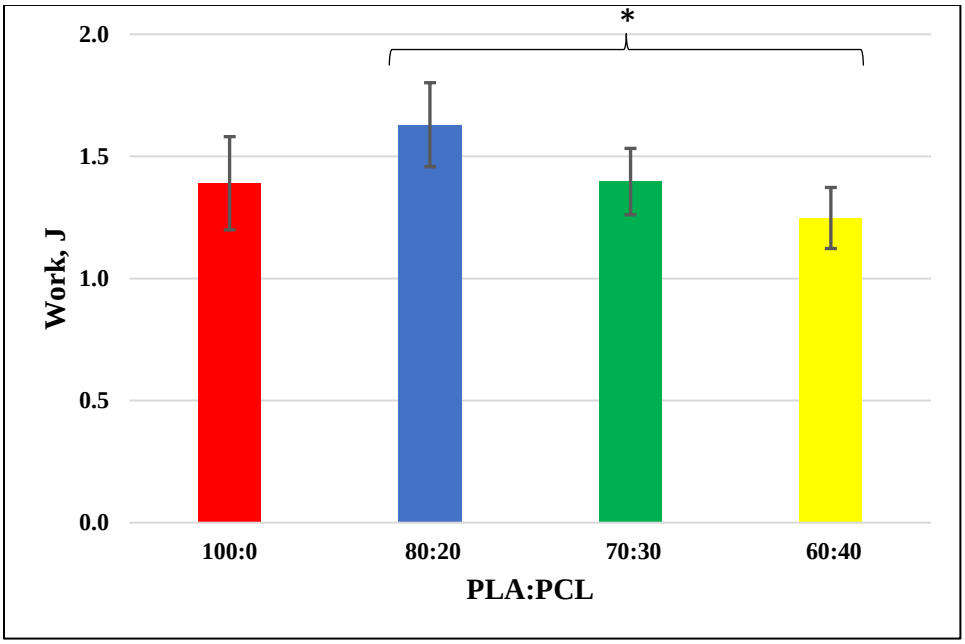


**Figure 3-10:** Average work needed to destroy the nanocomposite after a degradation period of 0 weeks. Error bars represent the standard deviation. (n=3)

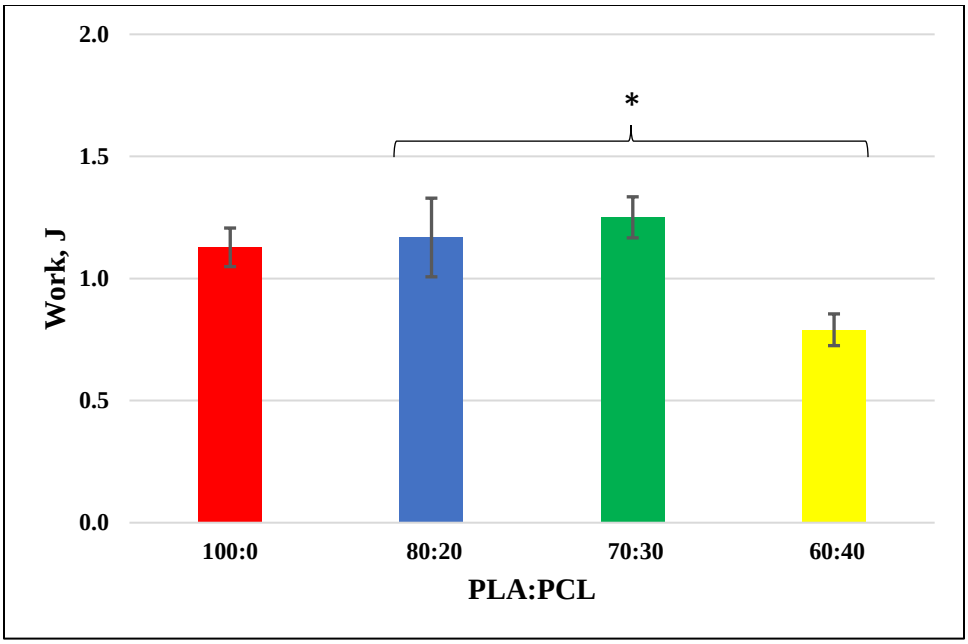


**Figure 3-11:** Average work needed to destroy the nanocomposite after a degradation period of 6 weeks. Error bars represent the standard deviation. (n=3)

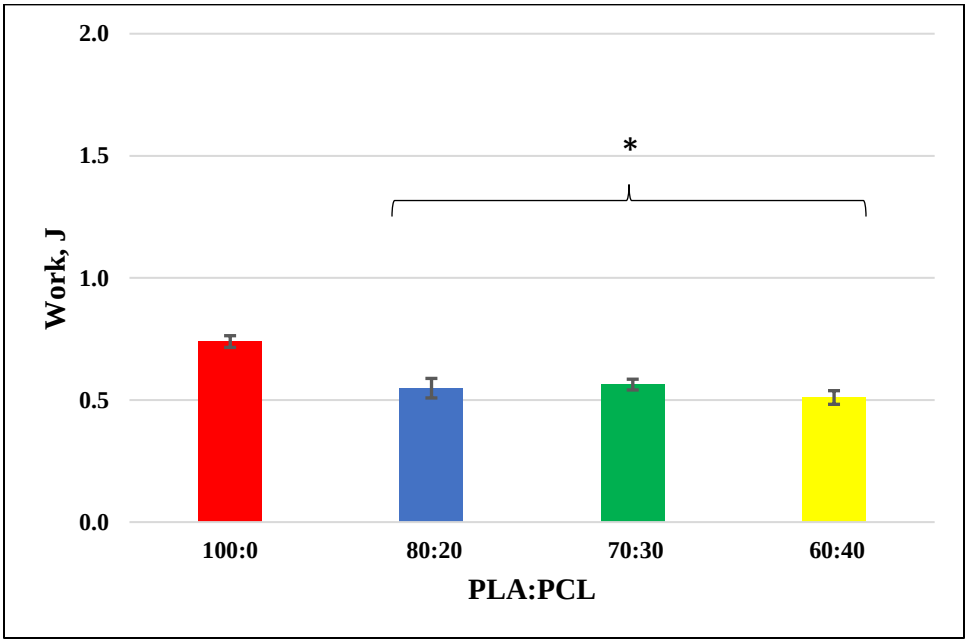


**Figure 3-12:** Average work needed to destroy the nanocomposite after a degradation period of 12 weeks. Error bars represent the standard deviation. (n=3)

The loss in strength of each respective blend can be seen in **Figure 3-13**. Each point represents the average work needed to break three nanocomposites after degradation over the 0-, 6- or 12-week periods. The slope of the trendline illustrates the degree of loss of strength and can be seen in the bottom left corner of the graph. As before, the more negative the slope of the trend line, the higher the strength loss.

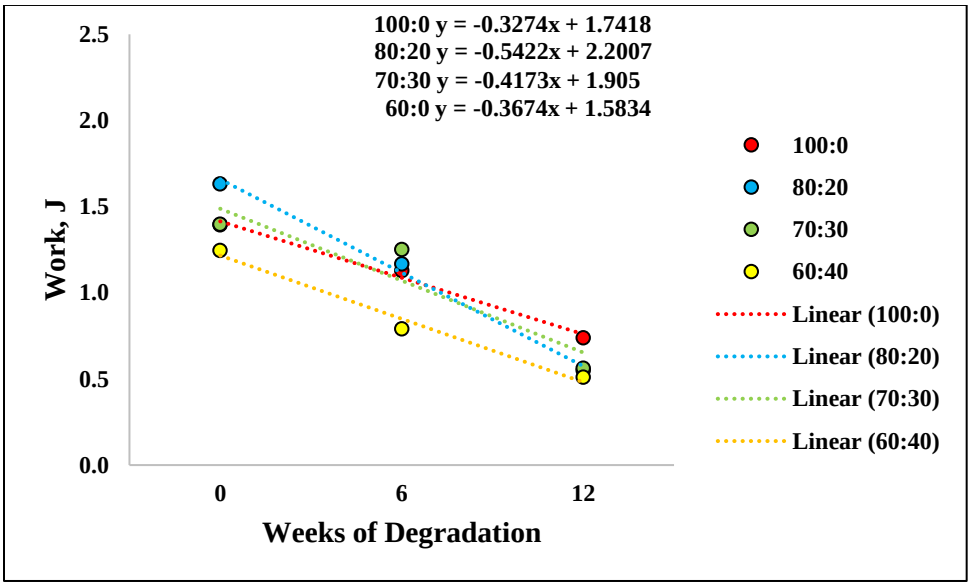


**Figure 3-13:** Graph of work needed to destroy each blend of nanocomposite after degrading for 0-, 6-, and 12-weeks. The slope of each line represents the trendline of each nanocomposite. Error bars represent the standard deviation. (n=3 for each point)

Unlike before, the strength loss was from degradation due to polymer hydrolysis did not favor the 80:20 blend. The 80:20 blend showed the least retention of strength after degradation, while the nanocomposite without PCL showed the best retention followed by the 60:40 blend. Regardless of the trend, the 80:20 blend was one of the top performers for each degradation period. The steep slope could be attributed to the higher strength of the non-degraded nanocomposite. This observation can be coupled with the

nanocomposite degrading and becoming as weak as the other nanocomposite blends over time due to degradation.

### 3.3.3 Degradation Testing

Due to the performance of the strength tests, a decision was made to exclude the 70:30 and 60:40 blends from further tests. A nanocomposite consisting of these two ratios would not be able to produce a nanocomposite with enough strength and flexibility to be effectively used to fixate bone. Degradation testing was performed on the 80:20 blend to chart the hydrolysis of each respective polymer into monomers. PLA was also tested for comparison purposes. The absorbance of the lactic acid monomers that resulted from the hydrolysis of PLA can be seen in **Figure 3-14**. **Figure 3-15** and **Figure 3-16** show the absorbances of lactic acid and ϵ-hydroxy caproic acid in PBS that was formed due to the hydrolysis of the 80:20 blend.

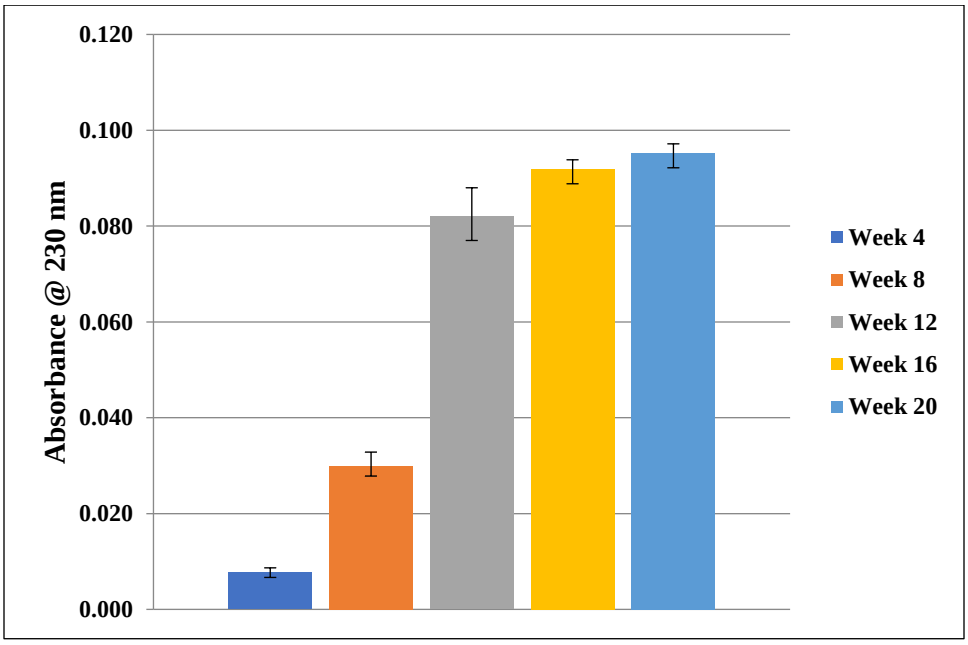


**Figure 3-14:** Absorbance recorded at 230 nm to characterize lactic acid in PBS over a 20-week period for the PLA nanocomposite. Error bars represent standard deviation. (n=6)

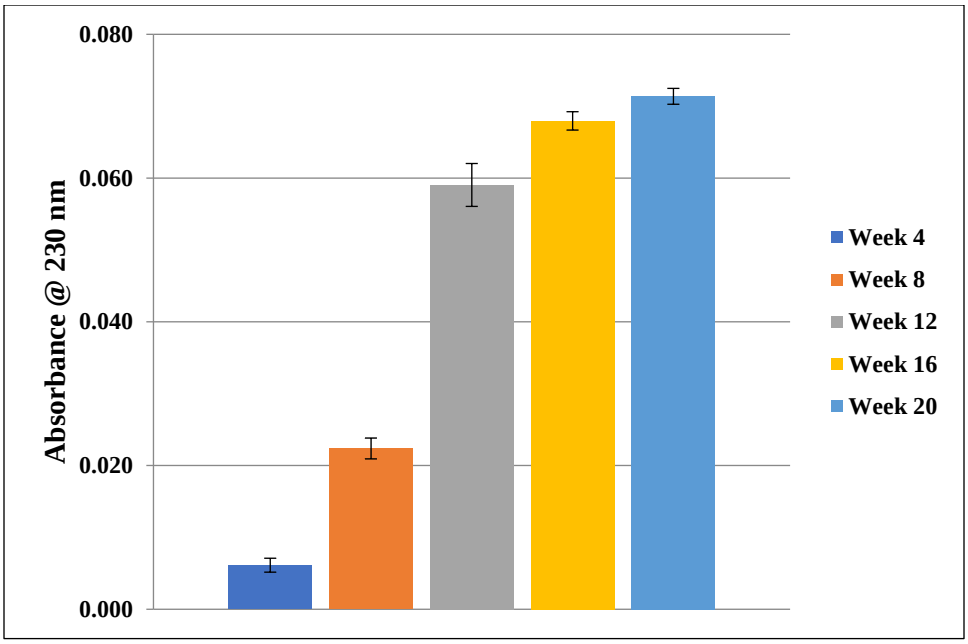


**Figure 3-15:** Absorbance recorded at 230 nm to characterize lactic acid in PBS over a 20-week period for the 80:20 blend nanocomposite. Error bars represent standard deviation. (n=6)

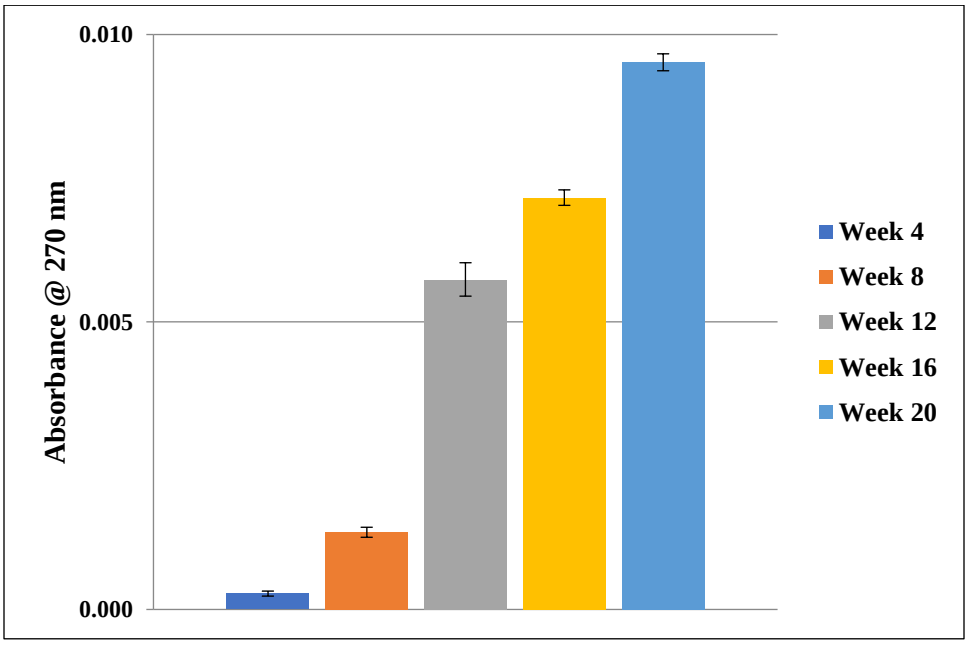


**Figure 3-16:** Absorbances recorded at 270 nm to characterize ϵ-capronic acid in PBS over a 20-week period for the 80:20 blend nanocomposite. Error bars represent standard deviation. (n=6)

See **Figure 3-17** to properly gauge the total amount of polymer hydrolysis and release of monomers from the 80:20 blend. The intensities of absorbance were combined to give a comparison to the lactic acid released by the PLA nanocomposite.

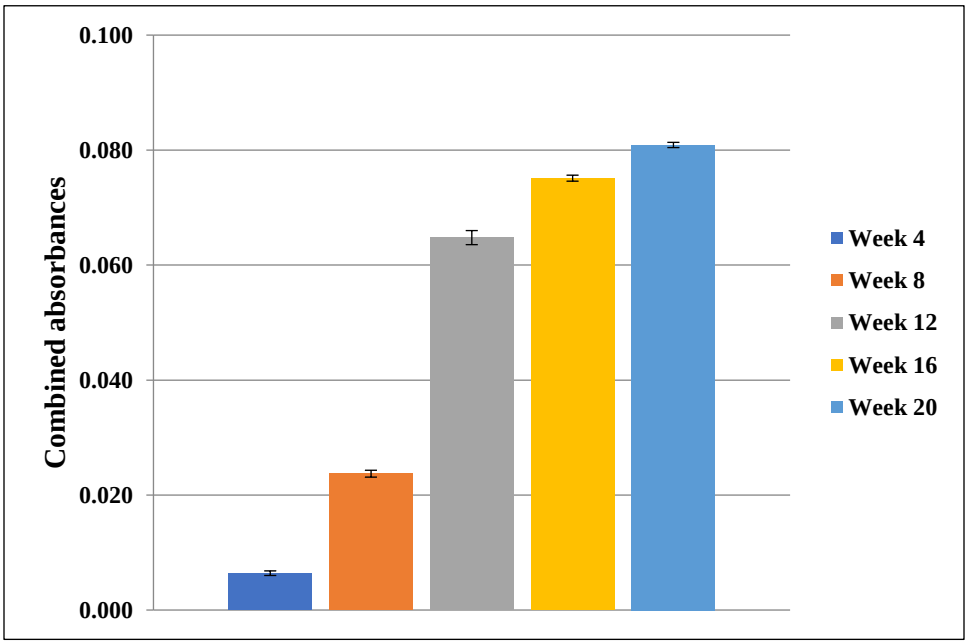


**Figure 3-17:** Absorbance values of the combined ϵ-capronic and lactic acid in PBS over a 20-week period for the 80:20 blend nanocomposite. Error bars represent the combined standard deviations. (n=6)

The amount of monomer in solution for the PLA nanocomposite were higher than the monomers released from the 80:20 blend. A comparison can be seen by looking at **Figure**s **3-18**. PCL is known to undergo hydrolysis at a slower pace when compared to PLA, and the results of this degradation study supported that statement. A comparison of the slope of each degradation rate further supports that PLA degrades faster that the PLA:PCL mixture.

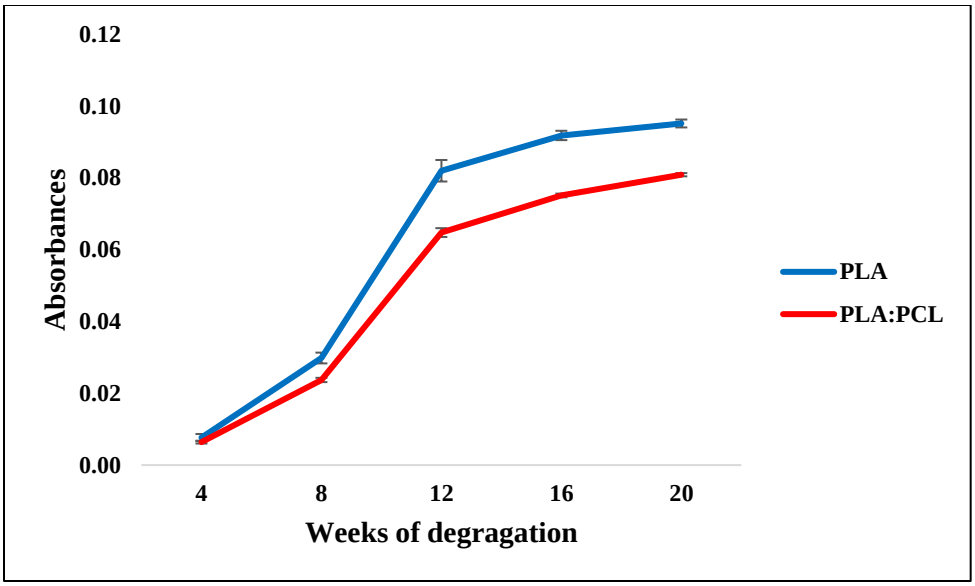


**Figure 3-18:** Graph showing the values associated with the hydrolysis of each nanocomposite. Error bars represent the standard deviation. (n=6)

### 3.4 Discussion and Conclusions

Our hypothesis was supported by the test performed in the previous experiments. PCL has been shown to increase PLA's flexibility in every test performed in this experiment. The elastic gain did not outweigh the strength lost due to the addition of PCL past the 20% threshold. A blend of PLA and PCL has similar strength and increased flexibility when compared to PLA alone. To manufacture usable filament with additives, the amount of additive must be kept to a certain percentage to create a uniform filament, suitable for 3D printing. It was found that extruding a filament with 10% HNT or silicon nitride negatively affected the filament's quality, making it unusable for 3D printing using our printers.

The amount of monomer in solution supports the expected behavior of the hydrolysis process of each polymer. PLA dissolves at a much faster rate than PLC. We can see that this principle was upheld even when the two polymers were blended and

extruded into a single filament. The combined monomer in the solution of the 80:20 blend at 20 weeks of degradation was similar to the amount of monomer released into the solution of the 100:0 polymer after 12 weeks of degradation. A slower degradation gives the nanocomposite an ability to stabilize the fracture for a longer period while new bone is being formed. The additional time can increase thickness of bone due to a prolonged exposure to the growth factors that are eluted from the nanocomposite. We suspect that if the nanocomposites with higher levels of had been tested in parallel for degradation rate, it would have had a slower rate than the 80:20 blend.

Future studies will be conducted with the addition of PGA to further fine-tune the nanocomposite's strength, flexibility and degradation for a specified time length. The current problem of a readily available supply of PGA continues to exist. To further refine the nanocomposite, similar tests can be performed with PLA and PCL ratios that are close to the 80:20 blend that had the best outcome of the blends tested in this experiment. The ratios of interest for future studies of PLA:PCL:PGA are 80:15:5, 80:10:10, 75:20:5, 70:20:10 and 75:15:10, respectively. Moreover, an additional test can be performed to evaluate a condition that was not tested in this set of experiments, torque. The nanocomposite could be expected to resist rotational force due to normal bodily movements. An examination of the force needed to rotate the nanocomposite by a certain degree could be warranted. The amount of rebound to return to the original shape after torque is applied. Lastly, the rotation torque needed for the nanocomposite to fail would be tested. These torque tests can be performed on PLA, the 80:20 blend as well as any additional new blend.

# CHAPTER 4

# CELL CULTURE STUDIES

## 4.1 Introduction

Intercellular communication between cells and their environment can be enabled by cellular adhesion [63]. Leyva-Leyva et al. (2015) linked cell adhesion achieved throughout focal adhesions and osteogenic differentiation via adhesion components using CD105+ and CD105- human mesenchymal stem cells [63]. CD105 is also known as Endoglin, a cell surface glycoprotein that is part of the TGF beta receptor complex [64]. Smad2 signaling due to Endoglin expression has lead synovium-derived mesenchymal stem cells to undergo chondrogenesis [65]. Several pathways, such as Wnt, MAPK, Smad2/3, and β-catenin, have been researched as signaling pathways that promote chondrogenesis or osteogenesis in conjunction with members of the TGF beta super family [66].

Cellular attachment and exposure to the specific growth factors used in this experiment were analyzed for the ability to foster the growth of osteoblasts and chondroblasts. Alizarin Red S staining and cell viability/cytotoxicity assays were used at predetermined intervals of exposure to the nanocomposites that were eluting the growth factors, to analyze cells. Initial testing was done on the nanocomposites to determine the amount of growth factor that was released from the nanocomposites. The quantification

of the released growth factor gave insight into the amount of growth factor expected to be released and exposed to the stem cells during the cell culture studies.

Meinel et al. (2004) observed that MSCs exhibited calcium deposits, which increased over time, starting 3 weeks after culturing began. It was noted that the between weeks 2 and 3 of the culture, an increase in cell cluster sizes and intensity of staining indicating higher calcium deposits was observed suggested the initiation of bone formation [64].

We hypothesized that our nanocomposite would release growth factor or silicon nitride over time and be non-cytotoxic to mesenchymal stem cells while promoting osteogenic differentiation. The release of the morphogenic agent contained within the polymer nanocomposites have been proven to foster cell proliferation, migration and differentiation due to direct exposure.

## 4.2 Methods

### 4.2.1 FITC/BSA Release Study

The release characteristics for the 3D printed nanocomposite were tested using FITC tagged bovine serum albumen (FITC/BSA) as a surrogate for growth factors. FITC/BSA is less expensive and quantitative analysis upon using a spectrophotometer is simple and straightforward. HNTs were loaded with FITC/BSA and 3D printed in the same manner as the growth factor containing HNTs. The FITC/BSA/PLA filament was 3D printed into the dog bone shape as described in chapter 3's degradation testing using the Creality Ender 3 printer.

#### 4.2.1.1 *Making FITC/BSA Filament*

A solution of 10 µg/mL of FITC/BSA in PBS was prepared. Halloysite nanotubes (5 g) were slowly added to a 100 mL beaker containing the FITC/BSA/PBS solution. The solution was stirred for 5 minutes to combine. The beaker was then placed into a glass vacuum chamber and a 75 cm Hg vacuum was pulled for 5 minutes and released. The vacuum and release were repeated 5 times, shaking every minute to release trapped air bubbles. A final vacuuming step performed for an additional 24 hours. After the final vacuuming step, any left-over liquid was aliquoted and washed 3 times with PBS to remove any FITC/BSA that remained on the surface. The doped halloysite was then dried in an incubator at 30°C for 24 hours.

PLA (50 g) was added to a 1000 mL beaker and placed into an incubator at 45°C for 24 hours. 200 µl of silicone pump oil (SPI Supplies) was pipetted onto the warm polymer beads. Parafilm was placed over the opening of the beaker and the contents were vortexed then shaken in 60 seconds intervals respectively for a total of 6 minutes to thoroughly coat the polymer beads. The coated beads were then transferred into a clean 250 mL beaker to prevent access oil from coating the sides of the beaker, thus taking away from the coating in the next step. FITC/BSA doped halloysite nanotubes (2.5 g) were added to the oiled polymer beads. Parafilm was place over the beaker and the contents were vortexed and shaken in 60 seconds intervals respectively for a total of 6 minutes to thoroughly coat the polymer beads with the FITC/BSA doped HNTs. The HNT coated polymer beads were placed in a 37°C incubator for 24 hours. A 1.75 mm filament was made with an extrusion temperature of 180°C.

#### 4.2.1.2 *Nanocomposite Elution*

The FITC/BSA elution tests were performed by placing each 3D printed nanocomposite discs into separate sample tubes containing 2 mL of PBS at 37°C. Each sample was vortexed every 48h to ensure even degradation. The design was made to more closely mimic the outer surface that the nanocomposite would have *in vitro* once the nanocomposite was glued to a well of a 48 well cell culture plate. Cells prefer a textured surface to attach rather than smooth. To mimic the conditioning that the nanocomposite would be subjected to as a way of aiding in cell adhesion, the nanocomposite surface was slightly degraded to add texture. The nanocomposite was dipped in 5M sodium hydroxide for 1 minute. Each nanocomposite was washed with water and dried before degradation.

#### 4.2.1.3 *FITC/BSA Concentration Collection*

Forty-two 3D printed nanocomposites were degraded as described in the previous section. Measurements were taken every 4 days from 6 different samples for a total of 4 weeks. Samples were vortexed for 10 seconds prior to collection. After 2 mL of eluted FITC/BSA in PBS was collected and, the sample discarded. The sample liquid was analyzed within one hour after collection to prevent FITC/BSA degradation due to light interaction.

#### 4.2.1.4 *FITC/BSA Calibration Curve*

A calibration curve was made using FITC/BSA and PBS. 1 mg of FITC/BSA was added to 100 mL of PBS and mixed well to combine to get same amount of FITC/BSA that was in solution that was used for vacuum loading HNTs. Further dilutions from the stock 10 µg/mL FITC/BSA were used to complete the calibration curve. A series of serial

dilutions was made and measured from a concentration of 10 µg/mL down to 15.6 ng/mL using the Nanodrop 200c spectrophotometer. The results are displayed on **Figure 4-1**.

### 4.2.2 Cell Culture Media

Cell culture media was designed to give adequate nutrients to stem cells to support proliferation and future differentiation. 400 mL of Dulbecco's Modification of Eagle's Medium (DMEM) (Corning) with 4.5 g/L glucose, L-glutamine and sodium pyruvate was added to a sterile flask. 47.5 mL of fetal bovine serum (FBS)(Biowest) was then added to the DMEM. 2.5 mL of penicillin streptomycin solution (Corning) was the last media ingredient added to the flask prior to vacuum filtration to remove any large particles or contaminants. The solution was labeled "complete media" and placed into the refrigerator for storage.

### 4.2.3 Cell Culture Proliferation

StemPro human adipose derived stem cells were used as a cell source for this study. The initial cell plating was done on a ThermoFisher T-75 culture flask placed into a 37°C incubator with 5% $CO_2$. Once the confluency was between 90-95%, the cells were passaged for further proliferation. Depleted media was removed, 1 mL of 0.25% trypsin-EDTA was added to the flask and place into the incubator for 75 seconds. The flask was then gently tapped to detach any cells that remained attached to the flask. 10 mL of media was added to the flask and mixed to suspend the cells throughout the media. 1 mL of the cell and media mixture was added to a new culture flask. An additional 9 mL of media was added to each culture flask, the cap was applied loosely, and placed back into the incubator.

### 4.2.4 Nanocomposite Printing and Preconditioning

Each nanocomposite iteration was printed using the Creality Ender 3 printer. The discs had 50% infill and were cylindrical in shape. Before attaching them to the base of a 48 well plate, each nanocomposite was preconditioned by dipping them in 5M sodium hydroxide for 1 minute. Post preconditioning, the nanocomposites were washed with water thrice and dried. Each nanocomposite was plated into individual wells of a 48 well plate and secured with superglue. The superglue was allowed to cure for 2 hours before the plates containing the nanocomposites was placed under UV light for 30 minutes to kill any bacteria that may have landed on the surface.

### 4.2.5 Addition of Cells 48 Well Plate

Media was removed from each cell culture flask and discarded. 1 mL of 0.25% trypsin-EDTA was added to each flask and placed in the incubator for 75 seconds. After gently taping the flask to remove any adhered cells, 10 mL of media was added to each flask. The contents of all flasks were added to a single flask. The approximate number of cells was calculated using the Nexcelom Bioscience Auto T4 Cellometer cell counter. The flask containing the cells was diluted to have a concentration of $1 \times 10^6$ cells per mL. 1 mL of the stem cell/media mixture was added to each well that contained a nanocomposite and 3 additional empty wells as a control. The media was changed for each well every 48 hours.

### 4.2.6 Live/Dead Staining

Cell viability was tested using the Biotium viability/cytotoxicity assay kit. The staining solution was made by adding 1.25 µl of 4 mM calcein AM and 5 µl of 2 mM EthD-III to 2.5 mL of PBS. The depleted media was removed from the well and the well

was washed twice with PBS. 300 µl of the staining solution was added to each well and allowed to absorb for 1 hour at room temperature in a dark enclosure. Live cells fluoresced at 517 nm and dead cells fluoresced at 625 nm. A microscope with filters to allow specific excitation wave lengths of 494 nm and 532 nm was used.

### 4.2.7 Alizarin Red S Staining

Alizarin Red S staining was done on a plate of samples at an interval of 1, 7, 14, 22, 28, and 35 days. Each well of cells were stained with Alizarin Red S stain to determine if the cells were calcium-rich, indicating that the stem cells are beginning to or have already become pre-osteoblast or pre-chondroblasts. A 40 mM Alizarin Red S staining kit was purchased from Sigma-Aldrich. The pH of the alizarin red s was adjusted to 4.2 before use with the 10% ammonium hydroxide or 10% acetic acid included with the kit. Media was removed from each well and 300 µl of 10% formaldehyde was added to each well to fix the cells for 10 minutes at room temperature. The formaldehyde was removed, and the well was washed with 500 µl PBS twice to remove as much formaldehyde as possible. 250 µl of alizarin red s was added to each well and allowed to stain for 15 minutes at room temperature. The final step was to wash the well with water prior to observing under a microscope.

## 4.3 Results

### 4.3.1 FITC/BSA Calibration Curve

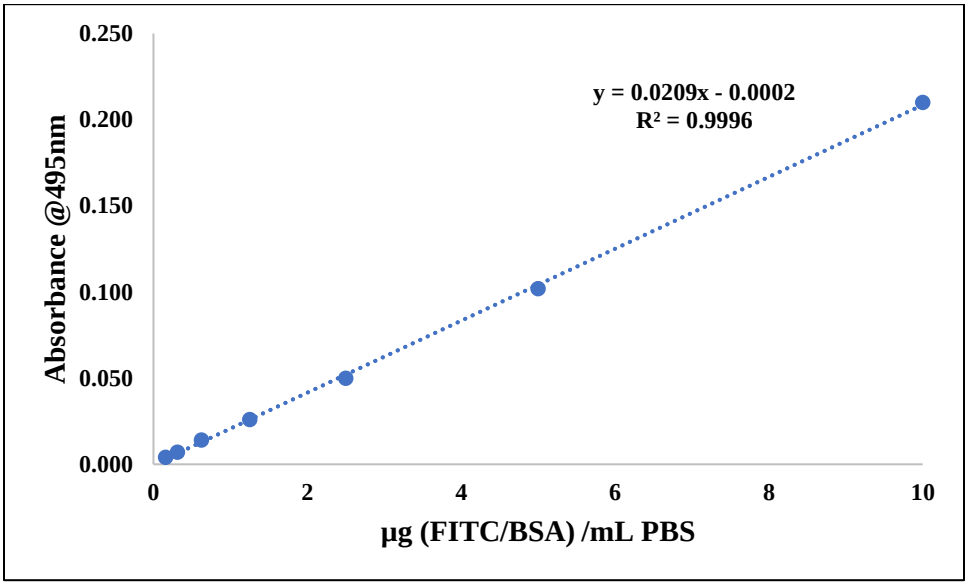


**Figure 4-1:** Graph of the calibration curve of FITC/BSA in PBS to determine the amount of FITC/BSA released from the nanocomposite over time.

### 4.3.2 FITC/BSA Released into Solution

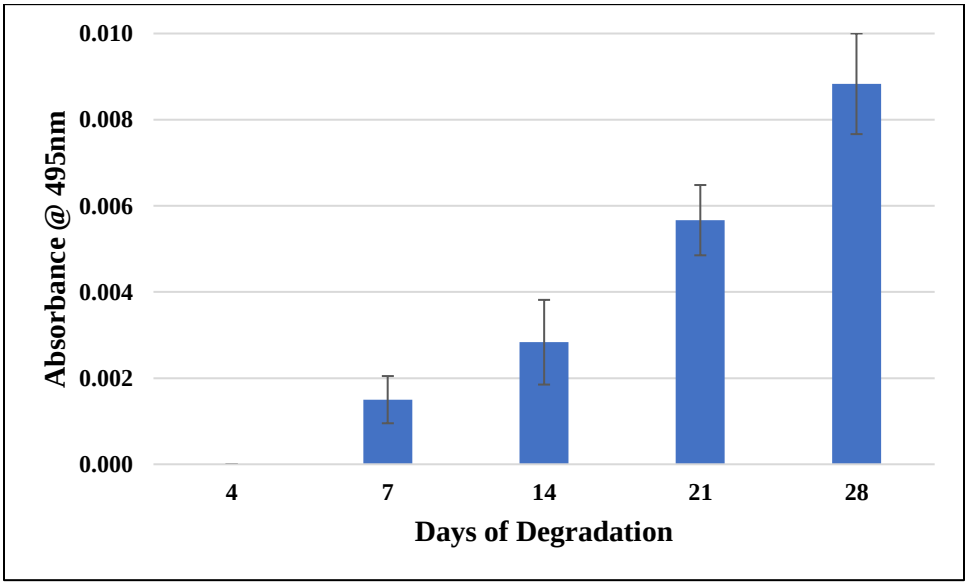


**Figure 4-2:** Graph of FITC/BSA released from cylindrical nanocomposites after degradation. Error bars represent ± standard deviation. (n=6)

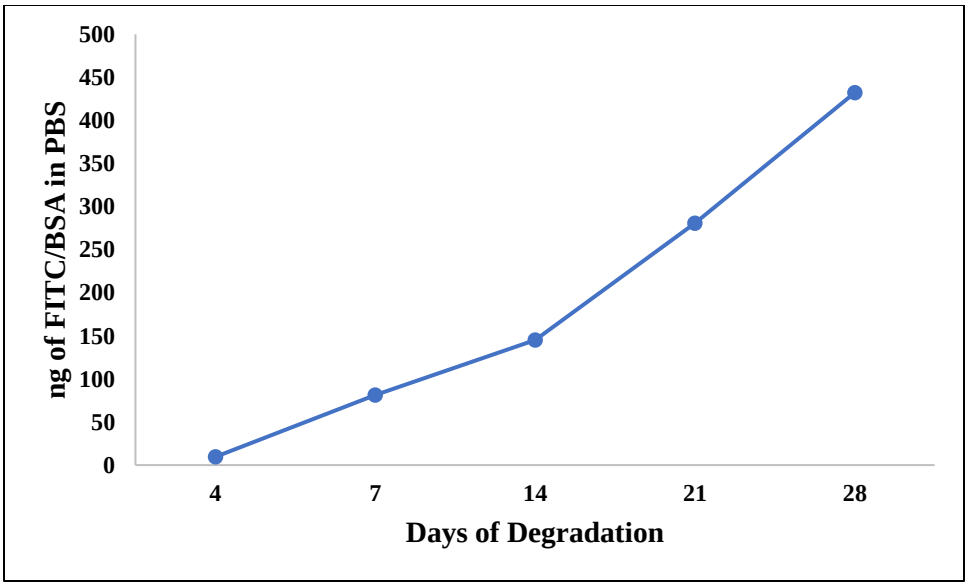


**Figure 4-3:** FITC/BSA released into solution after nanocomposite degradation over 4-weeks. (n=6)

4.3.3 Live/Dead Staining

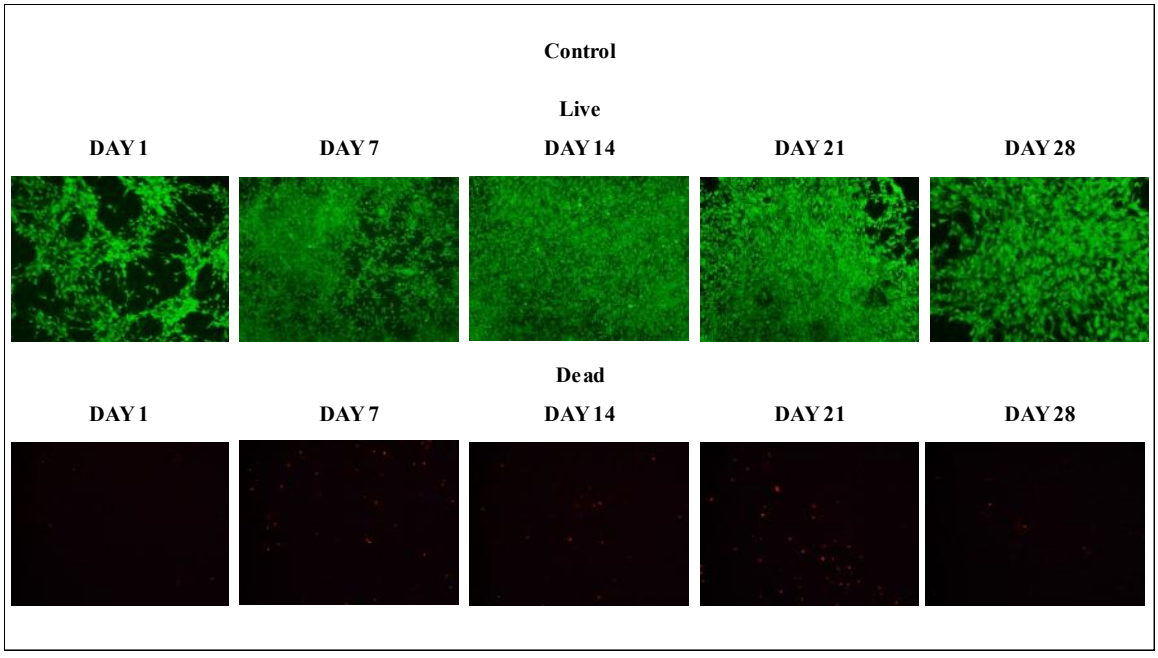


**Figure 4-4** Live dead assay of the control wells showing the live cells in green on top image and dead cells in red on the image below for day 1, 7, 14, 21, and 28.

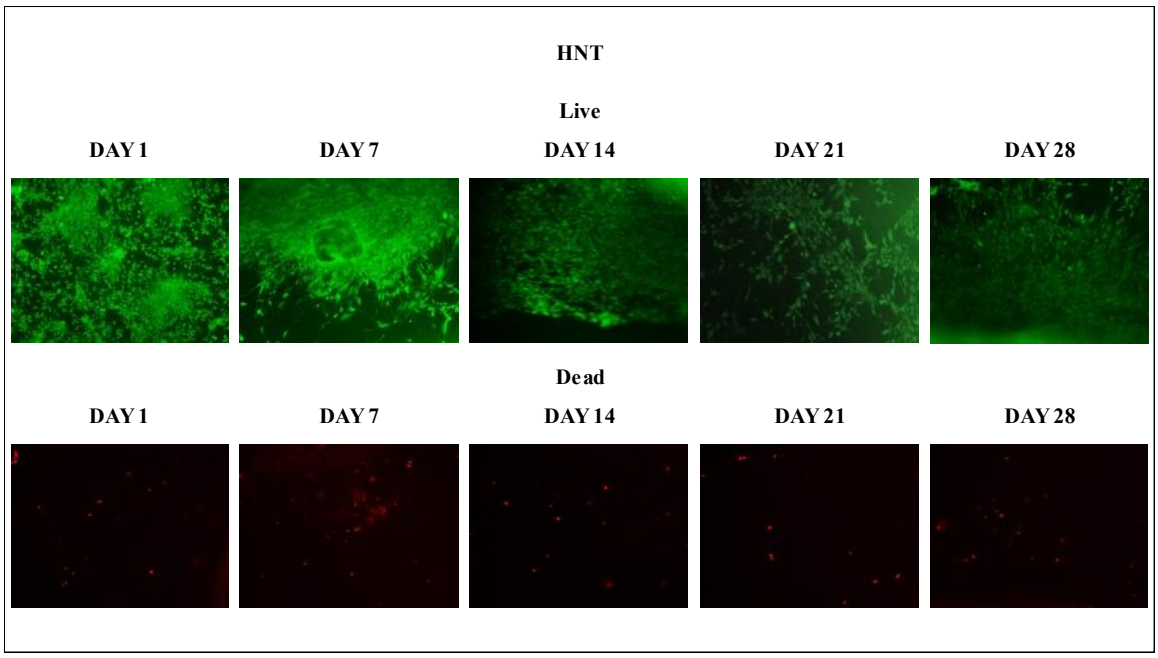


**Figure 4-5:** Live dead assay of wells containing HNT\PLA discs showing the live cells in green on top image and dead cells in red on the image below for day 1, 7, 14, 21, and 28.

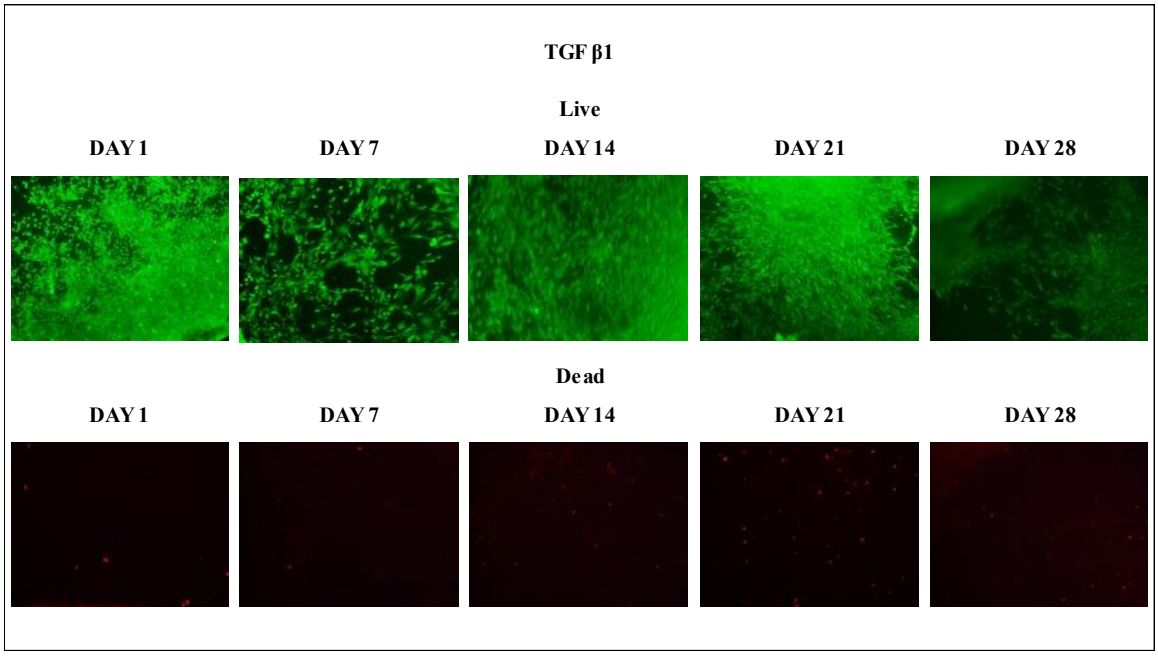


**Figure 4-6:** Live dead assay of wells containing TGFβ1\PLA discs showing the live cells in green on top image and dead cells in red on the image below for day 1, 7, 14, 21, and 28.

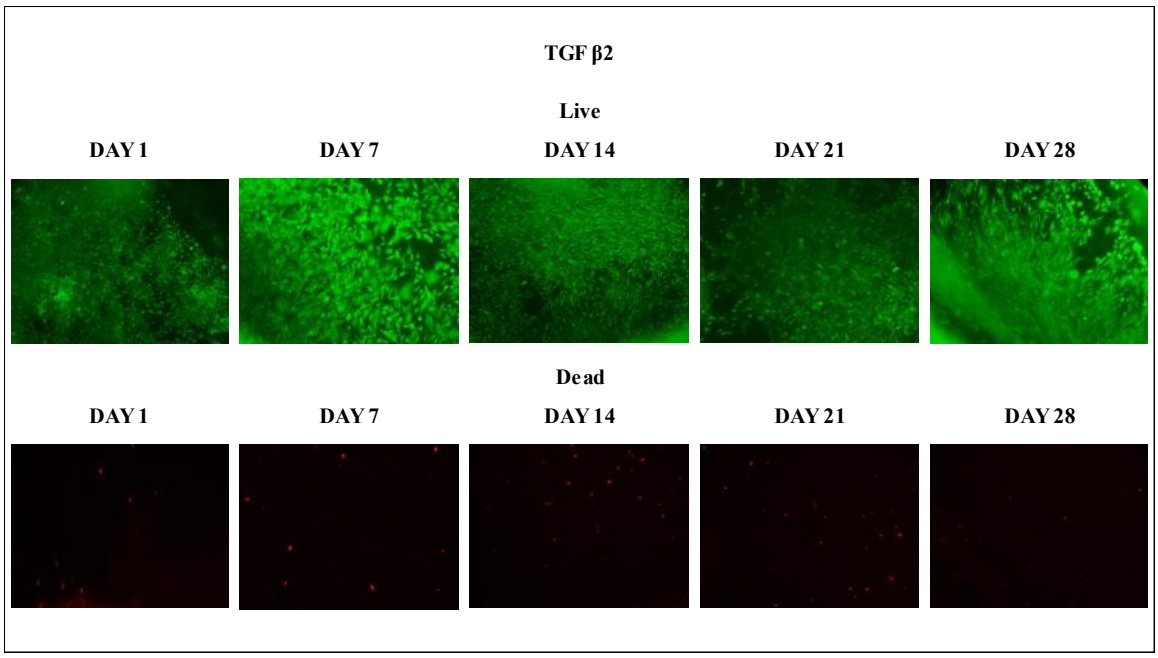


**Figure 4-7:** Live dead assay of wells containing TGFβ2\PLA discs showing the live cells in green on top image and dead cells in red on the image below for day 1, 7, 14, 21, and 28.

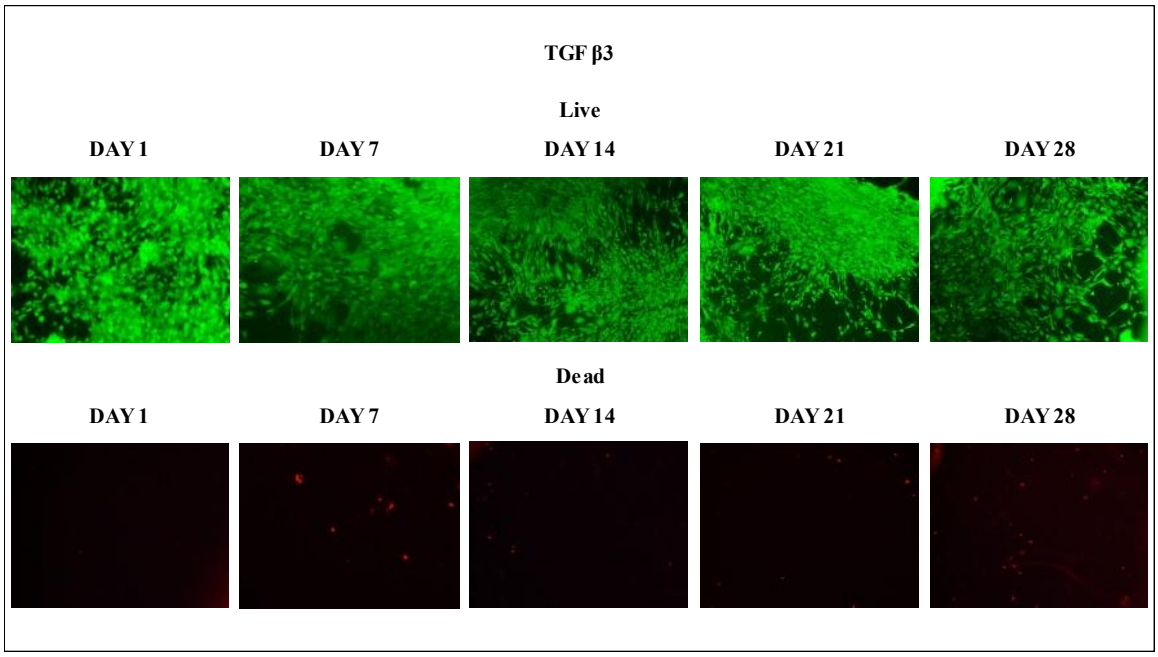


**Figure 4-8:** Live dead assay of wells containing TGFβ3\PLA discs showing the live cells in green on top image and dead cells in red on the image below for day 1, 7, 14, 21, and 28.

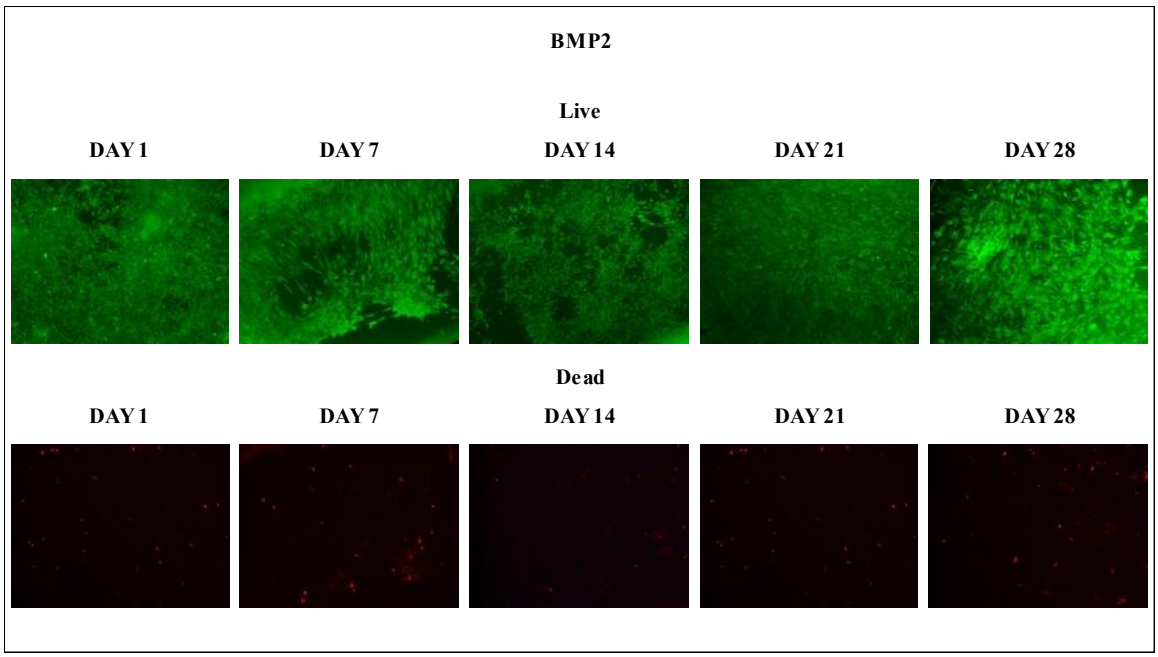


**Figure 4-9:** Live dead assay of wells containing BMP2\PLA discs showing the live cells in green on top image and dead cells in red on the image below for day 1, 7, 14, 21, and 28.

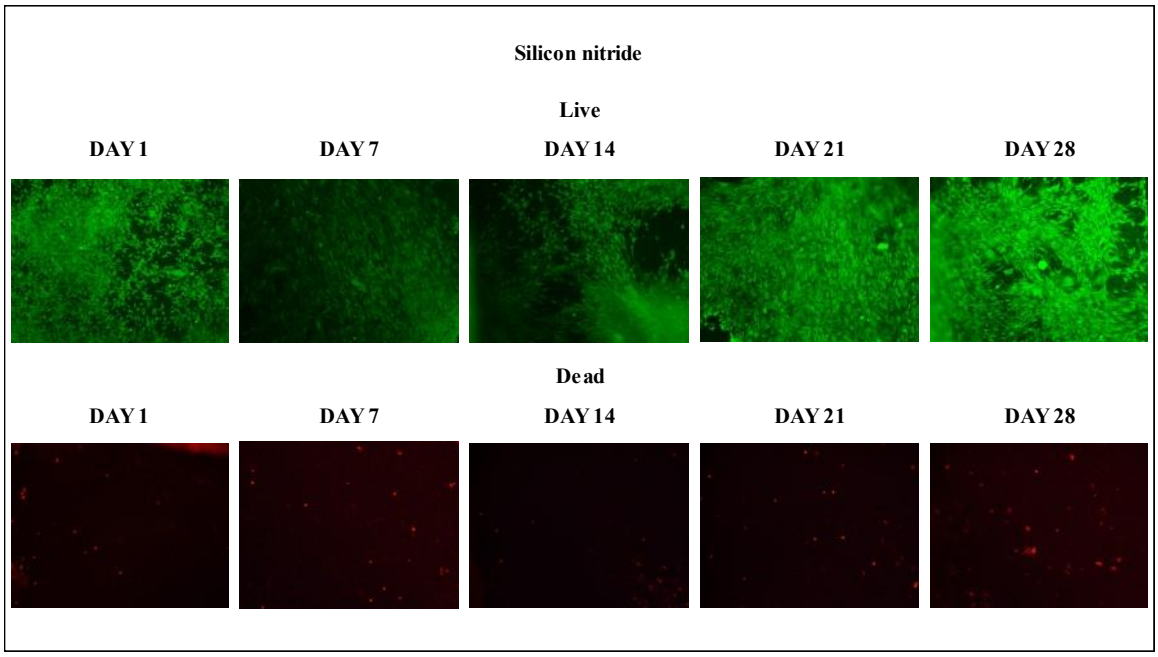


**Figure 4-10:** Live dead assay of wells containing silicon nitride\PLA discs showing the live cells in green on top image and dead cells in red on the image below for day 1, 7, 14, 21, and 28.

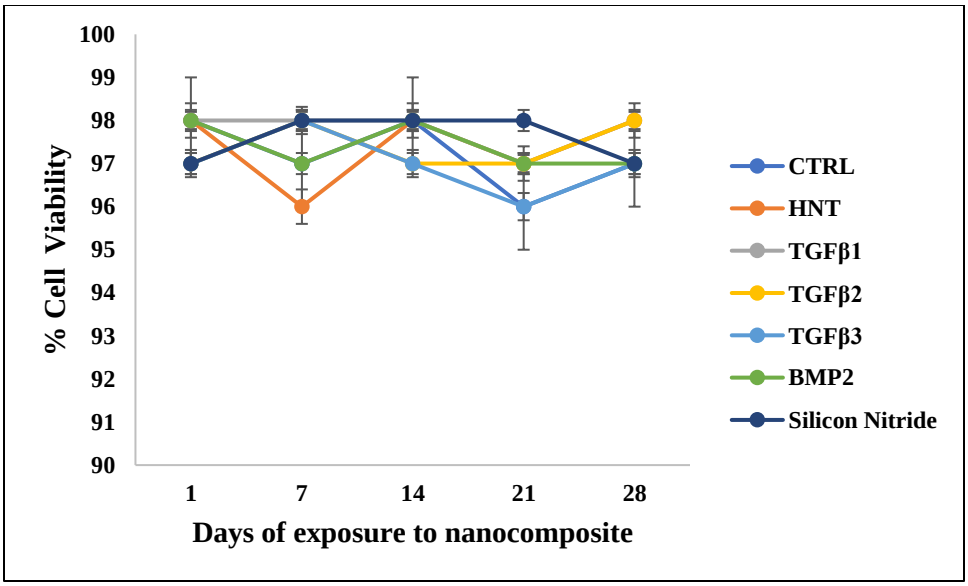


**Figure 4-11:** Graph showing the quantitative values of cell count calculated ((live - dead) / live). Error bars are standard deviation where n=3.

### 4.3.4 Alizarin Red S Staining

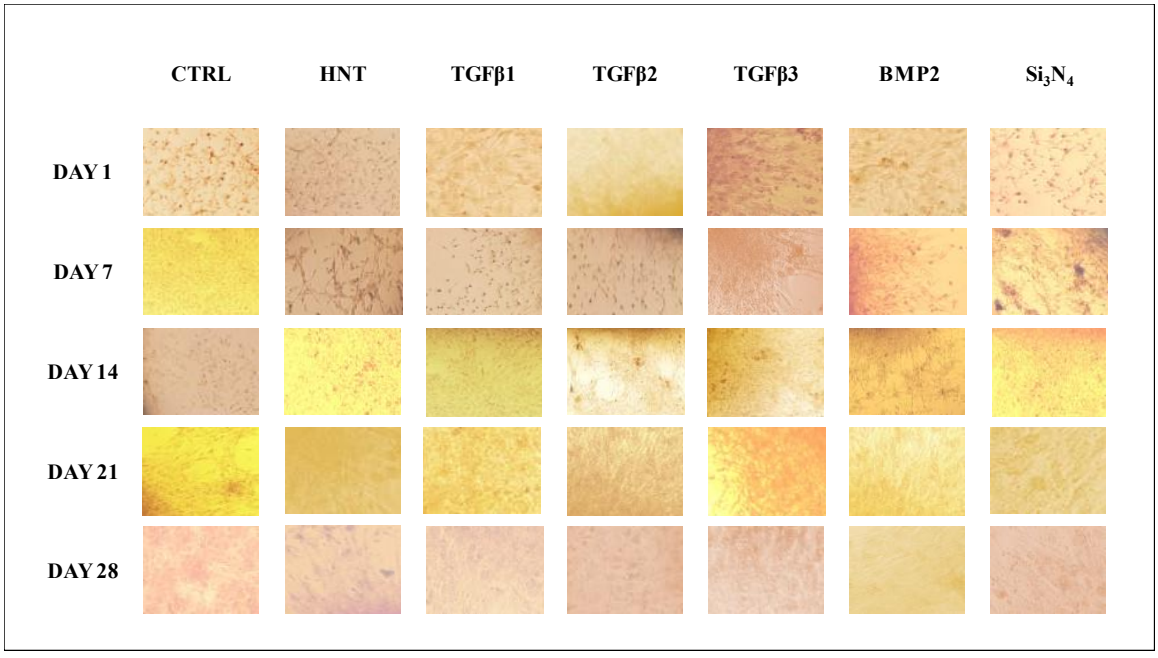


**Figure 4-12:** Alizarin Red S staining of each well after days 1, 7, 14, 21, and 28 days of exposure to nanocomposite.

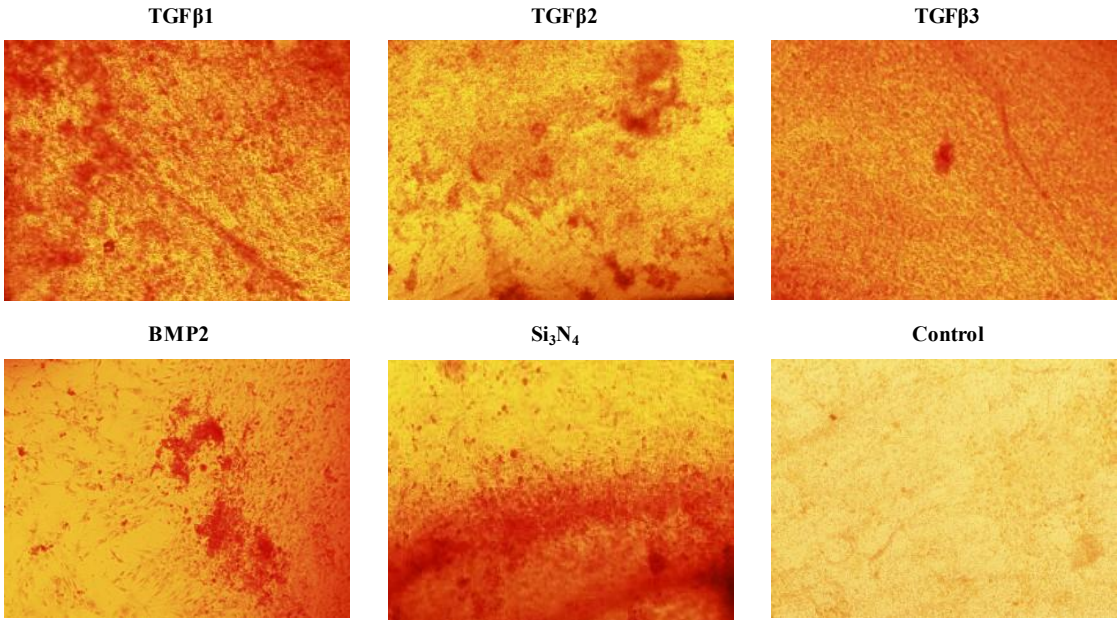


**Figure 4-13:** Alizarin Red S staining of each well after 35 days of exposure to nanocomposite.

## 4.4 Discussion and Conclusions

### 4.4.1. FITC/BSA Release

In this experiment, human mesenchymal stem cells were exposed to PLA nanocomposite containing HNTs doped with various growth factors. Preliminary results on the 3D printed nanocomposites doped with FITC/BSA showed consistent results for the 6 samples that were tested for each period of degradation. Analysis of the release of the FITC/BSA contained within the printed nanocomposite revealed a release pattern that showed an initial slow release and increased as the polymer began to undergo hydrolysis. To calculate the FITC/BSA released into the PBS, the slope of the line in the calibration curve was used and the number was doubled to account for the sample size of 2 mL. **Figure 4-3** shows the total amount of FITC/BSA released into solution. Growth factor

release should follow the same pattern of release due to the similar size and external charges of BSA and the growth factor proteins.

### 4.4.2 Live/Dead

Live dead staining was performed on all samples to reveal the nanocomposite's cytotoxic effects on the stem cells. The results revealed that not only were the nanocomposites non-cytotoxic, but they were also a desirable location for cell growth. Clustering and cell migration at or near the edge of the nanocomposite made this conclusion evident. It is believed that the release of growth factor facilitated the agglomeration of cells near the nanocomposite. There was no major decline in the ratio of live to dead cells over the entirety of the 28-day cytotoxicity study. The results were expected since none of the additives nor the polymers were found to be cytotoxic in tests performed on the individual components. *In vitro* cytotoxicity testing using mesenchymal stem cells give confidence that future test using animal models for *in vivo* testing would exhibit similar noncytotoxic effects.

### 4.4.3 Alizarin Red S Staining

The Alizarin Red S staining was performed in on the cells of all wells including the control cells. Although the nanocomposites were predegraded with sodium hydroxide to add texture, no further preconditioning was done. A small quantity of growth factor was released into solution over the first 4 weeks of the test, thus there was not much differentiation in the stem cells. Additionally, research has shown that differentiation into the lineage of osteocytes typically shows calcium deposits only after 28 days. The minute quantity of growth factor that was released aided in cell recruitment, which was evident due to the proximity of the cell clusters to the nanocomposite. The differentiation study

was planned to be concluded after day 28, however, an additional plate remained and was allowed to proliferate and differentiate for an additional 7 days to see post-28-day calcium deposits. Contamination was present in all 3 undoped HNT/PLA nanocomposite wells for the day 35 reading, so images of those sample were unattainable. The wells that contained TGFβ1, TGFβ2, TGFβ3, BMP2, and silicon nitride all had cells that had elevated levels of calcium deposits, indicating that cells were differentiating into osteocytes or chondrocytes.

Our hypothesis was supported with the evidence provided by the live/dead and Alizarin Red S staining assays. Our nanocomposites released growth factor or silicon nitride over time and were seen to be non-cytotoxic to mesenchymal stem cells while promoting osteogenic differentiation. The release of the morphogenic agent contained within the polymer nanocomposites have been proven to foster cell proliferation, migration, and differentiation due to direct exposure.

### 4.5 Future Studies

Additional testing will be done on nanocomposites of the same material that have undergone more significant hydrolysis. A higher degree of degradation has multiple effects on cell morphology and structure. Cells may be able to integrate into a nanocomposite and grow in 3 dimensions. Additionally, a steady supply of growth factor will be available to continue the signaling cascade that would lead to osteogenic differentiation. The present study tested the ability of each growth factor to facilitate cell migration and differentiation individually. Future research will combine growth factors to harness each growth factor’s ability to impact cell development synergistically.

Additional western blot testing will be used to specifically confirm the presence of ALP++, osterix ++, or osteopontin which are proteins that are produced by immature osteoblasts. Epiphycan (Epyc) and unique cartilage matrix-associated protein (Ucma) are proteins that can confirm the presence of immature chondrocytes will also be tested.

# CHAPTER 5

# ANTIBACTERIAL 3D FILAMENT AND MASK FILTER

## 5.1 Introduction

The spread of bacteria and viruses can be facilitated through touch or airborne contact. Infectious diseases or complications with preexisting ailments may result from exposure to these pathogens. Infectious diseases are a leading cause of mortality worldwide, with viruses making a significant global impact on healthcare and socio-economic development. Currently, COVID-19 is a worldwide health pandemic that affects the world similarly to the 1918 influenza pandemic that claimed an estimated 50,000,000 lives. The recent onslaught of the COVID-19 epidemic, caused by a novel coronavirus, has affected every facet of human life in some way. Densely populated buildings such as prisons, assisted living homes, and hospitals reported thousands of cases [67]. The COVID-19 pandemic has caused severe disruptions to human communities in employment, medical supplies, household supplies, food and food services, mental health, and many more. Life will be different for the foreseeable future in these uncertain times.

The human mouth and nose act as a susceptible environment for viral entry and incubator for multiple viruses [68]. The nasal epithelium is one of the first sites of

infection for the SARS-CoV-2 virus [69]. Investigations into the expression of the cell surface enzyme angiotensin-converting enzyme 2 (ACE2) have been conducted, showing binding to a SARS-CoV-2 spike protein [69]. The combination of ACE2 and the spike proteins promote the virus's internalization into human cells [69]. The presence of virus binding receptor ACE2 expressed by the mouth and throat epithelial cells makes the virus binding challenging to prevent [70], [71]. The spike protein on the surface of coronaviruses multifunctional molecular machine mediates coronavirus entry into host cells [72]. It first binds to a receptor on the host cell surface through its S1 subunit and then fuses viral and host membranes through its S2 subunit. Two domains in S1 from different coronaviruses recognize various of host receptors, leading to the viral attachment [72]. Recent research has shown evolutionary advantages of the virus in binding to the host surface, longer-lasting, and increased active receptor sites in humans [73], [74].

The transmission of COVID-19 is thought to occur through respiratory droplets. Current CDC guidelines recommend using N95 masks for health care providers managing the care of patients infected with SARS-CoV-2 or persons under investigation (PUI) for COVID-19 [75], [76]. Recent studies have revealed that the aerosolization of SARS-CoV-2 is detectable in the air, and the virus remains viable for up to 3 hours [67]. The global shortage of PPE in the setting of a viral pandemic has created potentially dangerous conditions for frontline healthcare workers lacking appropriate protection and their patients [77]. In the spring of 2020, there existed a shortage of N95 masks, surgical masks, and face shields at hospitals for medical responders testing and treating COVID-

19 patients. Medical responders need to be protected from respiratory droplets from coughing and sneezing in a stressful and intense hospital setting [78].

COVID-19 particles range from 60-140 nm, while N95 masks filter particles at 300 nm and only 95 percent of test particles. N99 respirators filter particles at 100 nm, and without inactivating pathogen particles. Any smaller particles that are filtered by the N95 or N99 mask is done so by electrostatic forces. Additionally, the respiratory droplets that are thought to carry the viral particles are larger than the size of the viral particles themselves and may also be caught by current masks. However, individuals with chronic respiratory, cardiac, or other medical conditions may have difficulties wearing N95 masks for extended periods due to labored breathing. Due to the high similarities of previous novel coronaviruses, it is believed that immunocompromised individuals, elderly, and patients suffering from chronic or acute respiratory illness remain highly susceptible to the onset of symptoms and higher mortality rates among the general public [79], [80]. The virus's virulent nature remains a threat to all of society as all age groups have been impacted in some capacity. Moreover, N95 respirators are not designed for children or individuals with facial hair. Because of these inherent gaps in capability, a new mask must be developed for increased protection against viral pathogens while also taking other considerations into hand such as comfortability and mask related health risks and prevention.

The need for advanced protective masks continues to mount each day for healthcare professionals worldwide, with no signs of stopping, even with the control of the current COVID-19 pandemic. Because the future timing of outbreaks is unknown, developing a mask that protects a wider scope of wearers in a clinical or domestic setting

remains a high priority. All healthcare personnel, ordinary citizens, and our servicemen and their families should not have to resort to homemade apparatus that are potentially leaving them at risk to inhale pathogens and are not entirely effective at preventing the spread of viral particles [81]. Even though many individuals and groups are designing and manufacturing face shield frames for these responders using personal 3D printing machines, many designs are not implemented for high-density optimized additive manufacturing and cannot be accessed locally [81], [82].

N95 respirators are personal protective equipment that is used to protect the wearer from airborne particles and liquid. An N95 respirator is a respiratory protective device designed to achieve a very close facial fit and very efficient airborne particles' filtration. Some N95 respirators are intended for use in a health care setting and worn by health care personnel during procedures to protect both the patient and health care personnel from the transfer of microorganisms, body fluids, and particulate material as well as filtering specific amounts of viruses or bacteria, reducing the amount of but not actively killing viruses, bacteria, or fungi [83]–[86]. A recent publication noted co-infection with other respiratory pathogens was as high as 21% [87]. Surgical masks are designed to prevent others from becoming infected due to airborne particles and liquids expelled from the wearer. There is a common misconception that surgical masks provide adequate wearer protection from the inhalation of harmful microorganisms. Surgical masks are used to protect a patients' wounds from aerosol or mucosal droplets that may contain harmful microorganisms and offer little respiratory protection for the user [88].

The respiratory system is not the sole means of infection by COVID-19 or other bacteria and viruses. Surfaces can harbor various pathogens transmitted to the body by

transferring to the skin from a surface and into the body through any orifice or lesion. Research has shown that the attachment of bacteria to horizontal surfaces may stimulate bacterial growth [89]. This is due to the increased nutrient deposits as organic material tends to settle on its surface [89]. Additionally, metabolites and co-factors may be obtained from these surfaces and can lead to biofilms, which protect the bacteria. Biofilms provide resistance to mechanical damage, dislodgement due to liquid or airflow, and antibiotic treatment resistance [89], [90]. Care must be taken to prevent bacteria from producing exopolysaccharide matrix or glycocalyx which are critical components of biofilms. A substance that can kill or disable pathogens in a short period is crucial to fighting bacterial, fungal, and viral infections.

The interaction of metal nanoparticles (mNPs) with microorganisms offer many advantages for therapeutic applications. The unique physical properties of mNPs have associated benefits for drug delivery [91]. These are predominantly due to the particle size (which affects bioavailability and circulation time), large surface area to volume ratio (enhanced solubility compared to larger particles), the particle's tunable surface charge with the possibility of encapsulation, and excessive drug payloads that can be accommodated [92], [93]. Metals such as silver and copper exert toxicity at inherently low concentrations that are non-toxic to mammalian cells [94]. It is believed that copper kills bacteria by releasing copper cations and reactive oxygen species that disrupt cellular activity [95]. The ability to cross bacteria cell membrane and damage vital enzymes are the properties that make copper nanoparticles an effective antibacterial material. Research has shown that silver nanoparticles damage the bacteria's outer membrane by inducing pits and gaps that fragment the cell [96]. Zinc nanoparticles' antibacterial

mechanism is not fully understood, but they have been shown to cause morphological changes, membrane leakage and an increase in oxidative stress gene expression [96].

When mNPs particle size is reduced, this amplifies the toxicity even at low levels and increases their prokaryotes' effects [93]. Combinations of silver, copper, and zinc nanoparticles exhibit synergistic antimicrobial activity, which can be attributed to increased prokaryotic cell permeability [94]. Furthermore, when mNPs are combined with antibiotics and doped into polymers, they have shown a similar augmented antimicrobial effect [94], [97].

In response to the COVID-19 pandemic, we designed an antimicrobial filter and mask tandem filtration unit made of medical-grade bioplastics and metal/ceramic nanoparticle composites. The filter utilized in our design aimed to possess a porosity of 50nm due to the nature of the electrospun fibers that form a "spider-web-like" material that is breathable and long-lasting. The filter material is similar to the mask's material except for the quantity of mHNTs and manufacturing method. Our first application of this filter system was as a replacement to N95 respirators. Critical in our design concept was to fabricate a fluid resistant filter unit that provides the wearer protection against large droplets, splashes, or sprays of bodily or other hazardous fluids. It also protects the patient from the wearer's respiratory emissions and reduces the wearer's exposure to particles, including small particle aerosols and large droplets.

## 5.2 Materials and Methods

### 5.2.1 Fabrication Design

The filtration units were fabricated in a variety of sizes with rigid or elastic thermoplastics. Polylactic acid (PLA) and thermal plastic urethane (TPU) were the polymers of choice to manufacture the filtration unit's mask portion. PLA was the only thermoplastic used for the filter systems. Filters are composed of a commercially available gauze, thermoplastic, and mHNTs. We have a patented method for metalizing the HNT surface with antimicrobial metals (copper, silver, zinc, and others). 3D printing will assemble the masks in a layer-by-layer fashion. It affords a significant ability for customization with different metal-coated HNTs (mHNTs), antimicrobial-loaded HNTs, and antimicrobial-loaded mHNTs. The filters also carry an electrostatic charge to attract small enough particles enough to pass through the filter's pores.

### 5.2.2 Inner and Outer Fabric Layers of the Filter

Many N95 masks utilize a triple-ply approach to manufacture their respirators. These three-ply materials are typically made of an outer layer of bonded fabric, a filtration layer comprised of melt-blown material, and an inner layer made of more bonded fabric. A similar approach was taken for the manufacturing of the filters for this experiment. The filter for the mask was also comprised of three layers. The first and last layers were composed of rayon/polyester wound gauze pads (Equate, Bentonville, Ar.). The inner layer was comprised of blow-spun PLA/mHNT. A multilayered approach to manufacturing the filters offers an improved ability to filter particles in both airflow directions during inhalation and exhalation. Furthermore, the inner layer can be made

double thick to add more filtering capability by coating both gauze pieces with blow-spun material.

### 5.2.3 Material Preparation and Filament Extrusion

#### 5.2.3.1 *Metal HNT Preparation*

A non-sacrificial standard two-electrode electrolysis setup was assembled consisting of two platinum-coated titanium mesh electrodes acting as a reversible cathode and anode. The electrodes were gently cleaned using silicon carbide abrasive papers and ultrasonicated in distilled water for 10 minutes to remove any surface contamination. The electrodes were held parallel at a 2-inch distance and connected to a DC power source (VWR Accupower 500 electrophoresis power supply).

An ultrasonicated colloidal solution of 700 mL of 5mM ($AgNO_3$, $CuSO_4$ or $ZnSO_4$ respectively) and 350 mg HNT were dispersed in the electrolysis vessel (1000 mL VWR borosilicate glass beaker) and continuously stirred using a magnetic stir bar to reduce electrophoretic buildup and precipitate formation at the working electrode. A temperature of 85°C during the duration of the electrolysis process. The 20V charge was applied in 5-minute intervals, after which the polarity was reversed. This process continued for a total of six 5-minute cycles for a total of 30 minutes.

The supernatant was decanted and washed with deionized water three times. The solution was centrifuged at 2000 rpm for 5min with water to separate mHNTs from the unreacted NPs. The supernatant was removed. The unreacted NPs collect on top of the dense pellet after centrifugation and were removed. The mHNTs were then dried at 37°C. A schematic of the set up can be seen in **Figure 5-1**.

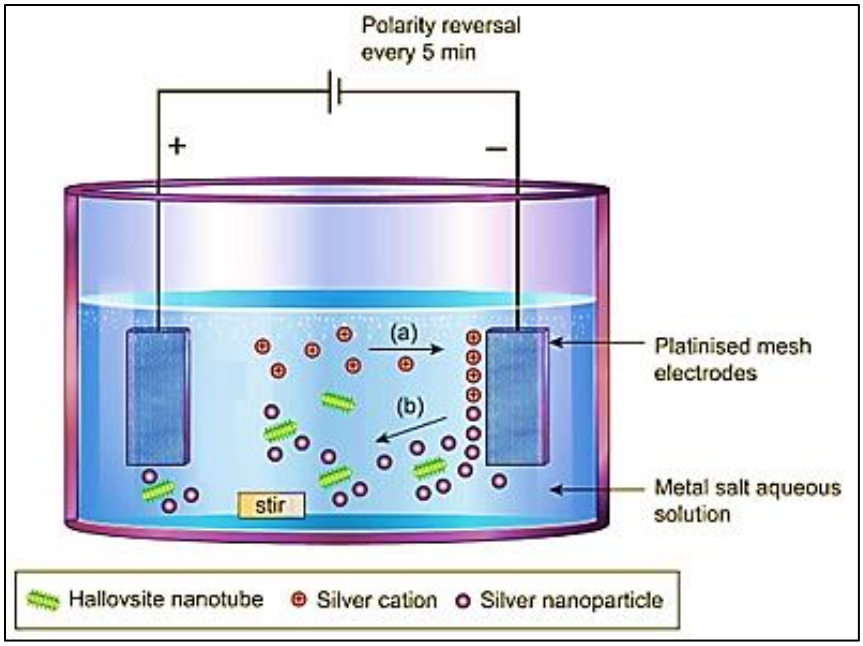


**Figure 5-1:** Schematic of the halloysite metal coating process.

5.2.3.2 *HNT and mHNT PLA Filament Preparation*

Five compositions were tested in this study: PLA, PLA+mHNTs/Zn, PLA+mHNTs/Cu, PLA+mHNTs/Ag, and PLA+mHNTs/(Ag,Cu,Zn). Filaments were extruded using a Noztek Pro Extruder (West Sussex, England) with a uniform diameter of 1.75 ±0.05mm, but there was a slightly different filament preparation for each group. For the PLA group, PLA filaments were extruded at 175°C. For PLA+mHNTs groups, to archive a uniform distribution of HNTs in PLA, 20µL of PEG 200 was added into 20g PLA and vortexed for 10 minutes, then 1g of Zn, Cu, or Ag mHNTs were added and continually vortexed for another 10 minutes. For PLA+mHNTs/(Ag,Cu,Zn) mixture, 0.33g of each respective mHNT type were combined before adding them to the PEG coated PLA. All mixtures of PLA+mHNTs were extruded at 181°C. Prior to extrusion, all compositions were allowed to pre-dry for 4hrs in an incubator at 60°C as per the manufacturer's instructions to yield a more uniformed extrusion.

### 5.2.4 3D Printing of Masks

3D printing of the masks was done on an Ender 3 (Shenzhen, China) 3D printer with most of the general settings. The mask's design was produced using the free computer-aided design (CAD) website TinkerCAD.com and converted to a stereolithography (.stl) file. Ultimaker Cura 4.5 was used to adjust design parameters and create the g-code. Each mask was printed 205°C with an infill ratio of 50 % and the print platform heated to 50°C to aid in bed adhesion.

### 5.2.5 3D printing of Testing Discs

Each filament was printed into test discs for bacterial studies using a Creality ENDER 3 Pro (Shenzhen, China) 3D printer with similar settings. Due to the addition of the mHNTs, a slightly higher temperature was needed to print the testing discs successfully. PLA filament was printed at 205°C, while the PLA/mHNT filament was printed at 210°C. The test discs were cylindrical, with a height of 2mm and a diameter of 6mm for an overall surface area of 94.25mm$^2$. The infill ratio of the discs was 100% to make a solid disc with minimal porosity.

### 5.2.6 Antibacterial Testing

Bacterial cultures were prepared to test the pre-extruded and 3D printed filament's ability to inhibit bacterial growth. Antibacterial testing was done on both GS doped mHNTs and undoped mHNTs. The pre-extruded non-doped and doped mHNTs were subjected to Mueller-Hinton broth testing. Muller-Hinton agar plates and Muller-Hinton broth test tubes were used to provide testing mediums for the antibacterial capabilities of the printed non-doped and doped mHNTs. Gentamicin reference discs were plated to give a reference for the zone of inhibition on the agar plates.

#### 5.2.6.1 *Muller-Hinton Broth*

Liquid medium testing was facilitated using Mueller-Hinton broth. 5 mL of Muller-Hinton broth was added to each glass test tube and autoclaved. Once the broth cooled overnight, samples were marked for each polymer sample. We used *E. coli* and *S. aureus* as a model gram-negative and gram-positive bacterial source. Testing was performed on mHNT coated PLA beads, gentamicin doped mHNTs coated PLA beads, 3D printed non-doped mHNT PLA discs. Finally, 3D printed gentamicin doped mHNTs PLA discs. Glass culture tubes were inoculated with 50 µL of *E. coli* or *S. aureus* after each respective mHNT or doped mHNT bead or disc was added to the broth of each tube. Controls of uninoculated Muller-Hinton broth and inoculated broth were used. The cultures and controls were incubated at 37°C for 48 hrs. Optical density for the non-doped mHNT coated PLA beads readings were taken for at the 0 and 48 hr marks. Readings were taken for the GS doped mHNTs beads and discs at the 0, 24, and 48 hr mark. Each test was done in triplicate and the results were averaged.

#### 5.2.6.2 *Muller-Hinton Agar*

Muller-Hinton agar plates were prepared for manufacturers' specifications. We used *E. coli* and *S. aureus* as gram-negative and gram-positive bacterial sources. Testing was performed on 3D printed gentamicin doped mHNTs PLA discs. Each respective filament blend was printed into the small cylindrical disc described above. Each polymer was plated added to the bacteria covered agar plates before a 24 hr incubation at 37°C. zone of inhibition measurements was taken using a digital caliper. Each test was done in triplicate and the zone of inhibition diameters were averaged.

### 5.2.7 Blow Spinning Fibers

A mixture of 10 mL dichloromethane (DCM), PLA, and mHNTs were combined and ultrasonicated for 20min. The solution was then left for 48 hr at room temperature. A Zeny gravity feed airbrush kit was used with the air pump set to maintain a constant pressure of 40-60psi as our blow spinner. A square (4in x 4in) of sterile gauze as attached to the spraying platform. 4 mL of the DCM/PLA/mHNT solution was evenly airbrushed onto the surface of the gauze. The gauze was fully dry overnight at room temperature. Two squares were placed together with the airbrushed sides facing each other to make a four-layer filter. An unsprayed gauze square was used to sandwich the blow-spun layer of another gauze square to make a three-layer filter.

#### 5.2.7.1 *Blow-Spun Fiber Concentrations*

Three different mixtures of DCM, PLA, and mHNT were used to compare the surface's appearance to determine which was more uniformed. Each mixture contained 10 mL of DCM and varying amounts of PLA and mHNT. The concentrations of PLA in DCM were 0.1 g/mL, 0.075 g/mL, and 0.05 g/mL. Each mixture contained twenty percent mHNT by weight concerning the amount of PLA. Using 4 mL of the solution, theoretically 400 mg, 300 mg, and 200 mg of PLA with 80 mg, 60 mg, and 40 mg of mHNT was deposited onto each square of gauze respectively.

#### 5.2.7.2 *Blow-Spun Fibers with Varying Amounts of mHNTs*

Filters with varying amounts of mHNTs were made to test the dispersion of copper across the surface of the filters. 10 mL of DCM was added to three 50 mL glass vials along with 500 mg of PLA. 50 mg, 100 mg, and 150 mg of CuHNTs were added to each respective glass vial to make a 10%, 20%, and 30% mHNT to PLA solution. 3 mL of

each solution was blow-spun onto a 4x4 inch gauze square and allowed to dry at room temperature for 24 hours before analysis.

### 5.2.8 Distribution of mHNTs in the Filter

The blow-spun fibers using PLA, dichloromethane and mHNTs were blown onto gauze, an analysis of the distribution of mHNTs was performed. SEM and EDS imaging were used to examine the fibers and map the distribution of the mHNTs on the surface of the blow-spun material.

### 5.2.9 Filter Imaging

#### 5.2.9.1 *Scanning Electron Microscope (SEM)*

The mHNTs and filters were imaged with the SEM to characterize the texture of the surface. The filters' surface topography will give an insight into how the blow-spun fibers are oriented and show prominent pores near the surface. SEM images will confirm that the HNTs are coated with metal nanoparticles.

#### 5.2.9.2 *Energy Dispersion Spectroscopy (EDS)*

The mHNTs and filters were imaged and analyzed with the EDS to further characterize the texture of the surface and show the dispersion of metal on their body. The distribution of metal on the surface of the filters can be displayed and quantified to represent the entirety of the filter. The EDS will confirm and quantify that the mHNTs are coated in metal nanoparticles.

## 5.3 Results

### 5.3.1 SEM of mHNTs

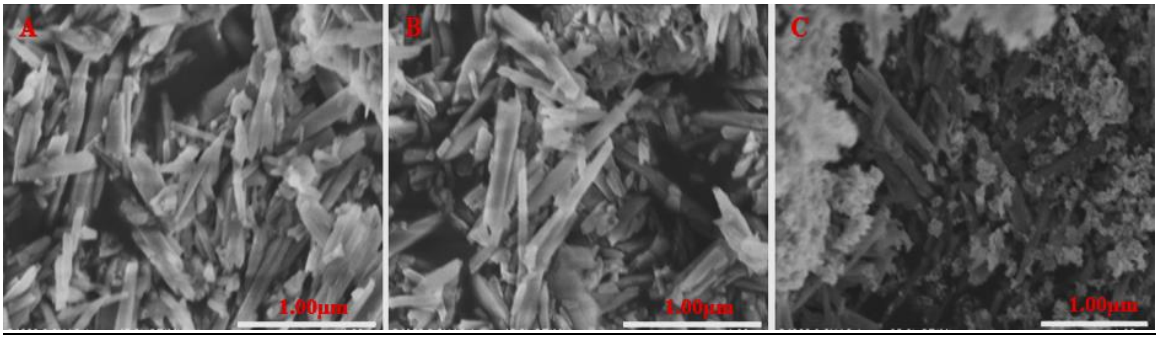


**Figure 5-2:** Scanning electron microscope image of A) silver, B) copper, and C) zinc coated halloysite nanotubes.

The SEM images shown in **Figures 5-2 A-C** show a thin, uniformed coating of metal on the outside surface of the HNTs. Excess agglomerated zinc particles were seen in the image. These particles were unable to be washed away using additional washing. The following EDS images confirm the presence of each metal on the surface of the halloysite.

5.3.2 EDS of mHNTs

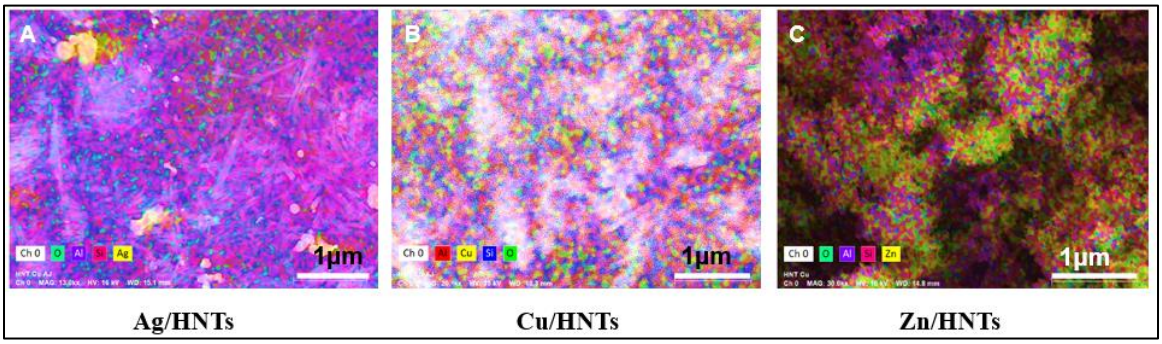


**Figure 5-3:** Energy dispersion X-ray spectroscopy scan of A) silver, B) copper, and C) zinc coated halloysite nanotubes.

EDS analysis of the highlighted boxes **Figure 5-5 A-C** revealed a quantitative weight of ~6% for silver nanoparticles, ~5% for copper nanoparticles, and ~8% for zinc nanoparticles. Due to the unpredictable nature of the metal coating process, a variance in the amount of coating per nanotube is not unpredictable. Large clusters of copper and zinc nanoparticles were not observed as seen previously in silver samples.

5.3.3 Liquid Growth Inhibition Studies

The absorbance values for each Mueller-Hinton broth culture were measured at 630 nm. The results for the 48h mHNT coated PLA beads are shown in **Figure 5-4**. The optical densities for the 24h and 48h bacteria cultures in Mueller-Hinton broth that contained GS doped mHNT coated PLA beads are shown in **Figure 5-5** and **Figure 5-6**. **Figure 5-7** and **Figure 5-8** show *E. coli* and *S. aureus*'s growth pattern when exposed to PLA beads coated in GS doped mHNTs. Optical density is directly correlated to the turbidity of the broth. Higher turbidity is evidence of a higher amount of bacterial growth. As such, the control broth for each set of cultures yielded the highest optical densities. This is observed for *E. coli* and *S. aureus* cultures at the 24h and 48h readings.

The optical densities for the 24h and 48h bacteria cultures in Mueller-Hinton broth that contained GS doped mHNT 3D printed discs are shown in **Figure 5-9** and **Figure 5-10**. **Figure 5-11** and **Figure 5-12** show the growth pattern of *E. coli* and *S. aureus* when exposed to GS doped mHNTs discs. A higher turbidity was also observed in both cultures when using GS doped mHNT discs.

In the experiments done with GS doped mHNT covered PLA beads and 3D printed GS doped mHNT embedded PLA discs, the cultures were also done with HNT covered PLA beads and 3D printed PLA embedded with HNT to see the effects of plain HNTs on bacterial growth. The resulting studies showed little to no growth inhibition of either *E. coli* or *S. aureus*. The GS doped mHNT coated beads showed little to no bacterial growth after an incubation period of 24h and 48h. The results of the bacterial studies done with 3D printed GS doped mHNT embedded PLA discs showed a higher optical density than the GS doped mHNTs covered PLA beads in *E. coli* and *S. aureus*.

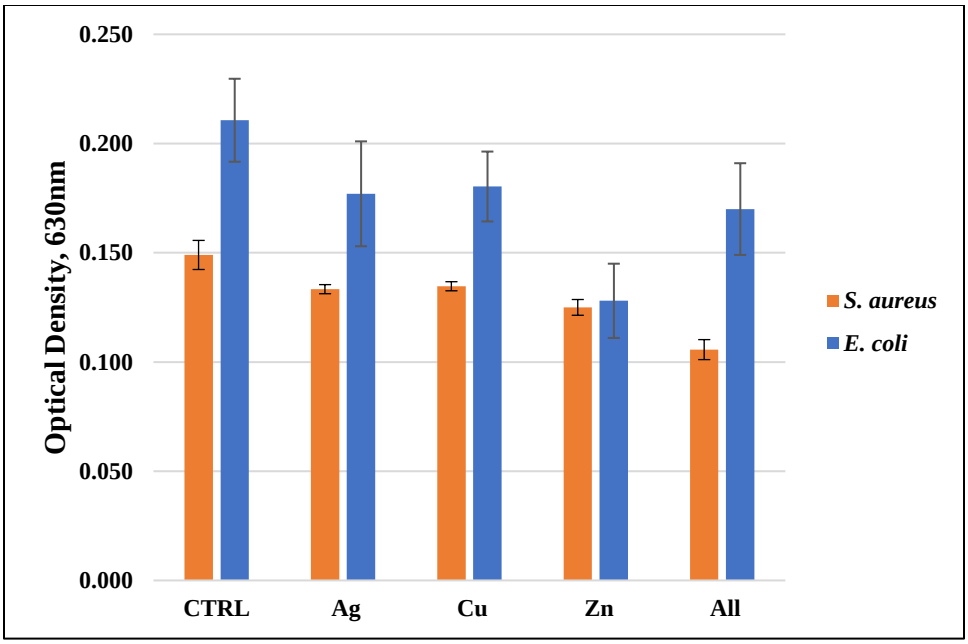


**Figure 5-4:** PLA beads coated with mHNTs in Mueller-Hinton broth for 48h with *E. coli* or *S. aureus*. Optical density was taken at 630nm wavelength. Error bars represent ± standard deviation. Values had a significant difference unless denoted ($p<0.05$). (n=3)

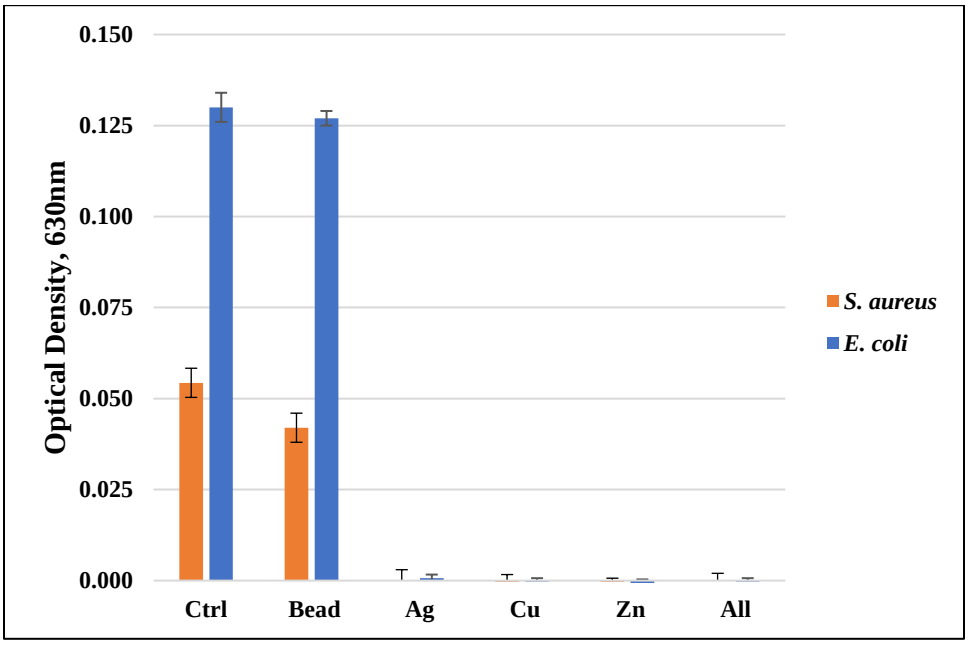


**Figure 5-5:** PLA beads coated with doped mHNTs in Mueller-Hinton broth for 24h with *E. coli* or *S. aureus*. Optical density was taken at 630nm wavelength. Error bars represent ± standard deviation. Values had a significant difference unless denoted ($p<0.05$). (n=3)

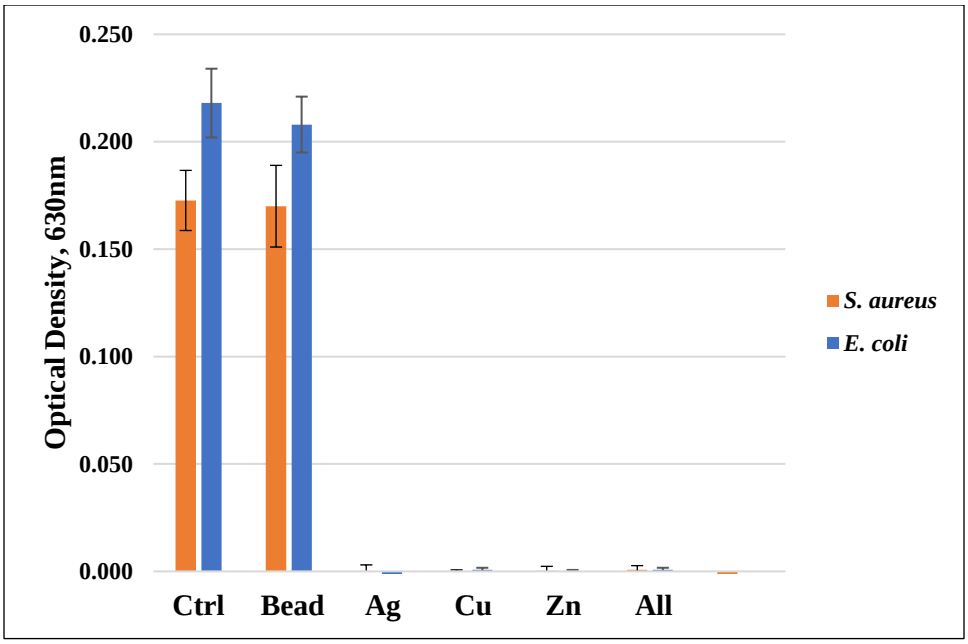


**Figure 5-6:** PLA beads coated with doped mHNTs in Mueller-Hinton broth for 48h with *E. coli* or *S. aureus*. Optical density was taken at 630nm wavelength. Error bars represent ± standard deviation. Values had a significant difference unless denoted ($p<0.05$). (n=3)

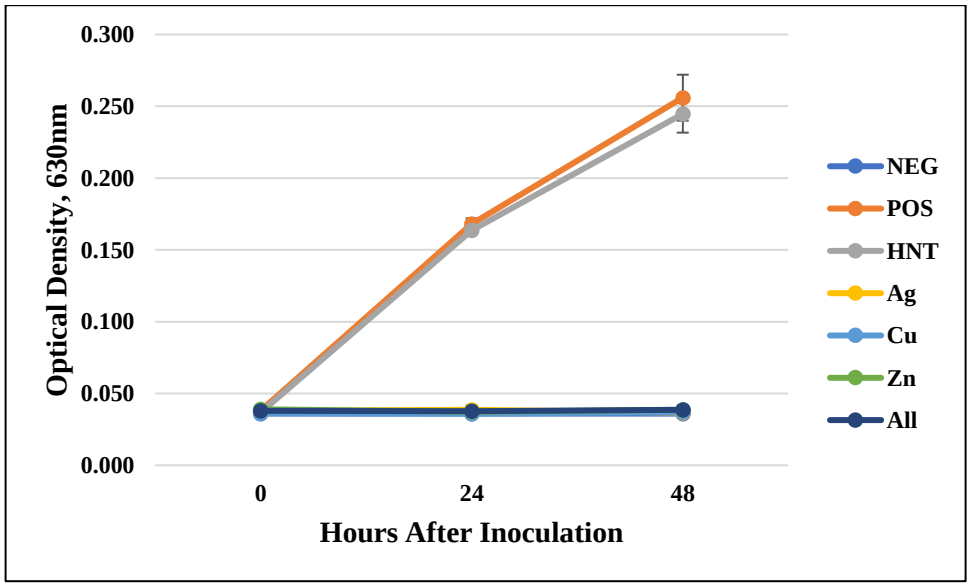


**Figure 5-7:** PLA beads coated with GS doped mHNTs in Mueller-Hinton broth for 48h with *E. coli*. Optical density readings were taken at 0, 24, and 48h. Optical density was taken at 630nm wavelength. Error bars represent ± standard deviation. (n=3)

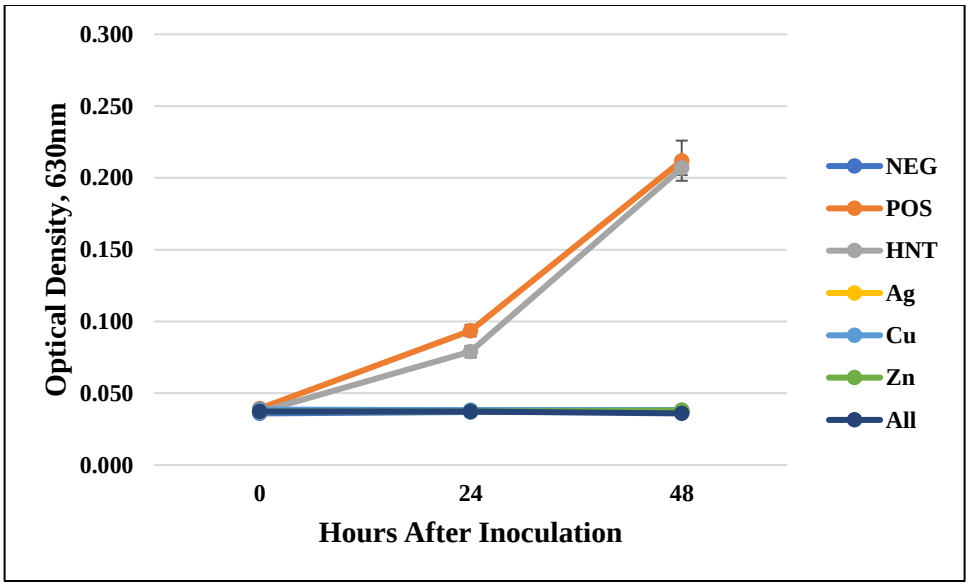


**Figure 5-8:** PLA beads coated with GS doped mHNTs in Mueller-Hinton broth for 48h with *S. aureus*. Optical density readings were taken at 0, 24, and 48h. Optical density was taken at 630nm wavelength. Error bars represent ± standard deviation. (n=3)

The 3D printed PLA discs were subjected to identical testing conditions as the mHNT and GS doped mHNT coated beads. The results can be seen in **Figures 5-9** through **5-12.**

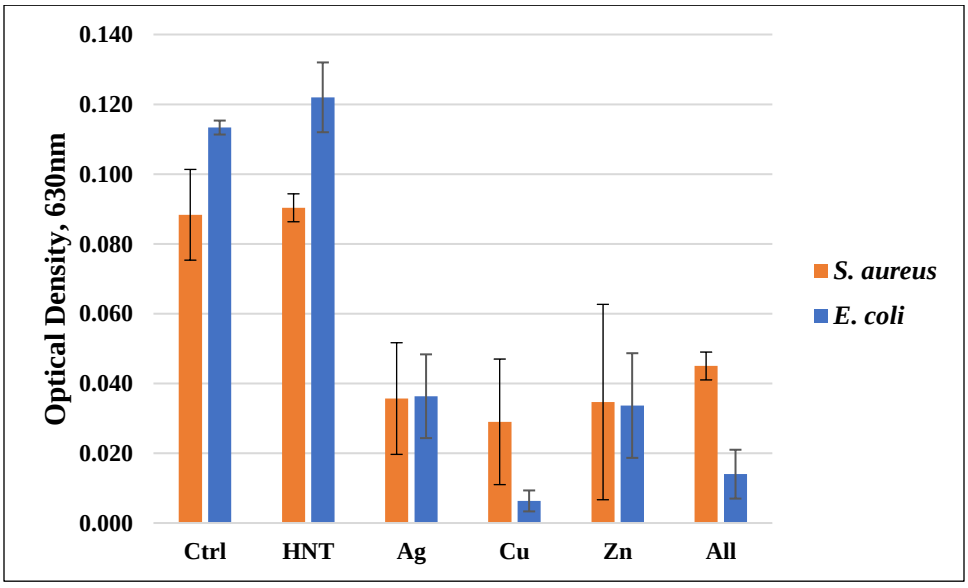


**Figure 5-9:** GS doped 3D printed mHNTs discs in Mueller-Hinton broth for 24h with *E. coli* or *S. aureus*. Optical density was taken at 630nm wavelength. Error bars represent ± standard deviation. Values had a significant difference unless denoted ($p<0.05$). (n=3)

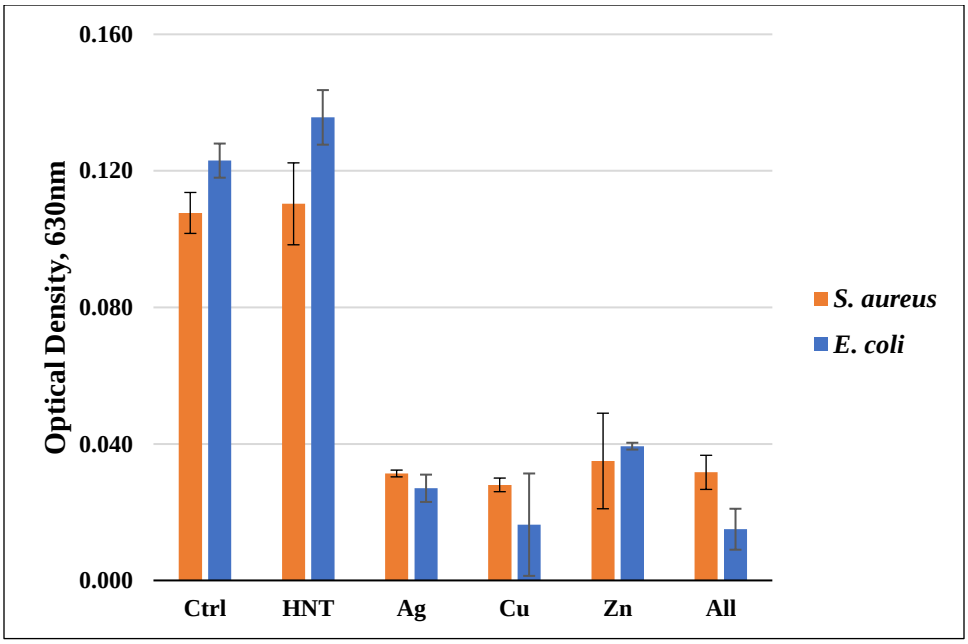


**Figure 5-10:** GS doped 3D printed mHNTs discs in Mueller-Hinton broth for 48h with *E. coli* or *S. aureus*. Optical density was taken at 630nm wavelength. Error bars represent ± standard deviation. Values had a significant difference unless denoted ($p<0.05$). (n=3)

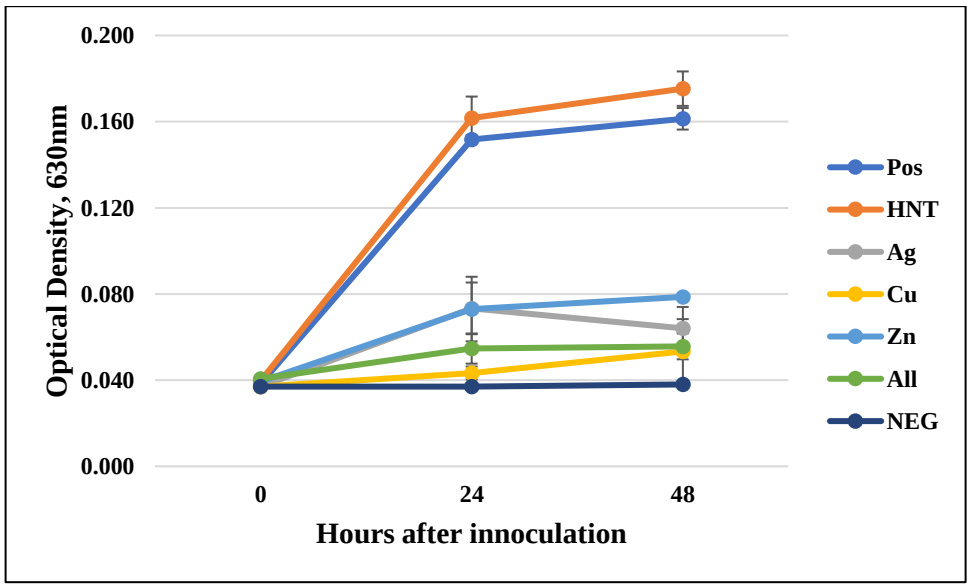


**Figure 5-11:** 3D printed PLA with GS doped mHNTs in Mueller-Hinton broth for 48h with *E. coli*. Optical density readings were taken at 0, 24, and 48h post inoculation. Optical density was taken at 630nm wavelength. Error bars represent ± standard deviation. (n=3)

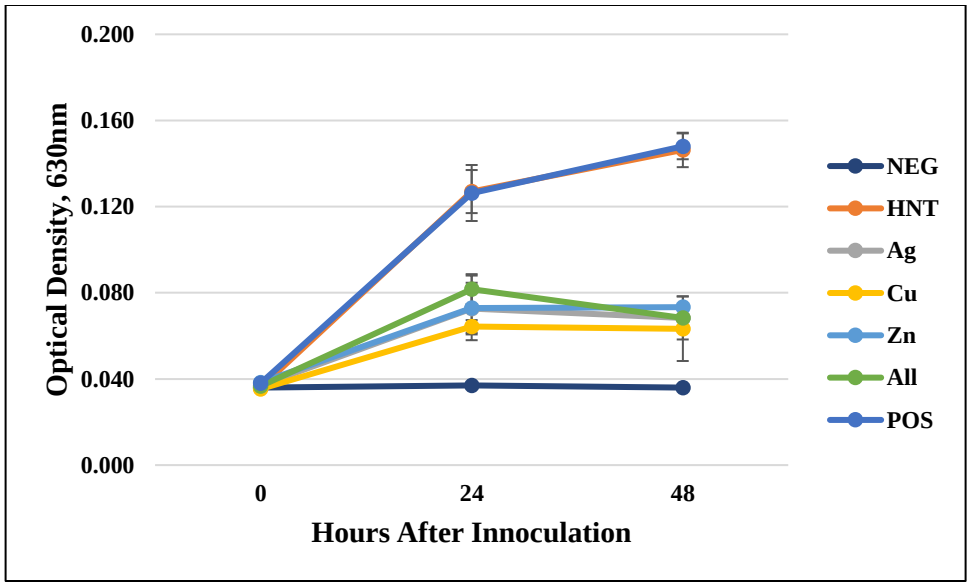


**Figure 5-12:** 3D printed PLA with GS doped mHNTs in Mueller-Hinton broth for 48h with *S. aureus*. Optical density readings were taken at 0, 24, and 48h post inoculation. Optical density was taken at 630nm wavelength. Error bars represent ± standard deviation. (n=3)

### 5.3.4 Plate Growth Inhibition Studies

The zone of inhibition for undoped mHNTs in PLA discs is displayed in **Figure 5-13**. The pictures from **Figure 5-14** and **5-15** display the zone of inhibition of the different formulations of 3D printed GS loaded mHNT PLA discs. A positive control lawn of bacteria was used for both *E. coli* and *S. aureus* to display the ability to grow on the Mueller-Hinton agar plates. Each control plate had full coverage across the entire surface. A PLA disc embedded with plain HNTs was also plated to show any antibacterial properties of plain HNTs. **Figure-16** shows the average zone of inhibition for each respective 3D printed GS loaded PLA disc.

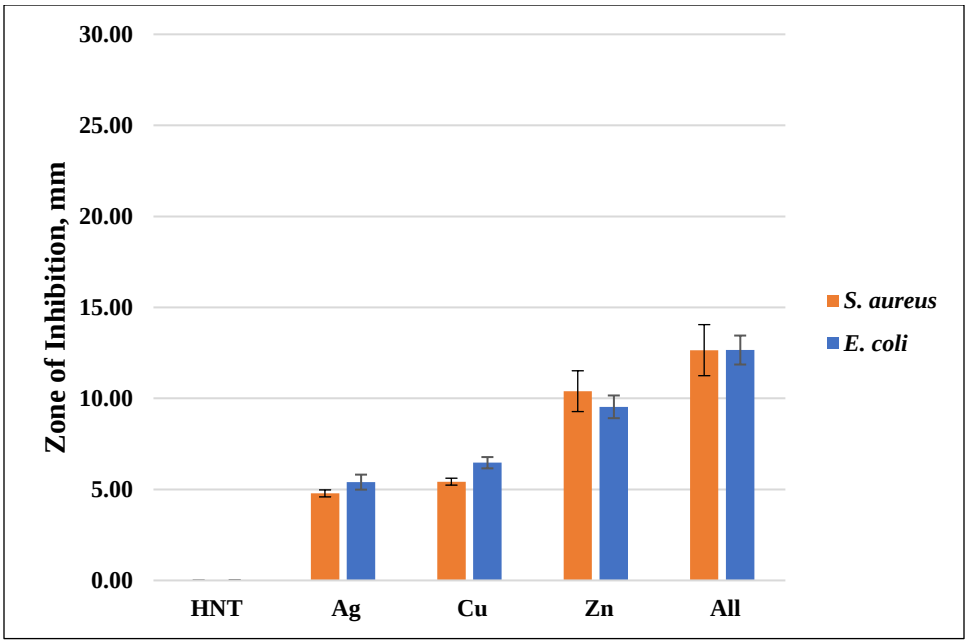


**Figure 5-13:** Zone of inhibition diameter average for each respective 3D printed discs after 24h. Error bars represent ± standard deviation. Values had a significant difference unless denoted ($p<0.05$). (n=3)

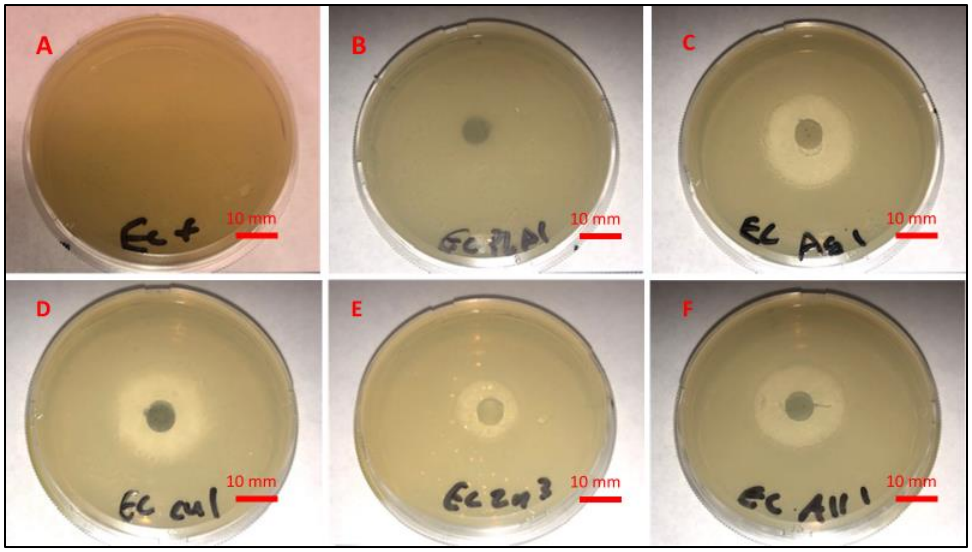


**Figure 5-14:** Mueller-Hinton agar plates, plated with *E. coli*, and (A) nothing, (B) PLA/HNT, (C) 3D printed GS/Ag/HNT disc, (D) 3D printed GS/Cu/HNT disc, (E) 3D printed GS/Zn/HNT disc, (F) 3D printed GS/Ag,Cu,Zn/HNT disc.

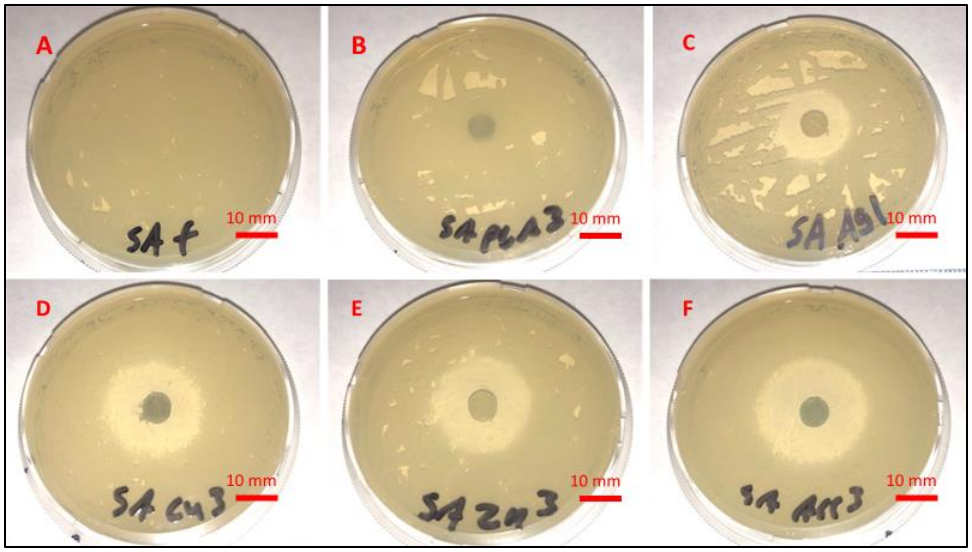


**Figure 5-15:** Mueller-Hinton agar plates, plated with *S. aureus*, and (A) nothing, (B) PLA/HNT, (C) 3D printed GS/Ag/HNT disc, (D) 3D printed GS/Cu/HNT disc, (E) 3D printed GS/Zn/HNT disc, (F) 3D printed GS/Ag,Cu,Zn/HNT disc.

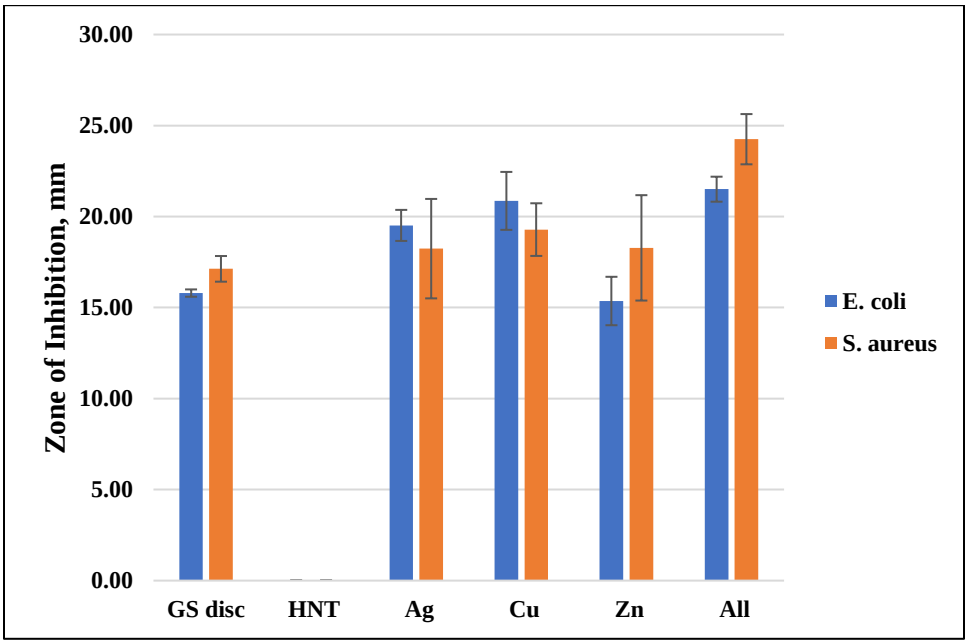


**Figure 5-16:** Zone of inhibition diameter average for each respective 3D printed discs after 24h. These were GS loaded mHNTs. Error bars represent ± standard deviation. Values had a significant difference unless denoted ($p<0.05$). (n=3)

### 5.3.5 Filter SEM and EDS

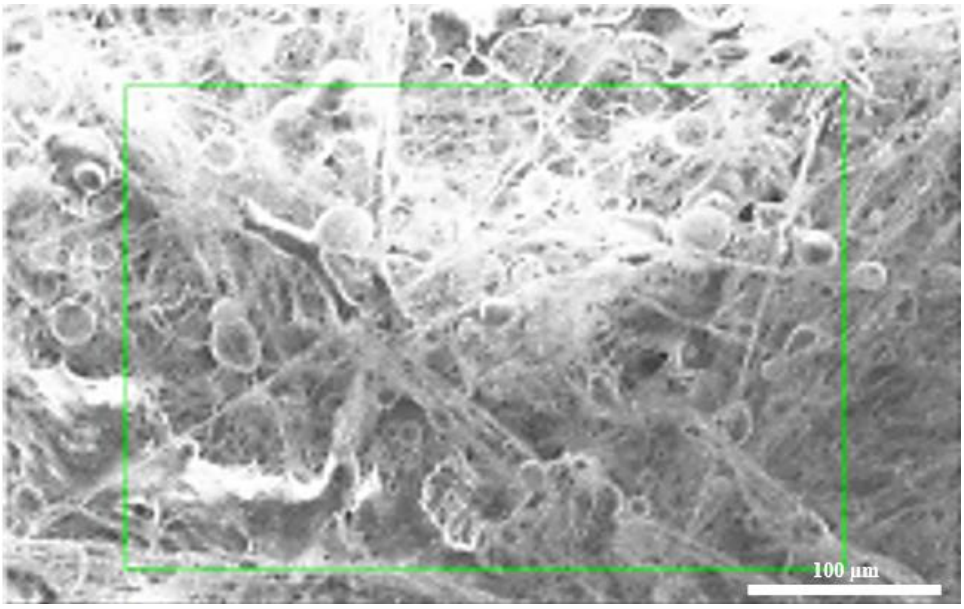


**Figure 5-17:** SEM of filter using the 0.1g/mL mixture PLA solution.

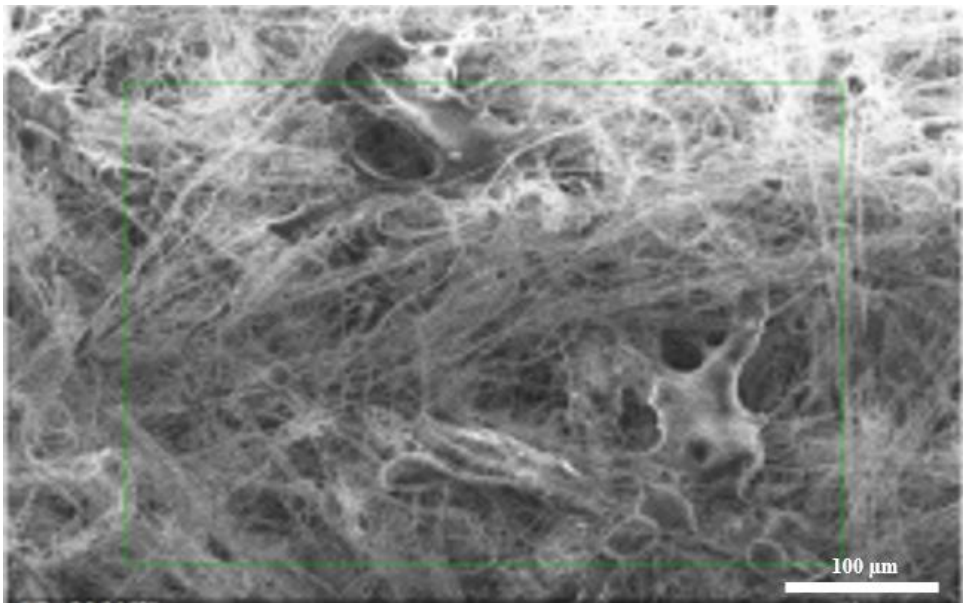


**Figure 5-18:** SEM of filter using the 0.075g/mL mixture PLA solution.

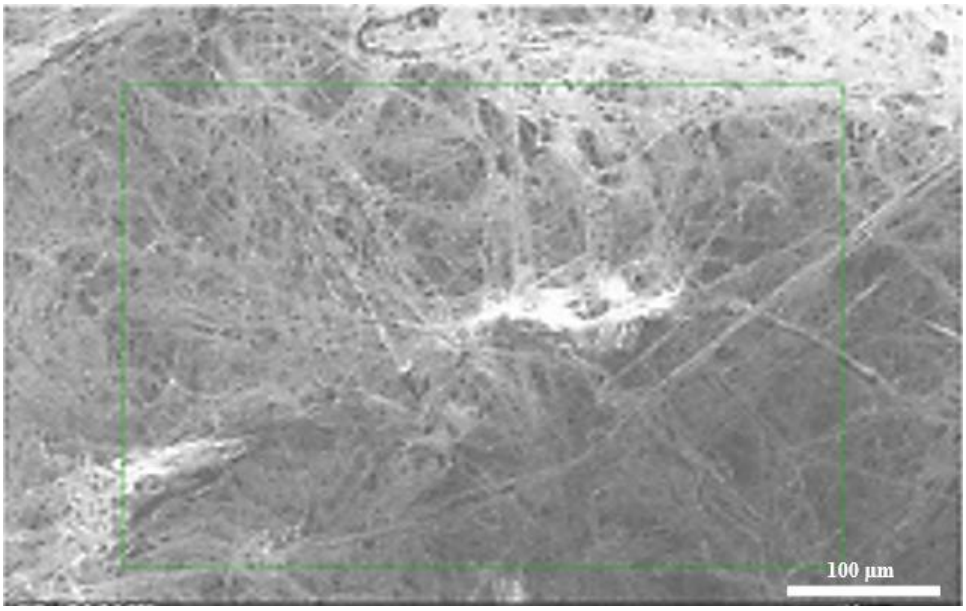


**Figure 5-19:** SEM of filter using the 0.05g/mL mixture PLA solution.

Fast scan SEM imaging was used to obtain the above images. Slower scanning or higher amounts of scans would have deformed the filter due to thermal energy imposed upon by the electron emitted from the SEM.

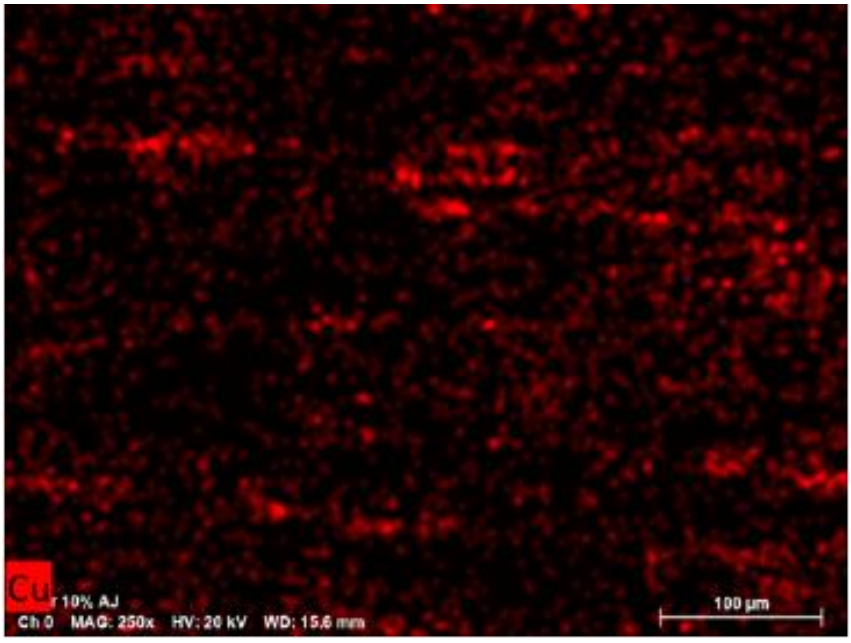


**Figure 5-20:** EDS of 10% CuHNT to PLA blow-spun fibers.

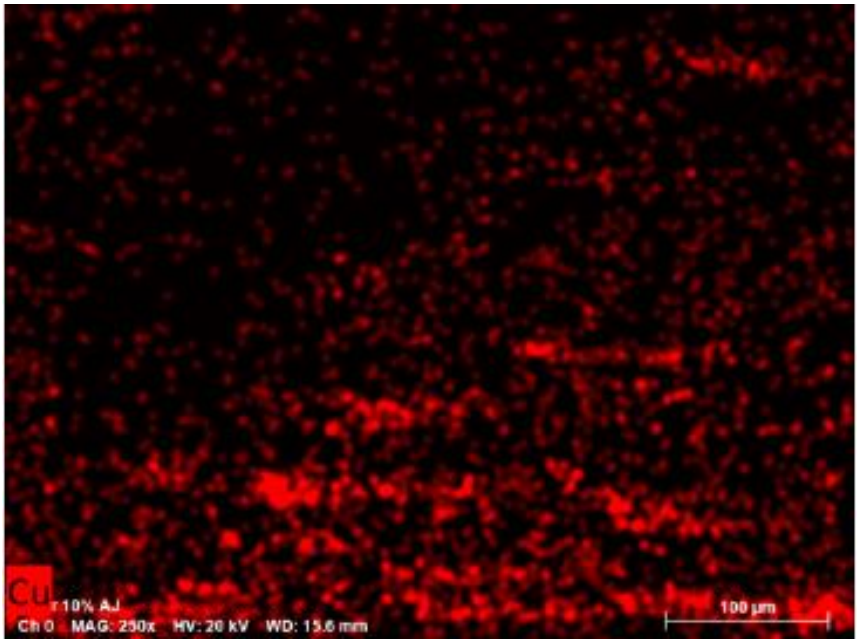


**Figure 5-21:** EDS of 20% CuHNT to PLA blow-spun fibers.

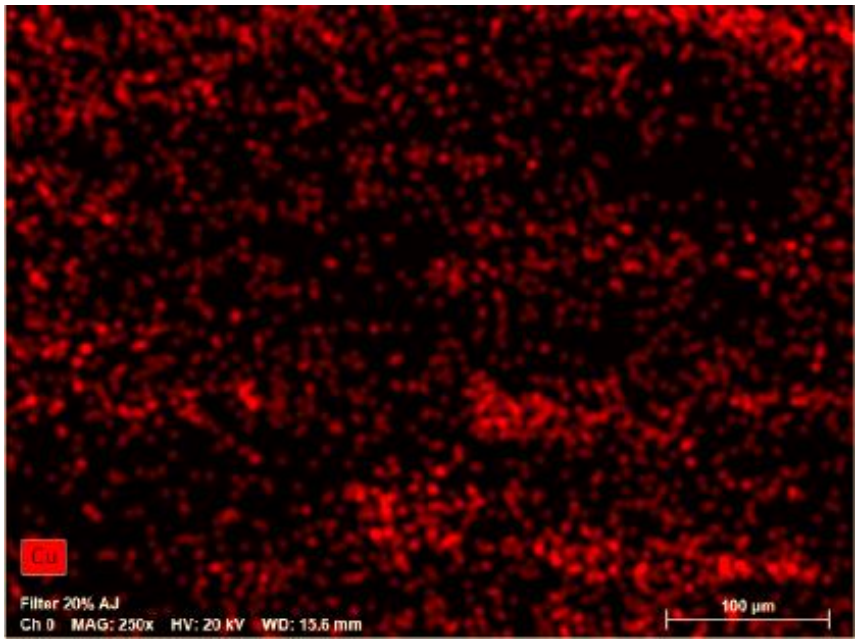


**Figure 5-22:** EDS of 30% CuHNT to PLA blow-spun fibers.

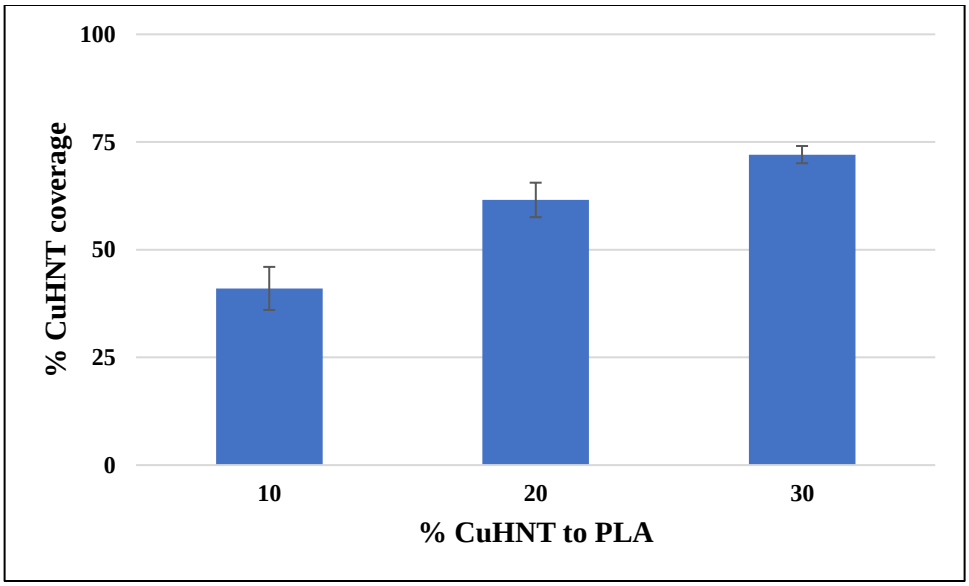


**Figure 5-23:** Graph showing the coverage of representative piece of each filter. Error bars represent standard deviation. Values had a significant difference unless denoted ($p<0.05$). (n=3)

## 5.4 Discussions

### 5.4.1 Analysis of GS/mHNTs

The EDS scans confirmed the addition of each metal to the surface of the halloysite nanotube. The color rendered images illustrated that each metal was deposited evenly on all nanotubes and was on the surface even after vacuum loading with gentamicin. Minimal contamination of unbound nanoparticles was observed. The presence of high concentrations of each specific metal nanoparticle in the area exhibiting high concentrations of the halloysite's outer surface's silicone confirmed this result. In samples with high amounts of contamination, large pockets of agglomerated nanoparticles with little to no silicone present.

### 5.4.2 Antibacterial Studies

The antibacterial capabilities of mHNTs and GS doped mHNTs were tested in a series of experiments using both gram-positive and gram-negative bacteria. All iterations

of mHNT show a hindrance to bacterial growth. Vacuum loading mHNTs with GS offered a more remarkable ability to inhibit bacterial growth. As seen in **Figures 2** and **3**, the non-3D printed GS loaded mHNT coated PLA beads could better inhibit bacterial growth than the 3D printed GS loaded mHNT discs. We speculate that since the entire load of GS loaded mHNTs was on the surface of the beads, more of the nanoparticles and gentamicin were available to deter bacterial growth. The 3D printed discs were made with extruded filament containing the GS loaded mHNTs. The GS loaded mHNTs were dispersed within the filament and thus mainly within the 3D printed discs. With the nature of the dispersion, some GS loaded mHNTs were present on the 3D printed disc's surface to inhibit bacterial growth. We observed that the GS loaded mHNTs could inhibit bacterial growth more than the gentamicin control disc. It is believed that the synergy of the loaded gentamicin and the metal nanoparticles made this possible.

While the coated beads performed better than the 3D printed discs, they will lose their ability to be an effective bacterial deterrent over time. The nature of the 3D printed discs is such that they wear down over time. This wearing effectively discards the now empty mHNTs and exposed new ones to the surface thus keeping its antimicrobial properties. The principle of a renewed antimicrobial outer surface has benefits for manufacturing products like masks, light switches, and toilet handles. The advent of utilizing this technology to manufacture objects with questionable sanitation could lower the ability to transmit microorganisms.

Medical facilities, such as hospitals or clinics, could see the most benefit from using antimicrobial surfaces to help fight the spread of infections like MRSA. Surfaces are periodically sanitized in medical facilities; however, there are gaps when these

surfaces are not cleaned. Surfaces such as doorknobs, water fountains, and water faucet handles are often touched with little second thought to the possible transfer of germs. An innate ability to self-sanitize would provide considerably better protection to all who come into contact.

To produce the quantity needed for mass implementation, two manufacturing methods can be used, industrial 3D printers or injection molding. Each technique of mass manufacturing has its advantages and disadvantages. The benefits of industrial 3D printing are the rapid ability to change the design of the object being printed. The obstacles that are faced with industrial 3D printing are the slow turnover and increased porosity. Injection molding has a faster throughput but can typically be harder to adjust the design.

The GS doped mHNTs and their antimicrobial capabilities can be used to manufacture more than the face masks and filters tested in this study. Intubation tubes and catheters can be manufactured with mHNTs to reduce infections in patients caused by bacterial. Eye guards have been made using mHNTs embedded in polycarbonate or poly (methyl methacrylate). Clarity was not compromised by implementing the mHNTs and showed an improvement in strength and antimicrobial capability. Research continues to be conducted to discover more products that can benefit from the implementation of mHNTs.

### 5.4.3 Filter Construction

The SEM images show that the fibers of the filter are long and interwoven strands. The blow-spun fibers' complex structure reduces the filter's porosity, allowing it to capture or block microscopic particles. Visual analysis each fiber construct's three

different concentrations revealed that a higher concentration of PLA in solution would yield a blotchy, uneven spray pattern instead of fine, uniformed fibers.

The EDS images show that we have an even distribution of mHNTs on the surface of the filter. The concentration of mHNT on the surface went up as predicted with higher concentrations of mHNT in solution, with minimal adverse effects such as area agglomeration. We concluded that the blow-spun fibers at the surface represent the internal fibers of the filter. With each pass of the airbrush, an additional layer is added of seemingly the same fiber dispersion.

The EDS images in **Figure 5-20**, **5-21**, and **5-22** showed an even distribution of CuHNTs filter's surface. The blow-spun fibers beyond the surface should exhibit similar patterns of distribution. The varying concentration of CuHNTs influenced the number of deposited mHNTs. Darkfield analysis of the EDS images showed a decline in the overall darkness as the concentration of CuHNT increased, meaning more copper was present. Analysis of the overall intensity of the EDS images of multiple filters revealed that the coverage of mHNT when using 20% and 30% were similar. The precent of coverage can be seen in **Figure 5-23**. These combined results mean the 30% CuHNT was applied more evenly across the surface. This could be due to having a more homogeneous starting mixture or merely human error when blow spinning.

## 5.5 Conclusions

3D printing has emerged as a viable option to manufacture face masks. The critical design feature in N95 respirators and surgical masks is the filtration unit. We have an efficient and effective design using 3D printing that can be scaled up for mass production via injection molding or industrial-scale 3D printers. We have demonstrated

the capability of our antimicrobial filament to be used to manufacture a mask that has antibacterial capabilities. GS loaded mHNTs were successfully used to effectively kill or retard the growth of both gram-negative and gram-positive bacteria on a surface and in liquid mediums. Mueller-Hinton broth optical density and Mueller-Hinton agar plate zone of inhibition results support this conclusion. While the mHNTs showed an ability to hinder bacteria's growth, the GS-doped mHNTs offered a much greater capacity to kill or inhibit bacterial growth. Due to the nature of the filament manufacturing and the 3D processes, careful consideration was taken when choosing the antimicrobial agent used as a dopant.

Recent concerns about the effectiveness of 3D printed face masks and respirators have arisen in response to similar designs to our "Montana style mask" made on commercially available printers. The two major concerns are that the mask's fit is not adequate, and the filter is not secured tight enough. We modified the original design of the Montana mask to address these issues. We added a layer of soft material to the masks' edge to improve comfort and provide a better seal to the wearer's face. The soft fabric was made of silicon weather stripping that was glued into place. A rubber foam material was not used due to porosity and complications with future sanitation. The silicon can be sanitized with UV light, soap, alcohol, or hydrogen peroxide solutions. The filter seal was improved by the addition of a small lip onto the front of the mask. The lip would act as a guard in which you could tightly push the filter and filter guard against the front of the mask, making a better seal.

Future studies will explore alternative doping materials to customize filament to have enhanced capabilities such as antifungal, antiviral, antibacterial, anticorrosive, and

many more within the PLA filament. The addition of different metal nanoparticles and multiple types of metal nanoparticles to a single HNT could improve the PLA filament's antibacterial capabilities. Polyethylene terephthalate glycol (PETG) will be explored as an alternative option to PLA because it is more robust and durable.

The respirator will soon undergo National Institute of Occupational Safety and Health (NIOSH) certified fit testing to ensure it passes government regulations for occupational use within the United States of America. Antiviral studies will be conducted using two surrogate coronaviruses, mouse hepatitis virus (MHV) and transmissible gastroenteritis virus (TGEV). Testing will include viral elimination on the filter's surface that will be analyzed using an ELISA kit. Additionally, the filter will be tested using a nebulized virus in a vacuum system to gauge the effectiveness of stopping viral particles from penetrating through the filter's blow-spun layers.

# BIBLIOGRAPHY


[1] N. S. S. 00286, A. J. Tonino, C. L. Davidson, P. J. Klopper, and L. A. Linclau, "Protection from stress in bone and its effects," *J. bone Jt. Surg.*, pp. 107–113, 1976.

[2] G. Leventhal, "TITANIUM, A METAL FOR SURGERY," *J. bone Jt. Surg.*, vol. 33-a, no. 2, pp. 473–475, 1951.

[3] A. Dhawan, N. Ghodadra, V. Karas, M. J. Salata, and B. J. Cole, "Complications of Bioabsorbable Suture Anchors in the Shoulder," *Am. J. Sports Med.*, vol. 40, no. 6, pp. 1424–1430, Jun. 2012.

[4] T. A. Turvey, B. Bell, C. Phillips, and W. R. Proffit, "Self-Reinforced Biodegradable Screw Fixation Compared With Titanium Screw Fixation in Mandibular Advancement NIH Public Access," *J Oral Maxillofac Surg*, vol. 64, no. 1, pp. 40–46, 2006.

[5] K. W. Frisken, G. W. Dandie, S. Lugowski, and G. Jordan, "A study of titanium release into body organs following the insertion of single threaded screw implants into the mandibles of sheep," *Austrailian Dental Journal*, vol 47, no. 3, pp. 214 -217 2002.

[6] G. Logroscino, F. Donati, M. Saracco, L. Pilloni, and C. Piconi, "Early failure of a locked titanium plate in a proximal humeral fracture: Case report and metallurgic analysis," *Trauma Case Reports*, vol. 17, pp. 18–22, Oct. 2018.

[7] R. Burgers, T. Gerlach, S. Hahnel, F. Schwarz, G. Handel, and M. Gosau, "In vivo and in vitro biofilm formation on two different titanium implant surfaces," *Clin. Oral Implants Res.*, vol. 21, no. 2, pp. 156–164, Feb. 2010.

[8] M. M. Fürst, G. E. Salvi, N. P. Lang, and G. R. Persson, "Bacterial colonization immediately after installation on oral titanium implants," *Clin. Oral Implants Res.*, vol. 18, no. 4, pp. 501–508, Aug. 2007.

[9] D. W. Hutmacher, "Scaffold design and fabrication technologies for engineering tissues — state of the art and future perspectives," *J. Biomater. Sci. Polym. Ed.*, vol. 12, no. 1, pp. 107–124, Jan. 2001.

[10] C. V. Bourantas, Y. Zhang, V. Farooq, H. M. Garcia-Garcia, Y. Onuma, and P. W. Serruys, "Bioresorbable Scaffolds: Current Evidence and Ongoing Clinical Trials," *Curr. Cardiol. Rep.*, vol. 14, no. 5, pp. 626–634, Oct. 2012.

[11] S.-J. Park *et al.*, "Sirolimus-Eluting Stent Implantation for Unprotected Left Main Coronary Artery Stenosis Comparison With Bare Metal Stent Implantation," *J. Am. Coll. Cardiol.*, vol. 45, no. 3, 2005.

[12] C. Gaball, S. Lovald, B. Baack, and G. Olson, "Minimally invasive bioabsorbable bone plates for rigid internal fixation of mandible fractures.," *Arch. facial Plast. Surg. Off. Publ. Am. Acad. Facial Plast. Reconstr. Surgery, Inc. Int. Fed. Facial Plast. Surg. Soc.*, vol. 13, no. 4, pp. 31–35, 2015.

[13] M. Suchenski *et al.*, "Material Properties and Composition of Soft-Tissue Fixation," *Arthrosc. J. Arthrosc. Relat. Surg.*, vol. 26, no. 6, pp. 821–831, Jun. 2010.

[14] D. W. Hutmacher, "Scaffolds in tissue engineering bone and cartilage," *Biomaterials*, vol. 21, no. 24, pp. 2529–2543, Dec. 2000.

[15] L. M. Tielinen, "Bioabsorbable Polymer and Bone Growth Factor Composites," *Topics in Tissue Engineering, University of Oulu,* vol. 7, pp. 1–11, 2003.

[16] K. E. Uhrich, S. M. Cannizzaro, R. S. Langer, and K. M. Shakesheff, "Polymeric Systems for Controlled Drug Release," *Chem. Rev.*, vol. 99, no. 11, pp. 3181–3198, Nov. 1999.

[17] L. Tielinen *et al.*, "Combining transforming growth factor-beta(1) to a bioabsorbable self-reinforced polylactide pin for osteotomy healing: an experimental study on rats.," *J. Orthop. Sci.*, vol. 4, no. 6, pp. 421–430, 1999.

[18] Y. M. Lvov, E. Abdullayev, and Y. Lvov, "Halloysite clay nanotubes for controlled release of protective agents," *Artic. J. Nanosci. Nanotechnol.*, vol. 11, pp. 10007–10026, 2011.

[19] M. Wu, G. Chen, and Y.-P. Li, "TGF-β and BMP signaling in osteoblast, skeletal development, and bone formation, homeostasis and disease," *Bone Res.*, vol. 4, 2016.

[20] F. A. Millan, F. Denhez, P. Kondaiah, and R. J. Akhurst, "Embryonic gene expression patterns of TGF beta 1, beta 2 and beta 3 suggest different developmental functions in vivo," *Development*, vol. 111, no. 1, pp. 131-143 1991.

[21] P. Schmid, D. Cox, G. Bilbe, R. Maier, and G. K. Mcmaster, “Differential expression of TGF beta 1, beta 2 and beta 3 genes during mouse embryogenesis,” *Development,* vol. 111, no. 1, pp. 117-130 1991.

[22] L. A. Opperman, K. Adab, and P. T. Gakunga, “Transforming growth factor-β2 and TGF-β3 regulate fetal rat cranial suture morphogenesis by regulating rates of cell proliferation and apoptosis,” *Dev. Dyn.*, vol. 219, no. 2, pp. 237–247, Oct. 2000.

[23] A. W. James, Y. Xu, J. K. Lee, R. Wang, and M. T. Longaker, “Differential effects of TGF-beta1 and TGF-beta3 on chondrogenesis in posterofrontal cranial suture-derived mesenchymal cells in vitro.,” *Plast. Reconstr. Surg.*, vol. 123, no. 1, pp. 31–43, Jan. 2009.

[24] A. Matsiko, T. J. Levingstone, J. P. Gleeson, and F. O’brien, “Incorporation of TGF-beta 3 within collagen-hyaluronic acid scaffolds improves their chondrogenic potential,” *Advanced healthcare materials,* vol. 4, no. 8, pp. 1175-1179, Jun. 2015.

[25] M. Kim, I. E. Erickson, M. Choudhury, N. Pleshko, and R. L. Mauck, “Transient exposure to TGF-β3 improves the functional chondrogenesis of MSC-laden hyaluronic acid hydrogels.,” *J. Mech. Behav. Biomed. Mater.*, vol. 11, pp. 92–101, Jul. 2012.

[26] T. Matsubara *et al.*, “BMP2 Regulates Osterix through Msx2 and Runx2 during Osteoblast Differentiation,” *Journal of Biological Chemistry,* vol. 283, no. 43, pp. 29119-29125, Oct. 2008.

[27] E. Balint *et al.*, “Phenotype discovery by gene expression profiling: Mapping of biological processes linked to BMP-2-mediated osteoblast differentiation,” *J. Cell. Biochem.*, vol. 89, no. 2, pp. 401–426, May 2003.

[28] T. Katagiri *et al.*, “Bone Morphogenetic Protein-2 Converts the Differentiation Pathway of C2C12 Myoblasts into the Osteoblast Lineage.” *The Journal of Cell Biology*, vol. 127, no. 6, pp. 1755-1766, Dec. 1994

[29] C. C. Guedes e Silva, B. König, M. J. Carbonari, M. Yoshimoto, S. Allegrini, and J. C. Bressiani, “Bone growth around silicon nitride implants-An evaluation by scanning electron microscopy,” *Mater. Charact.*, vol. 59, no. 9, pp. 1339–1341, 2008.

[30] J. Olofsson, T. M. Grehk, T. Berlind, C. Persson, S. Jacobson, and H. Engqvist, “Evaluation of silicon nitride as a wear resistant and resorbable alternative for total hip joint replacement.,” *Biomatter*, vol. 2, no. 2, pp. 94–102, 2012.

[31] B. Sonny and M. Raham, “The Rationale for Silicon Nitride Bearings in Orthopaedic Applications,” *Adv. Ceram. - Electr. Magn. Ceram. Bioceram. Ceram. Environ.*, 2012.

[32] R. Kue, A. Sohrabi, D. Nagle, C. Frondoza, and D. Hungerford, “Enhanced proliferation and osteocalcin production by human osteoblast-like MG63 cells on silicon nitride ceramic discs,” *Biomaterials*, vol. 20, no. 13, pp. 1195–1201, 1999.

[33] G. Pezzotti *et al.*, “Human osteoblasts grow transitional Si/N apatite in quickly osteointegrated Si3N4 cervical insert,” *Acta Biomater.*, vol. 64, pp. 411–420, 2017.

[34] B. Cappi, S. Neuss, J. Salber, R. Telle, R. Knü, and H. Fischer, “Cytocompatibility of high strength non-oxide ceramics,” *Journal of Biomedical Materials Research Part A: An Official Journal of The Society for Biomaterials, The Japanese Society for Biomaterials, and The Australian Society for Biomaterials and the Korean Society for Biomaterials*, vol. 93, no. 1, pp. 67-76 2010.

[35] A. Neumann *et al.*, “Osteosynthese im GesichtsschädelbereichOsteosynthesis in facial bones,” *HNO*, vol. 54, no. 12, pp. 937–942, 2006.

[36] T. J. Webster, A. A. Patel, M. N. Rahaman, and B. Sonny Bal, “Anti-infective and osteointegration properties of silicon nitride, poly(ether ether ketone), and titanium implants,” *Acta Biomater.*, vol. 8, no. 12, pp. 4447–4454, Dec. 2012.

[37] X. Yin, “Rescuing failed oral implants via Wnt activation," *Journal of Clinical Periodontology*, vol. 43, no. 2, pp. 180-192, 2016.

[38] I. K. Karoussis, U. Brägger, G. E. Salvi, W. Bürgin, and N. P. Lang, “Effect of implant design on survival and success rates of titanium oral implants: A 10-year prospective cohort study of the ITI® Dental Implant System,” *Clin. Oral Implants Res.*, vol. 15, no. 1, pp. 8–17, Feb. 2004.

[39] T. Wang, R. Patel, and B. Derby, “Manufacture of 3-dimensional objects by reactive inkjet printing,” *Soft Matter*, vol. 4, no. 12, pp. 2513-2518, 2008

[40] S. Infanger, A. Haemmerli, S. Iliev, A. Baier, E. Stoyanov, and J. Quodbach, “Powder bed 3D-printing of highly loaded drug delivery devices with hydroxypropyl cellulose as solid binder,” *Int. J. Pharm.*, vol. 555, pp. 198–206, Jan. 2019.

[41] X. Xu *et al.*, “Stereolithography (SLA) 3D Printing of a Bladder Device for Intravesical Drug Delivery,” *Mater. Sci. Eng. C*, vol. 120, p. 111773, Jan. 2020.

[42] F. Melchels, J. Feijen, and D. Grijpma, “A review on stereolithography and its applications in biomedical engineering,” Biomaterials, vol. 31, no. 24, pp. 6121-6130, 2010.

[43] V. S. D. Voet *et al.*, “Biobased Acrylate Photocurable Resin Formulation for Stereolithography 3D Printing,” *ACS Omega*, vol. 3, no. 2, pp. 1403–1408, Feb. 2018.

[44] J. P. Kruth, P. Mercelis, J. Van Vaerenbergh, L. Froyen, and M. Rombouts, “Binding mechanisms in selective laser sintering and selective laser melting,” *Rapid Prototyping Journal*, vol. 11, no. 1. Emerald Group Publishing Limited, pp. 26–36, 2005.

[45] J. Parthasarathy, B. Starly, S. Raman, and A. Christensen, “Mechanical evaluation of porous titanium (Ti6Al4V) structures with electron beam melting (EBM),” *J. Mech. Behav. Biomed. Mater.*, vol. 3, pp. 249–259, 2009.

[46] H. Wang, B. Zhao, C. Liu, C. Wang, X. Tan, and M. Hu, “A Comparison of Biocompatibility of a Titanium Alloy Fabricated by Electron Beam Melting and Selective Laser Melting,” *PLoS One*, vol. 11, no. 7, p. e0158513, Jul. 2016.

[47] H. Antheunis, J.-C. van der Meer, M. de Geus, A. Heise, and C. E. Koning, “Autocatalytic Equation Describing the Change in Molecular Weight during Hydrolytic Degradation of Aliphatic Polyesters,” *Biomacromolecules*, vol. 11, no. 4, pp. 1118–1124, Apr. 2010.

[48] Y. Liu, Y. Zheng, and B. Hayes, “Degradable, absorbable or resorbable—what is the best grammatical modifier for an implant that is eventually absorbed by the body?,” *Science China Materials*, vol. 60, no. 5. Science China Press, pp. 377–391, 01-May-2017.

[49] J. Li, S. N. Rothstein, S. R. Little, H. M. Edenborn, and T. Y. Meyer, “The Effect of Monomer Order on the Hydrolysis of Biodegradable Poly(lactic- co -glycolic acid) Repeating Sequence Copolymers,” *J. Am. Chem. Soc.*, vol. 134, no. 39, pp. 16352–16359, Oct. 2012.

[50] S. Rey-Vinolas, E. Engel, and M. Mateos-Timoneda, “Polymers for bone repair,” in *Bone Repair Biomaterials*, Elsevier, 2019, pp. 179–197.

[51] N. Zhao, Z. Ma, and C. Xiong, “Effect of Poly(L-lactic acid) on Hydrolytic Degradation of Poly(glycolic acid),” *Int. J. Polym. Mater.*, vol. 61, no. 8, pp. 587–595, Jul. 2012.

[52] G. Nitya, G. T. Nair, U. Mony, K. P. Chennazhi, and S. V. Nair, “In vitro evaluation of electrospun PCL/nanoclay composite scaffold for bone tissue engineering,” *J. Mater. Sci. Mater. Med.*, vol. 23, no. 7, pp. 1749–1761, Jul. 2012.

[53] D. Popescu, A. Zapciu, C. Amza, F. Baciu, and R. Marinescu, “FDM process parameters influence over the mechanical properties of polymer specimens: A

review," *Polym. Test.*, vol. 69, pp. 157–166, Aug. 2018.

[54] C. C. Chen, J. Y. Chueh, H. Tseng, H. M. Huang, and S. Y. Lee, "Preparation and characterization of biodegradable PLA polymeric blends," *Biomaterials*, vol. 24, no. 7, pp. 1167–1173, 2003.

[55] P. B. Maurus and C. C. Kaeding, "Bioabsorbable implant material review," *Oper. Tech. Sports Med.*, vol. 12, no. 3, pp. 158–160, Jul. 2004.

[56] M. Fernandez-Vicente, W. Calle, S. Ferrandiz, and A. Conejero, "Effect of Infill Parameters on Tensile Mechanical Behavior in Desktop 3D Printing," *3D Print. Addit. Manuf.*, vol. 3, no. 3, pp. 183–192, Sep. 2016.

[57] L. Baich, G. P. Manogharan, H. Marie, and G. Manogharan, "Article in International Journal of Rapid Manufacturing · December," *Int. J. Rapid Manuf.*, vol. 5, p. 2015, 2015.

[58] C. L. Simões, J. C. Viana, and A. M. Cunha, "Mechanical properties of poly(ε-caprolactone) and poly(lactic acid) blends," *J. Appl. Polym. Sci.*, vol. 112, no. 1, pp. 345–352, Apr. 2009.

[59] I. Navarro-Baena, V. Sessini, F. Dominici, L. Torre, J. M. Kenny, and L. Peponi, "Design of biodegradable blends based on PLA and PCL: From morphological, thermal and mechanical studies to shape memory behavior," *Polym. Degrad. Stab.*, vol. 132, pp. 97–108, Oct. 2016.

[60] A. K. Matta, R. U. Rao, K. N. S. Suman, and V. Rambabu, "Preparation and Characterization of Biodegradable PLA/PCL Polymeric Blends," *Procedia Mater. Sci.*, vol. 6, pp. 1266–1270, Jan. 2014.

[61] D. Rawtani, and Y. K. Agrawal, "Multifarious applications of halloysite nanotubes: a review." *Rev. Adv. Mater. Sci*, vol. 30, no. 3, pp. 282-295, 2012.

[62] M. Liu, Z. Jia, D. Jia, and C. Zhou, "Recent advance in research on halloysite nanotubes-polymer nanocomposite," *Prog. Polym. Sci.*, vol. 39, pp. 1498–1525, 2014.

[63] M. Leyva-Leyva *et al.*, "Differential Expression of Adhesion-Related Proteins and MAPK Pathways Lead to Suitable Osteoblast Differentiation of Human Mesenchymal Stem Cells Subpopulations," *Stem Cells Dev.*, vol. 24, no. 21, pp. 2577–2590, Nov. 2015.

[64] L. Meinel *et al.*, "Bone Tissue Engineering Using Human Mesenchymal Stem Cells: Effects of Scaffold Material and Medium Flow," *Annals of Biomedical engineering*, vol. 32. no. 1, 2004.

[65] W. Fan *et al.*, “CD105 promotes chondrogenesis of synovium-derived mesenchymal stem cells through Smad2 signaling,” *Biochem. Biophys. Res. Commun.*, vol. 474, no. 2, pp. 338–344, May 2016.

[66] S. Zhou, “TGF-β regulates β-catenin signaling and osteoblast differentiation in human mesenchymal stem cells,” *J. Cell. Biochem.*, vol. 112, no. 6, pp. 1651–1660, Jun. 2011.

[67] P. Bahl, C. Doolan, C. De Silva, A. A. Chughtai, L. Bourouiba, and C. R. Macintyre, “Airborne or droplet precautions for health workers treating COVID-19?." *The Journal of infectious diseases*," vol. 20, pp. 1-8, 2020

[68] K. G. Andersen, A. Rambaut, W. I. Lipkin, E. C. Holmes, and R. F. Garry, “The proximal origin of SARS-CoV-2,” *Nature Medicine*, vol. 26, no. 4. Nature Research, pp. 450–452, 01-Apr-2020.

[69] A. B. Patel and A. Verma, “Nasal ACE2 Levels and COVID-19 in Children,” *JAMA - Journal of the American Medical Association*, vol. 323, no. 23. American Medical Association, pp. 2386–2387, 16-Jun-2020.

[70] M. Hoffmann *et al.*, “SARS-CoV-2 Cell Entry Depends on ACE2 and TMPRSS2 and Is Blocked by a Clinically Proven Protease Inhibitor,” *Cell*, vol. 181, no. 2, pp. 271-280.e8, Apr. 2020.

[71] R. Yan, Y. Zhang, Y. Li, L. Xia, Y. Guo, and Q. Zhou, “Structural basis for the recognition of SARS-CoV-2 by full-length human ACE2,” *Science (80-. ).*, vol. 367, no. 6485, pp. 1444–1448, Mar. 2020.

[72] F. Li, “Structure, Function, and Evolution of Coronavirus Spike Proteins,” *Annu. Rev. Virol.*, vol. 3, no. 1, pp. 237–261, Sep. 2016.

[73] D. Wrapp *et al.*, “Cryo-EM structure of the 2019-nCoV spike in the prefusion conformation,” *Science (80-. ).*, vol. 367, no. 6483, pp. 1260–1263, Mar. 2020.

[74] Z. Sun and K. (Ken) Ostrikov, “Future antiviral surfaces: Lessons from COVID-19 pandemic,” *Sustainable Materials and Technologies*, vol. 25. Elsevier B.V., p. e00203, 01-Sep-2020.

[75] World Health Organization, “COVID19 pandemic,” 2020. [Online]. Available: https://www.who.int/publications/i/item/draft-operational-planning-guidance-for-un-country-teams [accessed Sep. 2020]

[76] World Health Organization, “Coronavirus disease (COVID-19) pandemic.,” 2020. [Online]. Available: https://www.who.int/emergencies/diseases/novel-coronavirus-2019 . [accessed Aug. 2020]

[77] L. Science, “How are people being infected with COVID 19.” [Online]. Available: https://www.livescience.com/how-covid-19-spreads-transmission-routes.html. [accessed Aug. 2020]

[78] World Health Organization, . “Infection prevention and control during health care when COVID-19 is suspected.” [Online]. Available: https://www.who.int/publications-detail/infection-prevention-and-control-during-health-care-when-novel-coronavirus-(ncov)-infection-is-suspected-20200125. [accessed Oct. 2020]

[79] P. C. Y. Woo *et al.*, “Characterization and Complete Genome Sequence of a Novel Coronavirus, Coronavirus HKU1, from Patients with Pneumonia Downloaded from,” *J. Virol.*, vol. 79, no. 2, pp. 884–895, 2005.

[80] V. Monteil *et al.*, “Inhibition of SARS-CoV-2 Infections in Engineered Human Tissues Using Clinical-Grade Soluble Human ACE2,” *Cell*, vol. 181, no. 4, pp. 905-913.e7, May 2020.

[81] C. for D. Control, “2019 COVID-19 fact sheet,” 2020. [Online]. Available: https://www.cdc.gov/coronavirus/2019-ncov/downloads/2019-ncov-factsheet.pdf. [accessed Sep. 2020]

[82] USFDA, “No Title,” 2020. [Online]. Available: https://www.fda.gov/medical-devices/personal-protective-equipment-infection-control/faqs-shortages-surgical-masks-and-gowns –2020. [accessed Aug. 2020]

[83] Z. Lei and J. Yang, “Computer-aided customized shape design of an N95 filtering facepiece respirator,” in *Proceedings of the ASME Design Engineering Technical Conference*, pp. 1-9, 2013.

[84] 3M, “Surgical N95 vs. Standard N95 – Which to Consider?,” 2020. [Online]. Available: https://multimedia.3m.com/mws/media/1794572O/surgical-n95-vs-standard-n95-which-to-consider.pdf [accessed Aug. 2020]

[85] H. Singh Nalwa and R. Singh, “Medical Applications of Nanoparticles in Biological Imaging, Cell Labeling, Antimicrobial Agents, and Anticancer Nanodrugs,” *Artic. J. Biomed. Nanotechnol.*, vol. 7, pp. 489–503, 2011.

[86] U. Y. Qazi and R. Javaid, “A Review on Metal Nanostructures: Preparation Methods and Their Potential Applications,” *Adv. Nanoparticles*, vol. 05, no. 01, pp. 27–43, Feb. 2016.

[87] D. Kim, J. Quinn, B. Pinsky, N. H. Shah, and I. Brown, “Rates of Co-infection between SARS-CoV-2 and Other Respiratory Pathogens,” *JAMA - Journal of the American Medical Association*, vol. 323, no. 20. American Medical Association, pp. 2085–2086, 26-May-2020.

[88] J. M. Zuniga and A. Cortes, “The role of additive manufacturing and antimicrobial polymers in the COVID-19 pandemic,” *Expert Rev. Med. Devices*, vol. 17, no. 6, pp. 477–481, Jun. 2020.

[89] H. H. Tuson and D. B. Weibel, “Bacteria-surface interactions,” *Soft Matter*, vol. 9, no. 17. Royal Society of Chemistry, pp. 4368–4380, 05-May-2013.

[90] T. F. C. Mah and G. A. O’Toole, “Mechanisms of biofilm resistance to antimicrobial agents,” *Trends in Microbiology*, vol. 9, no. 1. Elsevier, pp. 34–39, 01-Jan-2001.

[91] R. Turner, “Is Silver the Ultimate Antimicrobial Bullet?,” *Antibiotics*, vol. 7, no. 4, p. 112, Dec. 2018.

[92] Y. N. Slavin, J. Asnis, U. O. Häfeli, and H. Bach, “Metal nanoparticles: Understanding the mechanisms behind antibacterial activity,” *Journal of Nanobiotechnology*, vol. 15, no. 1. BioMed Central Ltd., p. 65, 03-Oct-2017.

[93] F. Paladini, M. Pollini, A. Sannino, and L. Ambrosio, “Metal-Based Antibacterial Substrates for Biomedical Applications,” *Biomacromolecules*, vol. 16, no. 7, pp. 1873-1885, 2015.

[94] S. Katva, S. Das, H. S. Moti, A. Jyoti, and S. Kaushik, “Antibacterial synergy of silver nanoparticles with gentamicin and chloramphenicol against Enterococcus faecalis,” *Pharmacogn. Mag.*, vol. 13, no. 52, pp. S828–S833, Oct. 2017.

[95] A. Mikolay, S. Huggett, L. Tikana, G. Grass, J. Braun, and D. H. Nies, “Survival of bacteria on metallic copper surfaces in a hospital trial,” *Appl. Microb. CELL Physiol.*

[96] S. M. Dizaj, F. Lotfipour, M. Barzegar-Jalali, M. H. Zarrintan, and K. Adibkia, “Antimicrobial activity of the metals and metal oxide nanoparticles,” *Materials Science and Engineering C*, vol. 44. Elsevier Ltd, pp. 278–284, 01-Nov-2014.

[97] J. H. Hwang, H. Choi, I.-S. Hwang, K.-J. Kim, and D. G. Lee, “Synergistic effect with silver nanoparticles and its involved mechanisms. Synergistic effects between silver nanoparticles and antibiotics and the mechanisms involved,” *J. Med. Microbiol.*, vol. 61, no. 12, pp. 1719-1726, 2012.